THESE

présentée à

L'UNIVERSITE BORDEAUX 1

ECOLE DOCTORALE DES SCIENCES PHYSIQUES ET DE L'INGENIEUR

par **Stanislav GOLKIN**

POUR OBTENIR LE GRADE DE

DOCTEUR

SPÉCIALITÉ : MÉCANIQUE ET INGÉNIERIE

SIMULATION DE LA PROPAGATION D'ONDES SH DANS DES STRUCTURES PÉRIODIQUES ET DE LA DIFFUSION MULTIPLE D'ONDES DE VOLUME EN MILIEUX ALÉATOIRES

SIMULATION OF SHEAR SURFACE WAVE PROPAGATION IN PERIODIC STRUCTURES AND OF BULK WAVE SCATTERING IN RANDOM MEDIA

Soutenue le 21 décembre 2012

Après avis de :
M. E. LE CLEZIO, Professeur, Université de Montpellier **Rapporteurs**
M. A. STOVAS, Professeur, Norwegian University of Science and Technology, Trondheim, Norway

Devant la commission d'examen formée de :
M. E. LE CLEZIO, Professeur, Université de Montpellier **Rapporteurs**
M. A. STOVAS, Professeur, Norwegian University of Science and Technology, Trondheim, Norway
M. M. CASTAINGS, Professeur, Université de Bordeaux **Examinateurs**
M. A. PICHUGIN, Lecturer, Brunel University, UK
M. A. SHUVALOV, Directeur de Recherche CNRS, Université de Bordeaux
M. O. PONCELET, Chargé de Recherche CNRS, Université de Bordeaux

- 2012 -

Acknowledgments

The completion of my dissertation and subsequent Ph.D. has been a long journey. Everyone has one work or task in his life that makes him face himself and reconsider his regard toward himself and his objectives. This PhD thesis was such a challenge for me. A human being grows into the personality only by overcoming difficulties and by keeping the self-confidence in the difficult situations. Now, when I look at the path I made, I feel proud of the work I performed.

I would like to express my heartfelt gratitude to people who helped me on this path. Without these supporters, especially the selected few I'm about to mention, I may not have gotten to where I am today, at least not sanely.

First of all, I want to give the special thanks to both of my advisors Directeur de Recherche CNRS Alexander Shuvalov and Chargé de Recherche CNRS Olivier Poncelet. Their patience, flexibility and thoughtful guidance made this dissertation possible. They played very important role during my 3 years past in Laboratoire Mechanique Physique (now, Institut de Mécanique et d'Ingénierie de Bordeaux) as my scientific advisors as well as my friends and mentors in everyday life. Olivier and Sasha crossed with me black and white periods I had during these years and supported me despite all odds. Olivier's franchise and scientific agility multiplied by Alexander's impressive scientific base and wisdom gave all its colors to my thesis and helped me to open new scientific and engineering horizons.

My studies were performed at the Laboratoire de Mécanique Physique (now, Institut de Mécanique et d'Ingénierie de Bordeaux, UMR CNRS 52 95) University Bordeaux 1. I wish to express my gratitude to Directeur de Recherche Marc Deschamps for having me in his laboratory.

Here, I would like to express my gratitude to the members of the jury:

- M. A. STOVAS, Professeur, Norwegian University of Science and Technology, Trondheim, Norway
- M. E. LE CLÉZIO, Professeur, Université de Montpellier, France
- M. A. PICHUGIN, Lecturer, Brunel University, UK

and the president of the jury:

- M. CASTAINGS, Professeur, Université Bordeaux 1, France

I would like to thank Professeur of University Bordeaux 1 Christophe Aristegui and his PhD student Mihai Caleap (now Research Assistant in University of Bristol, UK) for providing the analytical results for MST (Multiple Scattering Theory) confirming the consistency and accuracy of the numerical scheme developed in this thesis. Mihai was also my neighbour in the office and it is a pleasure to collaborate with him and to have a friend like him.

I'm grateful to Alexander Zarkh who participated in development of the numerical scheme for P-SV waves during his internship in LMP Bordeaux.

I thank Bertrand Audoin for his wise advice when it was mostly needed.

I don't forget to thank Nikolay Chigarev. Thank you for being my friend and bringing a good mood and a lot of smiles with you all the time.

I thank my close friends I met during my stay in Bordeaux: Nikita and Kira, Julia, Alina, Christina, Ita, Olya and Fabrice, Natasha, Lena and Cyril, Katya and Jordi.

I also thank all my fellows PhD students in LMP: Mahmoud, Mhamad, Slah, Ludovic, Thomas, Weina and others. Thank you Sandrine, Béatrice for helping us with administration and paper work.

Mama, Papa, without you, your support and the knowledge how you were worried about me and how close to the heart you take my achievement and problems, I would have never made it!

Julietta, you won't have reasons to be jealous to my PC anymore! Working till late in the night, it's finished! Kiss you, my dear!

At the end I want to say to my both grandmothers who were both dreaming to see me PhD: I made it, it is for you too!(Бабушки, я сделал это! Это для вас тоже! Я помню о вас!)

To my grannies.

(Посвящаю моим бабушкам)

Résumé français

La propagation des ondes élastiques dans les milieux hétérogènes, aléatoires ou périodiquement structurés, est un sujet d'intérêt dans de nombreux domaines tels que l'acoustique physique, l'évaluation non destructive, le génie civile, la géophysique et bien d'autres encore. L'étendue des applications potentielles va du diagnostic de matériaux endommagés aux nouveaux phénomènes acoustiques dans les milieux artificiels que sont les cristaux phononiques et les métamatériaux. L'utilisation de simulations numériques est très utile pour la description de la propagation des ondes dans de telles structures complexes où le traitement analytique est surchargé de nombreuses difficultés théoriques.

Dans cette thèse nous développons un code de différences finies dans le domaine temporel (FDTD) et nous l'appliquons à deux types différents de problèmes de la propagation des ondes élastiques en milieux hétérogènes. Le premier concerne le problème des ondes de cisaillement horizontales (ondes SH) dans des structures verticalement périodiques. Nous comparons des résultats numériques avec les caractéristiques de dispersion d'ondes de surface SH directement calculées dans le domaine spectral (ω, k) pour ces structures. Nous utilisons aussi les simulations numériques dans le but d'extraire plusieurs types d'évaluations de propriétés de champs qui ne peuvent pas être obtenues analytiquement. Le second problème, sur lequel nous appliquons notre code numérique, est la diffusion multiple d'ondes SH et d'ondes P/SV (ondes de pression et cisaillement polarisées dans le plan de propagation). En particulier le code FDTD nous permet de recouvrer la statistique (caractéristiques moyennes) [1] de la propagation d'ondes dans des milieux aléatoires (à partir de l'estimation des propriétés en réflexion et transmission d'une couche aléatoire), qui est comparée à des estimations analytiques de la théorie de la diffusion multiple (MST) [2]. Cette dernière application est supposée servir une validation supplémentaire de la méthode numérique développée et doit mettre en avant ses perspectives pratiques étendues.

L'étude des ondes de surface acoustiques dans des structures verticalement périodiques est motivée par certaines particularités étonnantes de leur spectre de dispersion qui apparaissent spécifiquement à cause de la périodicité des propriétés du matériau dans sa profondeur. Comme conséquence, les courbes de dispersion des ondes de surface peuvent s'étendre jusqu'à des lenteurs horizontales nulles et il arrive qu'elles se présentent sous la

forme d'intervalles aléatoirement discontinus. Étant donné un demi-espace verticalement périodique avec un plan de symétrie vertical, les ondes de surface SH (SHSW) possèdent des spécifications additionnelles. C'est que les courbes de dispersion des solutions « physiques » et « non physiques » des ondes SHSW (ce caractère étant attribué selon leur croissance ou décroissance dans la profondeur), sont alternativement des intervalles des courbes de dispersion d'un autre spectre de dispersion, à savoir, le spectre des ondes guidées dans une seule cellule élémentaire (une seule période) considérée comme libre sur ses deux bords. Cette particularité a d'abord été notée pour des empilements périodiques de couches homogènes [3, 4] et ensuite démontrée pour des milieux périodiques gradués par morceaux [5]. La problème de l'obtention de la dispersion des SHSW se réduit alors au calcul des courbes de dispersion d'une seule cellule élémentaire, libre, du milieu périodique, et à l'identification des zones spectrales où l'onde de surface est « physique », et donc existe. D'une façon générale, on peut simplement dire que les SHSW sont attendues sur des segments aléatoires le long des courbes de référence d'une cellule élémentaire, qui peuvent être identifiés en testant seulement numériquement la condition de radiation. Cependant, et ceci constitue l'une de nos principales motivations dans ce travail, l'existence des SHSW peut souvent être « décidée » ou prédite sans aucun calcul préalable, simplement en examinant certaines propriétés de base du profil de la cellule élémentaire qu'il soit continue ou constant par morceaux (dépendance des propriétés matérielles sur une période). Comme nous le voyons, un lien direct existe indubitablement entre la forme du profil et l'existence des SHSW dans un demi-espace périodique continu par morceaux dont les propriétés matérielles sont différentes aux bords opposés de la période. Dans un tel cas, le spectre de dispersion des SHSW peut être remarquablement régulier en cela qu'il est confiné dans un certain intervalle de lenteur (intervalle qui admet une évaluation analytique simple). Par exemple, le profil d'une cellule élémentaire peut être arrangé de telle sorte que les SHSW existent au sein d'une unique « fenêtre » de lenteur (unique couloir spectral dans le plan (ω, k)), qui est étroit proportionnellement au contraste entre les paramètres matériels aux bords de la cellule élémentaire. Alternativement, le profil peut être construit de manière à ce que les SHSW soient exclues d'une lacune unique de lenteur. Une telle maîtrise autorise un design judicieux du profil de la cellule élémentaire pour réaliser des propriétés spectrales voulues pour les SHSW qui deviennent dès lors intéressantes pour certaines applications.

La diffusion multiple des ondes est un sujet concernant de nombreux domaines de la physique et spécialement ceux traitant des milieux aléatoires [6]. La MST est une technique analytique dont l'objectif est de déterminer le nombre d'onde effectif à valeur complexe des ondes cohérentes se propageant dans des milieux aléatoires. Elle s'appuie sur les propriétés de diffusion (les coefficients de la matrice T de diffusion) d'un seul diffuseur [7], mais aussi potentiellement (pour des méthodes plus élaborées) sur la fonction de corrélation de paire qui prend en compte la corrélation spatiale entre les diffuseurs [8] et des ordres supérieurs d'interactions dans le processus de diffusion entre objets. Il s'agit dans l'ensemble d'une technique analytique plutôt sophistiquée qui utilise un certain nombre d'hypothèses et qui implique des développements mathématiques laborieux. En même temps, cet effort aboutit à des formules analytiques explicites pour des caractéristiques importantes des ondes que sont le nombre d'onde, l'atténuation, ainsi que que les paramètres mécaniques effectifs [9]. En général, les limitations pratiques des techniques MST ne sont pas clairement spécifiées puisqu'il est très difficile de définir leur critère de précision. Par exemple, la gamme de concentrations d'inclusions et leur taille relative (par rapport à la longueur d'onde) qui autorisent une précision raisonnable ne peuvent pas être estimées en tant que telles, mais simplement être comparées entre différentes techniques MST.

Parce que la MST est une technique traitant de la diffusion stochastique, il est pratiquement compliqué de comparer ses résultats avec des calculs déterministes, sauf si l'aspect aléatoire de ces derniers est reconstruit. Expérimentalement, ceci est atteint en faisant plusieurs mesures à des positions différentes des capteurs dans le but de moyenner les signaux acoustiques sur le désordre du milieu. Ainsi plusieurs réalisations du désordre sont virtuellement effecuées. Une autre façon de procéder est d'effectuer des expériences numériques déterministes qui nous permettent de faire plusieurs fois la même simulation de propagation d'ondes mais avec des réalisations différentes du désordre. Donc, après moyenne des signaux résultants de l'ensemble des simulations, nous pouvons recouvrer l'onde « moyenne » (ou onde cohérente) sur la statistique du milieu aléatoire. Cette approche possède l'avantage d'être relativement facile d'implémentation tant que le code numérique est capable de tayloriser la même simulation avec plusieurs échantillons de la distribution statistique à l'étude. Dans ce travail nous présentons de telles comparaisons entre des résultats issus de la MST et d'autres obtenus par simulations numériques pour les cas de la diffusion

acoustique par une population de fissures plates et par une distribution d'inclusions cylindriques.

Ces dernières décennies, le progrès dans la simulation des phénomènes linéaires de propagation, incluant l'acoustique, l'électromagnétisme, et les ondes élastiques, a rapidement crû à cause de l'amélioration marquée des technologies informatiques. Les schémas standard de différences finies (incluant le célèbre schéma de Yee [10] sur une grille spatio-temporelle décalée pour des applications électromagnétiques) sont devenus des algorithmes numériques communément utilisés à cause de leur simplicité d'implémentation et leur flexibilité. Il est aussi bien connu que la propagation des ondes sur de longues distances nécessite une intégration sur des temps longs avec une dissipation et une dispersion numériques minimales. Toutefois leur possible haut coût CPU et de stockage mémoire amène parfois à des efficacités réduites des algorithmes, qui peut limiter du coup leur utilisation pratique.

Dans cette thèse nous implémentons un schéma de différences finies d'ordre deux pour la propagation des ondes élastiques sur une grille cartésienne 2D décalée avec celle du temps [11]. Nous appliquons le code FDTD développé au problème de la propagation des ondes élastiques de surface le long de structures périodiques et au problème de la diffusion multiple dans des milieux aléatoires. Nous vérifions que les résultats numériques issus du schéma développé produisent des accords convaincants avec ceux prédits théoriquement. Dans ce projet nous faisons le design du code en langage orienté-objet C++, et nous l'implémentons pour le cas des ondes SH et des ondes P/SV, offrant ainsi une possibilité de traiter numériquement différents types de problèmes d'acoustique. Un avantage essentiel de l'approche utilisée dans la confection informatique de ce code est que les conditions aux limites et les propriétés des matériaux peuvent être définies simplement dans une interface graphique facile d'utilisation. Ceci implique que l'utilisateur final peut créer une nouvelle configuration physique sans avoir besoin d'écrire aucune ligne de codes. En d'autres termes, le présent code peut être employé par n'importe quel utilisateur qui n'est pas familier de la programmation et de la méthode FDTD.

La thèse est organisée de la manière suivante. Le chapitre 1 introduit les définitions élémentaires et les équations de l'élastodynamique. Le système d'équations différentielles du second ordre gouvernant la propagation des ondes est reformulé sous l'aspect du formalisme

de Stroh (formalisme du vecteur d'état), c'est-à-dire comme le système différentiel ordinaire à coefficients constants ou variables qui admet le matricant (matrice propagateur) comme solution. Cette approche est utilisée au chapitre 2 pour considérer la propagation des ondes SH dans des structures dont les propriétés matérielles varient périodiquement (continûment ou discrètement) le long d'une direction qui est orthogonale aux interfaces. L'attention principale est apportée au cas des ondes de surface SH (SHSW). Il est montré qu'il existe un lien direct entre l'allure du profil périodique et l'existence des SHSW. Ce lien est particulièrement impactant lorsque les propriétés matérielles sont monotones sur une période. Pour ce cas particulier de profils, la zone d'existence des SHSW sur les courbes de dispersion est réduite à une bande étroite de vitesse, qui admet en réalité une évaluation explicite. Le chapitre 3 décrit la méthode FDTD qui est utilisée dans la thèse pour simuler numériquement la propagation d'ondes élastiques. Ce chapitre présente les schémas pour les ondes SH et P/SV, ainsi que le traitement des conditions aux limites au sein des schémas. Il présente aussi l'implémentation des Perfectly Matched Layers dans les schémas. Le chapitre 4 présente des informations sur les procédures de post-traitement qui permettent d'extraire d'une simulation les grandeurs désirées. Le chapitre 5 compare les résultats de la FDTD à ceux obtenus analytiquement pour les ondes SH de surface dans des milieux verticalement périodiques. Dans ce chapitre, nous fournissons aussi les détails techniques de la mise en place des simulations (paramètres d'entrée, choix des termes sources…), ainsi que des procédures spécifiques pour extraire certaines caractéristiques de champs. Finalement, le chapitre 6 met en valeur l'application de la technique numérique pour les problèmes de diffusion multiple des ondes Sh et P/SV dans les milieux aléatoires [1]. En particulier, il est montré que les simulations FDTD déterministes sont utiles pour recouvrer le spectre de réflectivité « moyen » d'une couche constituée d'une population aléatoire d'inclusions distribuées uniformément (fissures plates, cavités cylindriques et inclusions cylindriques solides), qui peuvent parallèlement être décrites par des approches stochastiques telles que la MST développée par Waterman et Truell [2] par exemple. Nous traitons aussi le cas plus général d'une distribution spatialement non uniforme de fissures plates [12].

Références

1. M. Chekroun, L.L. Marrec, B. Lombard, J. Piraux, Time-domain numerical simulations of multiple scattering to extract elastic effective wavenumbers, Waves Random Complex 22 (2012) 398-422.

2. P.C. Waterman, R. Truell, Multiple scattering of waves, J. Math. Phys. 2 (1961) 512-537.

3. A.N. Podlipenets, Surface Love Wave in Orthotropic Regularly Layered Composites, Mech. Comp. Matter. 18 (1982) 734-737.

4. A.N. Podlipenets, N.A. Shulga, Propagation of a harmonic shear wave in an orthotropic regularly layered plate., Sov. Appl. Mech 21 (1985) 1092−1096.

5. A.L. Shuvalov, O. Poncelet, A.N. Podlipenets, On the guided and surface shear horizontal waves in monoclinic transversely periodic layers and halfspace with arbitrary variation of material peroperties across the unit cell, Stud. Geophys. Geod. 50 (2006) 381-398.

6. A. Ishimaru, Wave Propagation and Scattering in Random Media, IEEE Press and Oxford University Press, Piscataway, NJ, 1997.

7. L.L. Foldy, The multiple scattering of waves. I. General theory of isotropic scattering by randomly distributed scatterers, Phys. Rev. 67 (1945) 107.

8. M. Caleap, B.W. Drinkwater, P.D. Wilcox, Coherent acoustic wave propagation in media with pair-correlated spheres, J. Acoust. Soc. Am. 131 (2012).

9. C. Aristégui, Y.C. Angel, Effective mass density and stiffness derived from P-wave multiple scattering, Wave Motion 44 (2007) 153-164.

10. K.S. Yee, Numerical solution of initial boundary value problems involving Maxwell's equations in isotropic media, IEEE Transactions on Antennas and Propagation 40 (1966) 302-307.

11. J. Virieux, P-SV wave propagation in heterogeneous media: velocity-stress finite-difference method, Geophysics 51 (1986) 889-901.

12. C. Aristégui, M. Caleap, O. Poncelet, S.V. Golkin, A.L. Shuvalov, Coherent elastic wave propagation through non-uniform spatial distributions of cracks, in: Proceedings of Acoustics'08, 29 June–4 July, Paris, France, 2008. CD ROM, ISBN 978−2−9521105−4−9, pp. 5963−5967.

General Introduction

Propagation of elastic waves in heterogeneous, randomly or periodically structured media is of interest for different domains such as physical acoustics, non-destructive evaluation, civil engineering, geophysics and others. The area of possible applications ranges from traditional problems of testing damaged materials to designing new acoustic phenomena in manmade phononic crystals and metamaterials. The use of numerical simulations is very helpful for describing wave propagation in such complex structures where analytical treatment may be overcharged with many theoretical difficulties.

In the thesis we will develop Finite-Difference Time-Domain (FDTD) method and apply it to two different types of problems of elastic wave propagation in inhomogeneous media. The first is the problem of shear horizontal (SH) waves in vertically periodic structures. We will compare numerical results with dispersion characteristics of surface SH waves directly calculated in the (ω, k) domain for such structures. We will also use the numerical simulations in order to extract several evaluations which cannot be obtained analytically. The second problem, to which we will apply the created numerical scheme, is the multiple scattering for SH and in-plane (P/SV) waves. In particular the FDTD code will enable us to recover the statistics (mean characteristics) [1] of the wave propagation in some random media (via the estimation of the reflection and transmission properties of a random slab), which will be compared to the analytical estimation of Multiple Scattering Theory (MST) [2]. This latter application is supposed to provide one more validation of the developed numerical method and should further highlight its broad practical perspectives.

The study of surface acoustic waves in vertically periodic structures is motivated by certain striking particularities of the dispersion spectrum which arise specifically due to periodicity of depth-dependent material properties. As its consequence, the surface-wave dispersion branches may extend down to zero horizontal slowness and they may come about in the form of randomly broken intervals. Given a vertically periodic halfspace with a vertical symmetry plane, further specificity pertains to the shear horizontal surface waves (SHSW). It is that the dispersion branches for ’physical’ and ’non-physical’ SHSW solutions, attributed as such due to their decrease or increase into the depth, are alternating intervals of the dispersion curves of actually another spectrum, namely, the spectrum for guided waves in a

single unit cell (period) considered as a free layer. This feature has been noted first for periodic stacks of homogeneous layers [3, 4]) and then proved for an arbitrary piecewise continuous vertically periodic inhomogeneity [5]. The problem of finding the SHSW reduces therefore to calculating the dispersion branches of a free unit cell layer and to identifying their spectral ranges where the surface wave is 'physical' and hence does exist. Generally speaking, the SHSW may be expected to exist on random intervals of the reference unit-cell branches which can be identified by testing the radiation numerically only. However, and this is one of the main motivations for our study, existence of SHSW can often be decided without any calculations, by merely inspecting certain basic benchmarks of a given continuous or piecewise constant unit-cell profile (a dependence of material properties over period). As we will see, a direct link between this profile shape and the SHSW existence is especially compelling in a piecewise continuous periodic halfspace whose material properties are different at the opposite edges of a period. In such a case, the SHSW dispersion spectrum may be remarkably regular in that it is confined within certain slowness values and these admit a simple analytical evaluation. For example, a unit-cell profile can be arranged so that the SHSW exists within a single slowness 'window' (single spectral corridor on the (ω, k)-plane), which is narrow in the measure of contrast between material values at the unit-cell edges. Alternatively, the SHSW may be precluded within a single slowness 'gap'. Such knowledge enables a judicious design of unit-cell profile for realizing desirable spectral properties of SHSW which may be interesting for applications.

Multiple scattering of waves is a topic relevant to many areas of physics and especially to those dealing with random media [6]. The MST is an analytical technique intended to provide the effective complex-valued wavenumber of the coherent waves propagating in random media. It mainly relies on the scattering properties (the T-matrix scattering coefficients) of only one scatterer [7], but possibly also (for the more elaborate methods) on the pair-correlation function that takes into account the spatial correlation between scatterers [8] and higher orders of interaction in the scattering process in between objects. It is on the whole a rather sophisticated analytical tool which uses various assumptions and involves laborious mathematical developments. At the same time, this effort yields the way to obtain analytical formulas for such important wave characteristics as effective wavenumber, attenuation and also effective mechanical properties [9]. In general the practical limitations of

the MST techniques are not clearly specified since it is difficult to define their precision criteria. For instance, the ranges of concentration of inclusions and of their size to wavelength ratio which yet allow reasonable accuracy cannot be estimated on their own and can only be compared in between different MST methods.

Because MST is a technique dealing with stochastic scattering, it is not in practice straightforward to compare its results with deterministic calculations, unless the randomness of the latter is reconstructed. Experimentally, this is achieved by doing several measurements at different positions of the sensors in order to average the signals over the disorder of the medium. Hence, several realizations of the disorder are virtually performed. Another way is to run deterministic numerical experiments which enables us to redo several times the same simulation but with several realizations of the disorder. Therefore, after averaging the resulting signals, we can recover the mean wave (or coherent wave) over the statistics of the random medium. This approach has the advantage of being relatively easy to perform as long as the numerical code is able to taylor the same simulations over several samples of the statistical distribution under study. In this work we present such comparisons between MST results and numerical simulations for the cases of scattering by a population of flat cracks and by a distribution of cylindrical inclusions.

In the past decades, progress in simulating linear wave phenomena, including acoustic, electromagnetic, and elastic waves, has been rapidly growing due to the improving performance of digital computers. The standard second order finite difference schemes (including the famous Yee's FDTD method [10] on staggered grid in computational electromagnetic applications) are commonly used numerical algorithms because of their simplicity and flexibility. It is also well known that the propagation of waves over long distances requires long-time integration with minimal numerical dissipation and dispersion. However, their extraordinarily computational costs lead to relatively low algorithm efficiency, which limits their utilization in practice.

In this thesis we will implement second order finite difference scheme for elastic wave propagation on Cartesian 2D-grids with completely staggered stencils [11]. We will apply the developed FDTD method to the problem of surface elastic waves propagating in periodical structures and to the problem of multiple scattering in random media. We will verify that the numerical results of developed scheme give a convincing agreement with the theoretically

predicted ones. In this project, we will design the general object-oriented code in C++ and implement it for SH and P/SV acoustic waves, enabling a possibility to treat various acoustics problems numerically. Essential advantage of the approach used in the code is that all the boundary conditions and material properties may be defined in a friendly user interface. It means that the end user is able to create a new physical configuration without writing any code. In other words, the present code can be utilized by any user who does not have to be familiar with C++ programming and FDTD method.

The thesis is organized as follows. Chapter 1 introduces basic definitions and equations of the elastodynamics theory. The governing system of second order differential equations is cast in the form of the Stroh matrix formalism, i.e. as the first-order ordinary differential system with constant or varying coefficients which admits the matricant solution. This approach is used in Chapter 2 in order to consider SH wave propagation in the structures, whose material properties vary periodically (continuously or discretely) along one direction which is orthogonal to the boundary. The main attention is given to the SH surface waves (SHSW). It is found that there exists a direct link between the periodic profile shape and the existence of SHSW. This link is especially compelling when the material properties are monotonic over a period. For the particular cases of profile shapes, the range of existence of SHSW on the dispersion curves is 'squeezed' to a narrow velocity window, which actually admits a simple and explicit evaluation. Chapter 3 describes FDTD method that is used in the thesis to numerically simulate elastic wave propagation. This chapter presents the schemes for SH waves and P/SV waves as well as the treatment of boundary conditions in these schemes. Also, it demonstrates the Perfectly Matched Layers implementation in the current schemes. In Chapter 4, efficient managing of different numerical parameters in order to optimize simulation is considered. This chapter also provides information about used post-treatment procedures which allows us to extract desired characteristics from the simulation by means of different Fast Fourier Transform algorithms. Chapter 5 compares the FDTD and the analytical results for the SH surface waves in vertically periodic media. In this chapter we also give technical details on the implementation of simulation and the procedure of extracting results. Finally, Chapter 6 demonstrates application of the FDTD method to the problems of multiple scattering of SH and P/SV waves in random media [1]. In particular, it is shown that the deterministic FDTD simulations are useful to recover the ‘mean’ reflectivity spectra of a slab

consisting of a random population of uniformly distributed inclusions (flat cracks, cylindrical cavities and cylindrical solid inclusions), which are analytically described by stochastic approaches such as the MST developed by Waterman and Truell [2] for instance. We also tackle a more general case of a non-uniform spatial distribution [12].

References

1. M. Chekroun, L.L. Marrec, B. Lombard, J. Piraux, Time-domain numerical simulations of multiple scattering to extract elastic effective wavenumbers, Waves Random Complex 22 (2012) 398-422.

2. P.C. Waterman, R. Truell, Multiple scattering of waves, J. Math. Phys. 2 (1961) 512-537.

3. A.N. Podlipenets, Surface Love Wave in Orthotropic Regularly Layered Composites, Mech. Comp. Matter. 18 (1982) 734-737.

4. A.N. Podlipenets, N.A. Shulga, Propagation of a harmonic shear wave in an orthotropic regularly layered plate., Sov. Appl. Mech 21 (1985) 1092−1096.

5. A.L. Shuvalov, O. Poncelet, A.N. Podlipenets, On the guided and surface shear horizontal waves in monoclinic transversely periodic layers and halfspace with arbitrary variation of material peroperties across the unit cell, Stud. Geophys. Geod. 50 (2006) 381-398.

6. A. Ishimaru, Wave Propagation and Scattering in Random Media, IEEE Press and Oxford University Press, Piscataway, NJ, 1997.

7. L.L. Foldy, The multiple scattering of waves. I. General theory of isotropic scattering by randomly distributed scatterers, Phys. Rev. 67 (1945) 107.

8. M. Caleap, B.W. Drinkwater, P.D. Wilcox, Coherent acoustic wave propagation in media with pair-correlated spheres, J. Acoust. Soc. Am. 131 (2012).

9. C. Aristégui, Y.C. Angel, Effective mass density and stiffness derived from P-wave multiple scattering, Wave Motion 44 (2007) 153-164.

10. K.S. Yee, Numerical solution of initial boundary value problems involving Maxwell's equations in isotropic media, IEEE Transactions on Antennas and Propagation 40 (1966) 302-307.

11. J. Virieux, P-SV wave propagation in heterogeneous media: velocity-stress finite-difference method, Geophysics 51 (1986) 889-901.

12. C. Aristégui, M. Caleap, O. Poncelet, S.V. Golkin, A.L. Shuvalov, Coherent elastic wave propagation through non-uniform spatial distributions of cracks, in: Proceedings of

Acoustics'08, 29 June–4 July, Paris, France, 2008. CD ROM, ISBN 978−2−9521105−4−9, pp. 5963−5967.

1 Wave propagation in elastic media

Table of contents

1.1 Introduction

When the particles of a medium are displaced from their equilibrium positions, internal restoring forces arise. This leads to oscillatory (or wave) motion inside the medium. There exist different approaches describing elastic wave propagation in solids. Direct formulation provides a system of second-order differential equations. In the case of constant coefficients, this system allows applying Fourier transform, which yields an algebraic equation called the Christoffel equation. The Christoffel equation describes a solution for free elastic waves in a homogeneous medium and is not appropriate for the case of media with one-dimensional (1D) inhomogeneity considered in the thesis. Our analysis of this case will be based on another approach, called the state-vector formalism, which casts the wave equation in the form of a first-order ordinary differential system (ODS). Such a formulation is well-suited for the task in hand.

In the present chapter, we first briefly describe the derivation of basic equations of linear anisotropic elastodynamics leading to the system of second-order differential wave equations[1]. It is then shown that this system can be transformed either to the algebraic Christoffel eigenvalue problem or to the first-order ODS, the latter admitting non-constant coefficients[2, 3]. We also explain the uncoupling of SH and P/SV waves in the presence of a symmetry plane.

1.2 Deformation and stress tensors

Let us introduce displacement as a vector function of time and space $\mathbf{u} = \mathbf{u}(\mathbf{x}, t)$, where vector $\mathbf{x}$ defines the initial position of a particle of the medium at the time t_0. After a perturbation, new position vector of this particle is $\mathbf{x}' = \mathbf{x} + \mathbf{u}$. Thus $\mathbf{u} = \mathbf{u}(\mathbf{x}, t)$ describes the displacement field caused by applied perturbation. The entire displacement field of the medium may be defined as the displacement of every point of the medium. Now consider a neighbouring point infinitesimally close to the given one. Its position vector $\mathbf{x} + \mathrm{d}\mathbf{x}$ gives the following displacement

$$\mathbf{u}(\mathbf{x} + \mathrm{d}\mathbf{x}) = \mathbf{u}(\mathbf{x}) + (\mathrm{d}\mathbf{x} \cdot \nabla)\mathbf{u} = \mathbf{u}(\mathbf{x}) + \mathrm{d}\mathbf{u}, \tag{1.1}$$

where

$$\mathrm{d}\mathbf{u} = (\mathrm{d}\mathbf{x} \cdot \nabla)\mathbf{u}. \tag{1.2}$$

Expression (1.2) can be written in index notations as

$$\mathrm{d}u_j = \frac{\partial u_j}{\partial x_i}\mathrm{d}x_i, \tag{1.3}$$

where $\gamma_{ji} = \partial u_j / \partial x_i \ll 1$ is the distortion. Let us denote by $\mathrm{d}l$ a distance between two given particles along the direction of a unit vector **m** before deformation. Then, to the linear order, the distance after deformation is

$$\mathrm{d}l' = \mathrm{d}l + \mathbf{m}\cdot\mathrm{d}\mathbf{u} = dl + \mathbf{m}\cdot(\mathrm{d}\mathbf{x}\cdot\nabla)\mathbf{u} = \mathrm{d}l\left(1 + m_i\varepsilon_{ij}m_j\right), \tag{1.4}$$

where

$$\varepsilon_{ij} = \frac{1}{2}\left(\frac{\partial u_i}{\partial x_j} + \frac{\partial u_j}{\partial x_i}\right) \tag{1.5}$$

is the strain tensor representing the symmetric part of the distortion. The diagonal components of ε_{ij} define extensions along principle directions and the non-diagonal ones describe a shear.

When the medium is deformed, internal stresses appear that 'try' to restore the equilibrium of the medium. The stress tensor σ_{ij} is defined by the formula

$$\sigma_{ij} = \lim_{\Delta S\to 0}\frac{\Delta F_i}{\Delta S_j}, \tag{1.6}$$

where ΔF_i is the i^{th} component of the force applied to the surface element ΔS_j normal to the vector n_j. Due to the balance of the moment of forces applied to the element of volume, the tensor σ_{ij} is symmetric. The traction force vector **t** per unit surface area has the components

$$t_i(\mathbf{n}) = \sigma_{ij}n_j, \tag{1.7}$$

one of which is normal and two others tangential with respect to a given surface element.

1.3 Stiffness tensor

The relation between stresses and strains in linear elastodynamics is described by the first order term of the Taylor expansion of the stress $\sigma_{ij}\left(\varepsilon_{kl}\right)$ with respect to infinitesimal deformation ε_{kl},

$$\sigma_{ij}\left(\varepsilon_{kl}\right) = \sigma_{ij}\left(0\right) + \left(\frac{\partial\sigma_{ij}}{\partial\varepsilon_{kl}}\right)_{\varepsilon_{kl}=0}\varepsilon_{kl} + \ldots \tag{1.8}$$

For $\sigma_{ij}\left(0\right) = 0$,

$$\sigma_{ij} = c_{ijkl}\varepsilon_{kl}, \tag{1.9}$$

where

$$c_{ijkl} = \left(\frac{\partial \sigma_{ij}}{\partial \varepsilon_{kl}}\right)_{\varepsilon_{kl}=0}. \tag{1.10}$$

Relation (1.9) is *Hook's law*, called after Robert Hook who first established a dependence between stresses and strains for the case of bar tension. Elastic stiffness tensor is a tensor of the fourth order with the following symmetries in permutation of indices:

$$\begin{aligned} c_{ijkl} &= c_{jikl}\,(\text{because } \sigma_{ij} = \sigma_{ji}),\\ c_{ijkl} &= c_{ijlk}\,(\text{because } \varepsilon_{kl} = \varepsilon_{lk}),\\ c_{ijkl} &= c_{klij}\,\big(\text{thermodynamic law}\big). \end{aligned} \tag{1.11}$$

Expressing strains through displacement, we can write Hook's law in the following form:

$$\sigma_{ij} = \frac{1}{2}c_{ijkl}\frac{\partial u_k}{\partial x_l} + \frac{1}{2}c_{ijkl}\frac{\partial u_l}{\partial x_k}. \tag{1.12}$$

Due to the symmetry $c_{ijkl} = c_{ijlk}$, (1.12) becomes

$$\sigma_{ij} = c_{ijkl}\frac{\partial u_l}{\partial x_k}. \tag{1.13}$$

The number of components of an arbitrary tensor of the fourth rank without any symmetry in indices is $3^4 = 81$. Thanks to the symmetry $(1.11)_1$ and $(1.11)_2$, the number of elastic constants reduces to 36. Symmetry property $(1.11)_3$ further reduces the number of elastic constants from 36 to 21. Symmetry in pairs of indices also enables introducing abbreviated or matrix indices according to the rule

$$\begin{array}{ccc} \big(11\big) \leftrightarrow 1 & \big(22\big) \leftrightarrow 2 & \big(33\big) \leftrightarrow 3 \\ \big(23\big) = \big(32\big) \leftrightarrow 4 & \big(31\big) = \big(13\big) \leftrightarrow 5 & \big(12\big) = \big(21\big) \leftrightarrow 6. \end{array} \tag{1.14}$$

1.4 Elastodynamics equations

Acoustic perturbation in the elastic medium is governed by two fundamental equations, which are the equation of motion (resulting from Newton's law) and Hook's law (1.13):

$$\begin{cases} \rho \dfrac{\partial^2 u_i}{\partial t^2} = \dfrac{\partial \sigma_{ij}}{\partial x_j} + f_i, \\ \sigma_{ij} = c_{ijkl} \dfrac{\partial u_k}{\partial x_l}, \end{cases} \tag{1.15}$$

where ρ is the density and f_i is the volume source.

We confine in the following to the generalized plane strain setup and quasi-plane wave modes. Consider the acoustic field $\mathbf{u}(x_1, x_2)$ depending on the coordinates in the sagittal plane $X_1 X_2$. Unless otherwise specified, the material is assumed homogeneous in the X_1-direction and either inhomogeneous in the X_2-direction or possessing boundaries orthogonal to X_2. In such a case, the displacement can be sought in the form

$$\mathbf{u}(x_1, x_2, t) = \mathbf{A}(x_2) \exp\left[\mathrm{i}\left(k_1 x_1 - \omega t\right)\right]. \tag{1.16}$$

1.5 Wave equation

This section presents two different ways of formulating the wave equation from the system of elastodynamics equations (1.15).

1.5.1 Christoffel equation

Substituting σ_{ij} from the second of Eqs. (1.15) into the first one provides a system of three second-order differential equations with generally non-constant coefficients

$$\rho \frac{\partial^2 u_i}{\partial t^2} = c_{ijkl} \frac{\partial^2 u_k}{\partial x_j \partial x_l} + \frac{\partial c_{ijkl}}{\partial x_j} \frac{\partial u_k}{\partial x_l}. \tag{1.17}$$

Let the material be homogeneous ($\rho, c_{ijkl} = const$). Then the last term in Eq. (1.17) disappears and it reduces to a canonic system of hyperbolic equations with constant coefficients

$$\rho \frac{\partial^2 u_i}{\partial t^2} = c_{ijkl} \frac{\partial^2 u_l}{\partial x_j \partial x_k}. \tag{1.18}$$

Eq. (1.18) admits the solutions in the form of a plane wave

$$\mathbf{u}(\mathbf{x}, t) = A\mathbf{P} \exp\left[\mathrm{i}\left(\mathbf{k} \cdot \mathbf{x} - \omega t\right)\right], \tag{1.19}$$

where A is an amplitude and $\mathbf{P}$ a unit polarization vector. The wave propagates along the direction $\mathbf{n} = \mathbf{k} / \left|\mathbf{k}\right|$. Plugging (1.19) into (1.18) leads to the algebraic eigenvalue problem

$$\left(\Gamma_{il} - \rho V^2 \delta_{il}\right) P_l = 0, \tag{1.20}$$

where

$$\Gamma_{il} = c_{ijkl} n_j n_k \tag{1.21}$$

and $V = \omega / |\mathbf{k}|$ is the phase velocity determined from the characteristics polynomial

$$\left|\Gamma_{ij} - \rho V^2 \delta_{ij}\right| = 0. \tag{1.22}$$

Eq. (1.20) is called the *Christoffel equation* and the 3×3 matrix Γ_{il} is called the *Christoffel matrix*. It is a symmetric matrix because of the symmetry of c_{ijkl} in indices, see $(1.11)_3$. Moreover, Γ_{il} is positive definite and so its eigenvalues ρV^2 are both real and positive.

Thus, Eq. (1.20) shows that any direction **n** admits propagation of three wave modes with generally orthogonal linear polarizations **P** (eigenvectors of symmetric Γ_{il}). The exceptional case is when two eigenvalues of Γ_{il} and hence the phase velocities of two modes coincide. Then the corresponding pair of eigenvectors **P** does not have to be mutually orthogonal. Recall, for example, an isotropic material, where the longitudinal mode is polarized along the direction of propagation, while two transverse modes are polarized arbitrarily in the plane orthogonal to the propagation direction and may combine into a wave with any elliptical polarization in this plane. For the anisotropic case, there also exist particular directions, called acoustic axes, where two phase velocities coincide. The coincidence of phase velocities of all three modes in anisotropic media is a pure theoretical possibility.

1.5.2 SH and P/SV waves

Eq. (1.17) can be written in the form

$$\rho \frac{\partial^2 u_i}{\partial t^2} = \frac{\partial}{\partial x_j}\left(c_{ijkl} \frac{\partial}{\partial x_k}\right) u_l, \tag{1.23}$$

where

$$\Gamma_{il} = \frac{\partial}{\partial x_j}\left(c_{ijkl} \frac{\partial}{\partial x_k}\right) \tag{1.24}$$

will be called a *generalized Christoffel tensor* in view of the possible inhomogeneity of material. Let us consider the elastic wave propagation in the symmetry plane $X_1 X_2$ of a monoclinic material whose properties do not depend on x_3. Applying this symmetry plane to

the tensor c_{ijkl} referred to the base $\{X_1, X_2, X_3\}$ means that each component c_{ijkl} with an odd number of entries of "3" in its indices is equal to minus itself and hence is zero. Adding into consideration independence of c_{ijkl} from x_3 leads to

$$\Gamma_{i3} = \Gamma_{3l} = 0 \ for \ i,l = 1,2. \tag{1.25}$$

In other words, the generalized Christoffel tensor takes the form

$$\Gamma_{il} = \begin{pmatrix} \times & \times & 0 \\ \times & \times & 0 \\ 0 & 0 & \times \end{pmatrix}, \tag{1.26}$$

where the symbol $\times$ implies a non-zero component. Thus, if X_1X_2 is a symmetry plane and the material parameters are independent (at least) of x_3, then the vector wave equation (1.23) couples a scalar equation for a transverse wave $\mathbf{u} \parallel X_3$ which is called the *SH* (shear horizontal) wave. Two other equations define coupled waves polarized in the plane X_1X_2 and called *P/SV* (pressure/shear vertical) waves. If the material is homogeneous and the plane waves (1.19) are considered, then this property is attributed to any propagation direction **n** in the symmetry plane X_1X_2.

1.5.3 SH wave equation in the form of a first-order ODS

Consider a monoclinic medium with a symmetry plane denoted as the plane X_1X_2. Suppose that the material properties vary along one direction of this plane and take this direction as the axis X_2. Then the SH wave propagating in the plane X_1X_2 and polarized along X_3 satisfies the elastodynamics equations (1.15), which in the absence of volume sources reduce to the form

$$\begin{cases} \rho \dfrac{\partial^2 u_3}{\partial t^2} = \dfrac{\partial \sigma_{3j}}{\partial x_j}, \\ \sigma_{3j} = c_{3jkl} \dfrac{\partial u_k}{\partial x_l}. \end{cases} \tag{1.27}$$

Seeking the SH waves in the form (1.16) and hence replacing $\partial / \partial x_1 \to ik_1, \partial / \partial t \to -i\omega$ allows rewriting (1.27) as

$$\begin{cases} -\rho\omega^2 u_3 = \mathrm{i}k_1\sigma_{31} + \dfrac{\partial\sigma_{32}}{\partial x_2}, \\ \sigma_{31} = \mathrm{i}k_1 c_{55} u_3 + c_{45}\dfrac{\partial u_3}{\partial x_2}, \\ \sigma_{32} = \mathrm{i}k_1 c_{45} u_3 + c_{44}\dfrac{\partial u_3}{\partial x_2}, \end{cases} \tag{1.28}$$

where the matrix indices (1.14) are used for stiffness components and the symmetry $c_{45} = c_{54}$ is utilized. Keeping $(1.28)_3$ as it is and substituting $(1.28)_2$ in $(1.28)_1$ leaves us with two equations

$$\begin{cases} \dfrac{\partial u_3}{\partial x_2} = -\mathrm{i}\omega s\dfrac{c_{45}}{c_{44}}u_3 + \dfrac{1}{c_{44}}\sigma_{32}, \\ \dfrac{\partial\sigma_{32}}{\partial x_2} = -\left[\rho - s^2(c_{55} - \dfrac{c_{45}^2}{c_{44}})\right]\omega^2 u_3 - \mathrm{i}\omega s\dfrac{c_{45}}{c_{44}}\sigma_{32}, \end{cases} \tag{1.29}$$

where $s = k/\omega$ is the slowness. Hereafter in this thesis we specialize the notations as follows:

$$\begin{aligned} &x = x_1,\ y = x_2,\ k = k_1,\ v = \omega/k,\ s = k/\omega, \\ &u_3(x,y) = U(y)\mathrm{e}^{\mathrm{i}(kx-\omega t)},\ \sigma_{32}(x,y) = F(y)\mathrm{e}^{\mathrm{i}(kx-\omega t)}. \end{aligned} \tag{1.30}$$

Rewriting (1.29) via the notations (1.30) and omitting the exponential factors yields

$$\begin{cases} \dfrac{dU(y)}{dy} = -s\dfrac{c_{45}}{c_{44}}\mathrm{i}\omega U(y) + \dfrac{1}{c_{44}}F(y), \\ \dfrac{dF(y)}{dy} = \mathrm{i}\omega\left[\rho - s^2(c_{55} - \dfrac{c_{45}^2}{c_{44}})\right]\mathrm{i}\omega U(y) - \mathrm{i}\omega s\dfrac{c_{45}}{c_{44}}F(y). \end{cases} \tag{1.31}$$

Premultiplying $(1.31)_1$ by $\mathrm{i}\omega$ leads to the desired ODS in a matrix form

$$\frac{\mathrm{d}\boldsymbol{\eta}}{\mathrm{d}y}(y) = \mathbf{Q}(y)\boldsymbol{\eta}(y), \tag{1.32}$$

where

$$\boldsymbol{\eta}(y) = \begin{pmatrix} \mathrm{i}\omega U(y) \\ F(y) \end{pmatrix}, \quad \mathbf{Q}(y) = \mathrm{i}\omega\begin{pmatrix} -s\dfrac{c_{45}}{c_{44}} & \dfrac{1}{c_{44}} \\ \rho - s^2(c_{55} - \dfrac{c_{45}^2}{c_{44}}) & -s\dfrac{c_{45}}{c_{44}} \end{pmatrix}. \tag{1.33}$$

The state vector $\boldsymbol{\eta}(y)$ involves the SH displacement and traction, and the system matrix $\mathbf{Q}(y)$ depends on y if so do the material properties $\rho = \rho(y)$ and $c_{\alpha\beta} = c_{\alpha\beta}(y)$ with $\alpha,\beta = 4,5$.

We have thus demonstrated that the second-order differential equations (1.27) for the SH waves in a homogeneous or 1D-inhomogeneous medium can be transformed to the first-order ODS (1.32) with respect to the state vector involving the displacement and traction. Generalization of a state-vector formulation for vector waves in homogeneous or 1D-inhomogeneous media of unrestricted anisotropy is based on the Stroh formalism, which is outlined next.

1.5.4 Stroh formalism

In 1962, A.N. Stroh developed an elegant and effective formalism to tackle two-dimensional problems in elastodynamics [4, 5]. Given a general anisotropy, it leads to Eq. (1.32) that takes the form of a system of six equations with the 6×6 system matrix $\mathbf{Q}(y)$ constructed from the Stroh matrix

$$\mathbf{N}(y)=\begin{pmatrix}\mathbf{N_1} & \mathbf{N_2}\\ \mathbf{N_3} & \mathbf{N_4}\end{pmatrix},\quad \begin{matrix}\mathbf{N}_1=-(nn)^{-1}(nm), & \mathbf{N}_2=-(nn)^{-1},\\ \mathbf{N}_3=(mm)-(mn)(nn)^{-1}(nm), & \mathbf{N}_4=\mathbf{N}_1^{\mathrm{T}},\end{matrix} \tag{1.34}$$

which is written via the Lothe-Barnett [6] notations $(ab)_{jk}=a_i c_{ijkl} b_l$ with $\mathbf{a},\mathbf{b}=\mathbf{n}$ or $\mathbf{m}$, where $\mathbf{m}$ and $\mathbf{n}$ are the unit vectors along the X_1 and X_2 axes. Different explicit definitions of the state vector $\boldsymbol{\eta}(y)$ in (1.32) provide different forms of $\mathbf{Q}(y)$. For instance, the parameterisation through s,ω gives

$$\boldsymbol{\eta}(y)=\begin{pmatrix}\mathrm{i}\omega A(y)\\ F(y)\end{pmatrix},\qquad \mathbf{Q}(y;\omega,s)=\mathrm{i}\omega\begin{pmatrix}s\mathbf{N}_1 & -\mathbf{N}_2\\ -s^2\mathbf{N}_3+\rho\mathbf{I} & s\mathbf{N}_1^{\mathrm{T}}\end{pmatrix}. \tag{1.35}$$

which is often termed as the Thompson-Haskell formulation [7, 8]. Eq. (1.33) is a particular case of (1.35) for the SH waves.

1.6 Conclusion

In this chapter we have briefly presented the basic concepts of anisotropic elastodynamics. The wave equation was recast in the form of a first-order ordinary differential system (ODS) using the state-vector approach. This writing proves to be convenient for the 1D-inhomogeneous media, particularly in the case of continuous inhomogeneity. The analysis of SH waves in periodically inhomogeneous structures, carried out in the next chapter, is based on the wave equation in the form of a first-order ODS (1.32).

References

1. D. Royer, E. Dieulesaint, Ondes élastiques sans les solides, Masson, Paris, 1996.

2. A.L. Shuvalov, O. Poncelet, M. Deschamps, General formalism for plane guided waves in transversely inhomogeneous anisotropic plates, Wave Motion 40 (2004) 413-426.

3. C. Baron, O. Poncelet, A.L. Shuvalov, M. Deschamps, Propagation in Continuously Stratified Media, Chap. 4 in "Materials and Acoustics Handbook", ISTE-Wiley, London (2009) 97-112.

4. A.N. Stroh, Steady state problems in anisotropic elasticity, J. Math. Phys. 41 (1962) 77-103.

5. T.C.T. Ting, Anisotropic Elasticity. Theory and Applications, New York/Oxford, Oxford University Press, 1996.

6. J. Lothe, D.M. Barnett, On the existence of surface-wave solutions for anisotropic elastic half-space with free surface, J. Appl. Phys. 47 (1976) 428-433.

7. W.T. Thomson, Transmission of elastic waves through a stratified solid medium, J. Appl. Phys. 21 (1950) 89-93.

8. N.A. Haskell, The dispersion of surface waves on multilayered media, Bull. Seismol. Soc. Am. 43 (1953) 377-393.

2 SH waves in vertically periodic structures. Existence and non-existence of SH surface waves

Table of contents

2.1 Introduction

In this chapter we consider SH wave propagation in the structures, whose material properties vary periodically (continuously or discretely) along one direction that is orthogonal to the unit-cell interfaces. In this context, we will first introduce a matricant, solution of the first-order ordinary differential system with varying or constant coefficients [1]. The matricant lends a convenient tool for analyzing wave propagation in 1D-inhomogeneous media. For the case of periodic material properties, the basic concepts of the Floquet-Bloch theory, such as the passbands and stopbands, are intimately related to the matricant over a period that is called a monodromy matrix. On this basis, we will derive and analyze solutions for the periodic plates, halfspaces and strips. First, we touch upon the problem of SH waves in a periodic plate which underlies the further development aimed at the SH surface waves in a vertically periodic halfspace. We also consider the case of a periodic strip. Hereafter, we assume the orthorhombic material symmetry so that $c_{45} = 0$. In fact, all the results can be generalized for the monoclinic case [2].

The main attention will be devoted to the *SHSW (SH surface waves)*. In general, the surface acoustic waves acquire some particular features when the material properties have a periodic dependence along the vertical axis directed into the depth of the medium. In such a case, the surface-wave dispersion branches may extend down to zero horizontal slowness and they may come about in the form of randomly broken intervals. Further specificity characterizes the spectra of SHSW propagating in a vertically periodic halfspace with a vertical symmetry plane. It is that the branches of 'physical' and 'non-physical' SHSW, attributed as such due to their decrease or increase into the depth, are the alternating intervals of the dispersion curves of actually another spectrum, namely, the spectrum for guided waves in a single unit cell (period) considered as a free layer. This property has been noted for periodic stacks of homogeneous layers [3-7] and generalized for an arbitrary continuous or piecewise continuous vertically periodic media [8]. The problem of finding SHSW reduces therefore to calculating the dispersion branches of a free unit-cell layer and to identifying their spectral ranges which render the wave 'physical'.

Generally speaking, the SHSW may be expected to exist along some unordered 'fragments' of the dispersion branches of reference unit-cell spectrum and these can be determined only through a numerical procedure of testing the radiation condition.

Interestingly though, the spectral ranges of surface-wave existence can often be predicted without any calculations, by merely inspecting certain basic benchmarks of a given profile of variation of material constants over unit cell. Moreover, the dispersion spectrum of SHSW for a broad class of inhomogeneity profiles appears to be perfectly regular in that it is confined in between certain velocity bounds. A direct link between the profile shape and the surface-wave existence is especially compelling when the material properties are monotonic over a period. For instance, if the velocity and impedance of the shear bulk waves are both decreasing over a period, then the range of existence of SHSW on the dispersion curves is 'squeezed' to a narrow velocity window, which actually admits a simple and explicit evaluation. For an inverse, increasing profile the surface wave does not exist in this window and exists elsewhere. An analytical proof relies on the properties of the ordinary differential equation with periodically varying coefficients which governs the SHSW propagation in the (ω, k) space. Such spectral selectivity may be interesting for applications.

2.2 Matricant solution for SH waves. Peano series

A fundamental solution (an integral matrix) to the ODS (1.39) is defined to within a multiplication by any non-singular constant matrix on the right hand side. Denote an arbitrary integral matrix by $\mathbf{X}(y)$. Then

$$\mathbf{M}(y, y_0) = \mathbf{X}(y)\mathbf{X}^{-1}(y_0), \tag{2.1}$$

is also an integral matrix such that yields

$$\mathbf{M}(y_0, y_0) = \mathbf{I}, \tag{2.2}$$

where $\mathbf{I}$ is identity matrix. This particular integral matrix is called a matricant. It is also often called a propagator, for it has a property of 'propagating' any partial vector solution (state vector) from one coordinate to another

$$\boldsymbol{\eta}(y) = \mathbf{M}(y, y_0)\boldsymbol{\eta}(y_0). \tag{2.3}$$

For the case of SH waves, the matricant is a 2x2 matrix. It expands into the Peano series of multiple integrals [1, 9, 10]

$$\mathbf{M}(y, y_0) = \begin{pmatrix} M_1(y, y_0) & M_2(y, y_0) \\ M_3(y, y_0) & M_4(y, y_0) \end{pmatrix} = \mathbf{I} + \int_{y_0}^{y} \mathbf{Q}(y_1)\,\mathrm{d}y_1 + \int_{y_0}^{y}\int_{y_0}^{y_1} \mathbf{Q}(y_1)\mathbf{Q}(y_2)\,\mathrm{d}y_1\mathrm{d}y_2 \ldots \tag{2.4}$$

Eq. (2.4) remains valid for a piecewise continuous $\mathbf{Q}(y)$ provided $\boldsymbol{\eta}(y)$ stays continuous. A matricant satisfies the chain rule

$$\mathbf{M}(y,y_0)=\mathbf{M}(y,y_1)\mathbf{M}(y_1,y_0), \tag{2.5}$$

which may be handy when $\mathbf{Q}(y)=const$ in $\left[y_1,y_2\right]\in\left[y_0,y_1\right]$ and hence

$$\mathbf{M}(y_2,y_1)=\exp\left[(y_2-y_1)\mathbf{Q}\right]. \tag{2.6}$$

In particular, $\mathbf{M}(y,y_0)$ is a product of exponentials when $\mathbf{Q}(y)$ is piecewise constant in $\left[y_0,y_1\right]$. For the case of real ω and k considered in the thesis, it follows from (2.4) and (1.35) that [2]

$$M_1,M_4 \text{ are real; } M_2,M_3 \text{ are imaginary.} \tag{2.7}$$

Either of the symmetry planes X_1X_3 or X_2X_3 suffices to ensure that the matricant is a unimodular matrix [2]

$$\det\mathbf{M}=1. \tag{2.8}$$

2.3 Periodicity. Passbands and stopbands

Let us specify the inhomogeneity along Y as periodic, so that $\mathbf{Q}(y)=\mathbf{Q}(y+T)$ where T denotes the least period. Each unit cell $y\in\left[0,T\right]$ may be a stack of different homogeneous or inhomogeneous layers in welded contact maintaining continuity of $\boldsymbol{\eta}(y)$, or it may be a single continuously inhomogeneous layer. Two SH Floquet modes are associated with the eigenspectrum of the matricant $\mathbf{M}(T,0)$ through the period

$$\mathbf{M}(T,0)\,\mathbf{w}_\alpha=q_\alpha\mathbf{w}_\alpha\,(\alpha=1,2),\ \ q_{1,2}\equiv\mathrm{e}^{\mathrm{i}K_{1,2}T},\ \ q_1=1/q_2 \tag{2.9}$$

where K is the Floquet wavenumber [1]. It enables a handy expression for the unimodular matricant $\mathbf{M}(NT,0)$ through any number N of welded unit cells [11]

$$\begin{aligned}\mathbf{M}(NT,0)=\mathbf{M}^N(T,0)&=\frac{q_1^N-q_2^N}{q_1-q_2}\mathbf{M}(T,0)-\frac{q_1^{N-1}-q_2^{N-1}}{q_1-q_2}\mathbf{I}=\\&=\frac{\sin NKT}{\sin KT}\mathbf{M}(T,0)-\frac{\sin(N-1)KT}{\sin KT}\mathbf{I},\end{aligned} \tag{2.10}$$

which by continuity extends to the degenerate case $q_1=q_2$. Obviously,

$$\mathbf{M}(NT,0)\mathbf{w}_\alpha=q_\alpha^N\mathbf{w}_\alpha\,(\alpha=1,2). \tag{2.11}$$

For a given T, the matricant $\mathbf{M}(T,0)$ and hence its eigenvectors $\mathbf{w}_\alpha$ and eigenvalues q_α depend on ω and $s = k/\omega$. The plane $\{\omega, k\}$ is therefore mapped out into the passbands, where q_1 and q_2 are complex conjugated numbers of a unit absolute value (K is real), and the stopbands, where q_1 and q_2 are real (K is purely imaginary). The lines $q_1 = q_2 (= \pm 1)$ are the stopband edges.

2.4 SH waves in a periodic plate

Let the wave propagate in a plate of thickness h. From relation (2.3) and the notation (1.30) introduced in the Chapter 1 we write

$$\begin{pmatrix} \mathrm{i}\omega U(h) \\ F(h) \end{pmatrix} = \begin{pmatrix} M_1 & M_2 \\ M_3 & M_4 \end{pmatrix} \begin{pmatrix} \mathrm{i}\omega U(0) \\ F(0) \end{pmatrix}. \tag{2.12}$$

Applying traction free conditions to the top and bottom faces of the plate gives

$$\begin{pmatrix} \mathrm{i}\omega U(h) \\ 0 \end{pmatrix} = \begin{pmatrix} M_1 & M_2 \\ M_3 & M_4 \end{pmatrix} \begin{pmatrix} \mathrm{i}\omega U(0) \\ 0 \end{pmatrix}, \tag{2.13}$$

hence the dispersion equation is

$$M_3(\omega, k) = 0. \tag{2.14}$$

By analogy, Eq. (2.12) considered under the boundary conditions of either both faces being clamped $(U(0) = 0, U(h) = 0)$, or with one face clamped and the other free, leads, respectively, to the dispersion equations

$$M_2(\omega, k) = 0 \quad \text{and} \quad M_1(\omega, k) = 0 \text{ or } M_4(\omega, k) = 0. \tag{2.15}$$

In this thesis we consider traction-free conditions, which provide the dispersion equation (2.14). Hence, by (2.3) and (2.10), the dispersion equation for the SH guided waves in a free periodic layer $y \in [0, NT]$ with a period T is

$$M_3(NT, 0) = \frac{\sin NKT}{\sin KT} M_3(T, 0) = 0, \tag{2.16}$$

where $M_3(T,0) = 0$ is in turn the dispersion equation for a single unit cell extracted from the periodic structure and subjected to the traction-free condition at both faces $y = 0, T$. It is noted that the eigenvalues of $\mathbf{M}(T,0)$ with $M_3(T,0) = 0$ are

$$q_1 = M_1(T,0), \; q_2 = M_4(T,0), \tag{2.17}$$

which are both real according to (2.7) and have the same sign due to (2.8). Therefore, by (2.16), the dispersion spectrum for a finite periodic structure $y \in \left[0, NT\right]$ of N unit cells consists of the branches given by $M_3(T,0)$, which lie in the stopbands due to q_1, q_2 being real, and of the branches given by $\sin NKT = 0$ $(\sin KT \neq 0)$, which lie within the passbands (see Fig. 2.1).

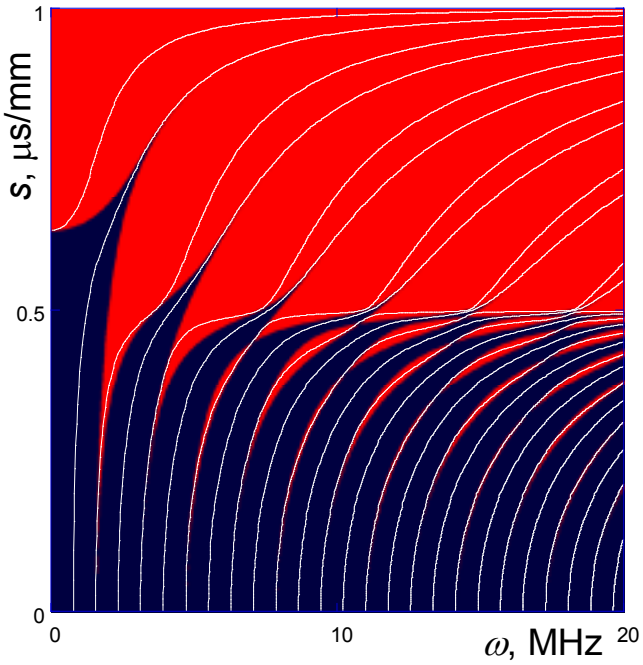

Fig. 2.1 *Dispersion curves in the* (s,ω) *plane for the plate consisting of two bilayered unit cells. Dispersion curves are overlaid onto the Floquet passbands (black zones) and stopbands (grey zones). The material parameters for the layers are* $\rho_1 = \rho_2 = 1\,g/cm^3, c_1 = 1\,mm/\mu s,\ c_2 = 2\,mm/\mu s$.

2.5 SH surface waves in a periodic halfspace

We pass to the case of SHSW propagation in a vertically periodic halfspace. First some general properties of SHSW are described. Then the cases of a piecewise homogeneous bilayered unit cell and a unit cell with an arbitrary monotonic profile are considered in detail.

2.5.1 Existence of surface waves

The SH surface wave in a vertically periodic halfspace must satisfy the condition $\sigma_{23} \sim F = 0$ on the traction-free surface $y = 0$ and also the radiation condition, which demands decrease of surface-wave amplitude into the depth. For the latter reason, the appropriate ('physical') wave solutions lie strictly inside the stopbands and correspond there to that one of two SH Floquet modes $\alpha = 1,2,$ for which the (real) eigenvalue of the

matricant over a period (the monodromy matrix) $\mathbf{M}(T,0)$ is such that $\left|q_\alpha\right|<1$. This inequality does imply that SH surface wave consists of a single Floquet mode but, on this grounds solely, it may yet be either the mode $\alpha=1$ or the mode $\alpha=2$. Now we recall the traction-free boundary condition $F(0)=0$. A single Floquet mode fulfils the latter condition at $y=0$, and simultaneously at all interfaces $y=NT$ (see (2.11)), if and only if it corresponds to the eigenvector $\mathbf{w}_\alpha$ of $\mathbf{M}(T,0)$ with an identically vanishing second (related to F) component. The required form $\mathbf{w}_\alpha \parallel \left(1,0\right)$ demands that $M_3(T,0)=0$ and, given so, it selects a single Floquet mode exceptionally as the mode $\alpha=1$, for which $M_3(T,0)=0$ implies $q_1=M_1(T,0)$. Thus, by (2.3) with $y_0=0$ and $\boldsymbol{\eta}(0)=U(0)\mathbf{w}_\alpha$, the wave amplitude at $y=NT$ after any number N of periods is $U(NT)=M_1^N(T,0)U(0)$. It remains now to come back to the aforementioned radiation condition $\left|q_\alpha\right|<1$ and to fix $\alpha=1$ in there, thus asking that

$$\left|U(T)\right|=\left|M_1(T,0)U(0)\right|<\left|U(0)\right|. \tag{2.18}$$

Recapping the above arguments, the dispersion spectrum for SHSW in a semi-infinite periodic structure is defined by a pair of conditions

$$\begin{cases} M_3(T,0)=0, \\ \left|M_1(T,0)\right|\left(=\left|M_4(T,0)\right|^{-1}\right)<1, \end{cases} \tag{2.19}$$

with the entries given by (2.4).

Thus, finding the SHSW spectrum amounts to a two-step procedure. The first step is using Eqs. $(2.19)_1$ and (2.4) to calculate the dispersion branches for SH guided waves in a free inhomogeneous layer $y\in\left[0,T\right]$ (see [8])), which is a single unit cell of a given structure. The SHSW may exist only somewhere along these branches. In the following they will be denoted as $\hat{v}_n(\omega)$ or $\hat{s}_n(\omega)$ (or $\hat{\omega}_n(k)$ as in Fig. 2.2, etc.), where the hat indicates that these are the 'reference' branches for the SHSW in the above-mentioned sense. The second step is applying the inequality $(2.19)_2$ to identify the spectral intervals on the SHSW existence on the reference branches. The reference dispersion branches (in the form of a frequency versus wavenumber dependence) and their partitioning into the ranges of SHSW existence and non-existence are exemplified in Fig. 2.2. An important property of the SH case is that inverting unit-cell profile swaps the SHSW existence and non-existence. This follows from the general identity $\mathbf{M}\left(y,y_0\right)=\mathbf{T}\mathbf{M}_{\mathbf{Q}(-y)}\left(-y_0,-y\right)\mathbf{T}$, where $\mathbf{M}_{\mathbf{Q}(-y)}$ is the matricant for Eq. (2.3) with

$\mathbf{Q}(-y)$ in the place of $\mathbf{Q}(y)$, and $\mathbf{T}$ is the matrix with zero diagonal and unit off-diagonal blocks (components for the 2x2 case in hand). In consequence, inverting an arbitrary profile of unit cell $\left[0,T\right]$ about its middle point (in other words, turning the periodic structure 'upside down') amounts to interchanging the components M_1 and M_4 of $\mathbf{M}(T,0)$. Hence, this transformation keeps intact the reference dispersion branches (say, $\hat{v}_n(\omega)$ or $\hat{s}_n(\omega)$) defined by $(2.19)_1$, but inverts the sense of their partitioning into the intervals of SHSW existence and non-existence, i.e., formerly 'physical' solutions become 'non-physical' and vice versa. This feature is referred to below as the reciprocity property.

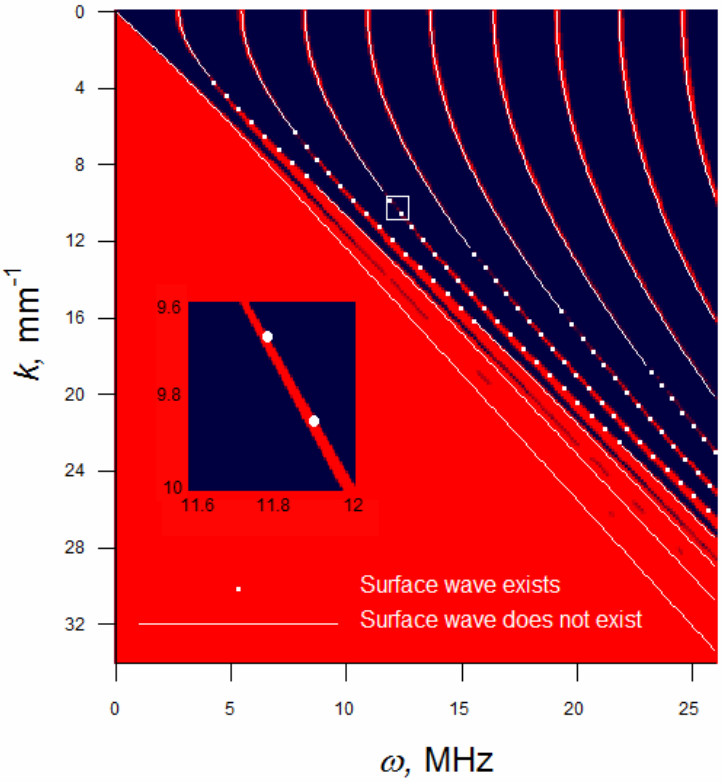

Fig. 2.2 *Dispersion curves of a free unit cell calculated in the (ω,k) plane and overlayed onto the Floquet passbands (black zones) and stopbands (grey zones). The stopbands near cutoffs are narrow and therefore not well resolved to the scale of the plot (see a zoomed inset). The ranges of the SHSW existence and non-existence are indicated here by the dotted and solid lines (identifying these ranges is the purpose of the analysis following below in this Chapter).*

The general problem of existence and non-existence of SHSW in a vertically periodic halfspace with an arbitrary unit-cell profile has been analyzed in [12]. The present study is focused on one of the most interesting cases, which is when the surface wave exists within only a single velocity window and does not exist elsewhere or vice versa. This occurs in particular if the variation of material properties over unit cell is monotonic, either piecewise

continuous or discrete. We start by considering the case of a unit cell consisting of two homogeneous layers. Obviously, such a cell is always 'discretely monotonic'.

2.5.2 Bilayered unit cell

Consider the case when the halfspace is a stack of periodically repeated pairs of homogeneous layers of thicknesses d_1 and d_2. First, we introduce the auxiliary notations as follows

$$\begin{aligned} &c_{\|j} = 1\big/ s_{\|j} = \sqrt{c_{55}^{(j)}\big/\rho_j}\,,\ \ c_{\perp j} = 1\big/ s_{\perp j} = \sqrt{c_{44}^{(j)}\big/\rho_j},\ \ z_{\perp j} = \rho_j c_{\perp j}, \\ &\kappa_j = \omega s_{\perp j}\sqrt{1 - c_{\|j}^2 \hat{s}_n^2(\omega)},\ \ \psi_j = \kappa_j d_j,\, Z_j = z_{\perp j}\sqrt{1 - c_{\|j}^2 \hat{s}_n^2(\omega)}, \end{aligned} \tag{2.20}$$

where $j = 1,2$ and κ_j is the vertical component of the wave vector. The matricant for a homogeneous layer is an exponential of the system matrix $\mathbf{Q}_j$ of this layer (see (2.6)), and, by (2.5), the matricant over a period (the monodromy matrix) is

$$\begin{aligned} \mathbf{M}(T,0) = \mathbf{M}^{(2)}\mathbf{M}^{(1)} = \mathrm{e}^{\mathbf{Q}_2 d_1}\mathrm{e}^{\mathbf{Q}_1 d_2} = \\ = \begin{pmatrix} \cos\kappa_1 d_1 & \dfrac{\mathrm{i}}{Z_1}\sin\kappa_1 d_1 \\ \mathrm{i}Z_1\sin\kappa_1 d_1 & \cos\kappa_1 d_1 \end{pmatrix}\begin{pmatrix} \cos\kappa_2 d_2 & \dfrac{\mathrm{i}}{Z_2}\sin\kappa_2 d_2 \\ \mathrm{i}Z_2\sin\kappa_2 d_2 & \cos\kappa_2 d_2 \end{pmatrix} = \\ = \begin{pmatrix} \cos\psi_2\cos\psi_1 - \dfrac{Z_1}{Z_2}\sin\psi_2\sin\psi_1 & \mathrm{i}\left(\dfrac{1}{Z_1}\cos\psi_2\sin\psi_1 + \dfrac{1}{Z_2}\sin\psi_2\cos\psi_1\right) \\ \mathrm{i}\left(Z_2\cos\psi_1\sin\psi_2 + Z_1\sin\psi_1\cos\psi_2\right) & \cos\psi_2\cos\psi_1 - \dfrac{Z_2}{Z_1}\sin\psi_2\sin\psi_1 \end{pmatrix}. \end{aligned} \tag{2.21}$$

By (2.21), the dispersion equation (2.14) may be written in the form

$$Z_2\cos\psi_1\sin\psi_2 + Z_1\sin\psi_1\cos\psi_2 = 0, \tag{2.22}$$

and the matricant considered along a dispersion branch $\hat{s}_n(\omega)$ (or $\hat{v}_n(\omega)$) takes the form

$$\mathbf{M}(T,0) \equiv \begin{pmatrix} M_1 & M_2 \\ M_3 & M_4 \end{pmatrix} = \begin{pmatrix} \cos\psi_1/\cos\psi_2 & \dfrac{\mathrm{i}}{Z_1}\sin\left(\psi_1 - \psi_2\right)\sin\left(\psi_1 + \psi_2\right) \\ 0 & \cos\psi_2/\cos\psi_1 \end{pmatrix}. \tag{2.23}$$

Let us analyse conditions for the existence of SHSW. First consider the so-called *subsonic domain* of wave speed where $v < \max(c_{\|1}, c_{\|2})$ (note that $\hat{v}_n(\omega) > \min(c_{\|1}, c_{\|2})$). We will show that the SHSW in a periodically bilayered halfspace either exist or do not exist throughout the whole subsonic domain. Assume that, say, $c_{\|1} > c_{\|2}$, so that ψ_1 is pure imaginary and ψ_2 is real in the subsonic domain $v < c_{\|1}$. Therefore

$$\cos\psi_2 < \cos\psi_1 = \cosh\psi_1. \tag{2.24}$$

By Eqs. (2.23) and (2.17), the matricant eigenvalues along the dispersion branches $\hat{v}_n(\omega)$ are as follows

$$q_1 = M_1 = \frac{\cos\psi_1}{\cos\psi_2},\ q_2 = M_4 = \frac{\cos\psi_2}{\cos\psi_1} \tag{2.25}$$

(unless explicitly specified, the reference to $\hat{v}_n(\omega)$ is kept tacit below). From Eq. (2.24) and (2.25), it is seen that $|q_1| > 1$. Thus, taking into account Eq. $(2.19)_2$, we conclude that, for the case of a bilayered unit cell, the SHSW are 'non-physical' (i.e. do not exist) throughout the subsonic domain if $c_{\|1} > c_{\|2}$; hence otherwise, if $c_{\|1} < c_{\|2}$, the SHSW are 'physical' (exist) throughout the subsonic domain by virtue of the reciprocity property.

We now turn to the 'physical'/'non-physical' solutions in the so-called *supersonic domain* where $v > \max(c_{\|1}, c_{\|2})$. Note that the supersonic Z_j and ψ_j are real. Along the branches $\hat{v}_n(\omega)$ that are defined by the dispersion equation (2.14), Eqs. (2.21) and (2.22) yield

$$M_1 - M_4 = \frac{Z_2^2 - Z_1^2}{Z_1 Z_2}\sin\psi_1 \sin\psi_2 = \frac{Z_1^2 - Z_2^2}{Z_2^2}\sin^2\psi_1 \frac{\cos\psi_2}{\cos\psi_1}. \tag{2.26}$$

By (2.25), $\cos\psi_1\cos\psi_2 \gtrless 0$ implies $M_1, M_4 \gtrless 0$ (here and below the successive upper/lower inequality signs are in one-to-one correspondence; recall also that $\operatorname{sgn} M_1 = \operatorname{sgn} M_4$ at $M_3 = 0$). Suppose that $\cos\psi_1\cos\psi_2 > 0$ so that M_1, M_4 are positive. Then, according to (2.26), $Z_1 \gtrless Z_2$ means $M_1 \gtrless M_4$ and hence $|M_1| \gtrless |M_4|$. Now let $\cos\psi_1\cos\psi_2 < 0$ so that M_1, M_4 are negative. Then, according to (2.26), $Z_1 \gtrless Z_2$ means $M_1 \lesseqgtr M_4$ and hence again $|M_1| \gtrless |M_4|$. Thus, recalling the SHSW-existence criterion $(2.19)_2$, we conclude that the supersonic SHSW are 'physical' if $Z_1 < Z_2$ and 'non-physical' if $Z_1 > Z_2$, where $Z_j = Z_j\left(\hat{v}_n(\omega)\right)$.

The above-established condition $Z_1 < Z_2$ for the existence of supersonic SHSW is yet somewhat implicit. Let us specify its explicit form in terms of the material parameters. According to (2.20), the inequality between Z_1, Z_2 at the cutoffs $\hat{s}_n(\omega)\left(= 1/\hat{v}_n(\omega)\right) = 0$ is the same as between $z_{\perp 1}, z_{\perp 2}$. Moving away from the cutoffs along the dispersion branches switches the inequality between Z_1, Z_2 within the supersonic domain $v > \max(c_{\|1}, c_{\|2})$ if the curves Z_1 and Z_2 cross each other in there. Denote the root of equation

$$Z_1\left(\hat{v}_n(\omega)\right) = Z_2\left(\hat{v}_n(\omega)\right) \quad \Leftrightarrow \quad z_{\perp 1}\sqrt{1 - c_{\|1}^2/\hat{v}_n^2(\omega)} = z_{\perp 2}\sqrt{1 - c_{\|2}^2/\hat{v}_n^2(\omega)} \tag{2.27}$$

by

$$\nu_{12} = \sqrt{\frac{c_{\|2}^2 z_{\perp 2}^2 - c_{\|1}^2 z_{\perp 1}^2}{z_{\perp 2}^2 - z_{\perp 1}^2}}. \tag{2.28}$$

The curves Z_1 and Z_2 intersect in the supersonic domain at a point $\hat{v}_n(\omega) = \nu_{12}$, provided that ν_{12} is real and greater than $\max(c_{\|1}, c_{\|2})$. Assume for definiteness that $c_{\|1} > c_{\|2}$ and consider the ensuing possibilities. First, let $z_{\perp 1} > z_{\perp 2}$. Then $\nu_{12}^2 > c_{\|1}^2$ and hence there is an intersection of Z_1 and Z_2 at $\hat{v}_n(\omega) = \nu_{12} > c_{\|1}$. So, $Z_1 > Z_2$ from the cutoffs $\hat{v}_n(\omega) = \infty$ down to this point $\hat{v}_n(\omega) = \nu_{12}$, while $Z_1 < Z_2$ for $c_{\|1} < \hat{v}_n(\omega) < \nu_{12}$. Thus

$$\begin{aligned} Z_1 > Z_2 \text{ at } \nu_{12} < \hat{v}_n(\omega) < \infty &\Leftrightarrow \text{no SHSW in } \nu_{12} < \hat{v}_n(\omega) < \infty \\ Z_1 < Z_2 \text{ at } c_{\|1} < \hat{v}_n(\omega) < \nu_{12} &\Leftrightarrow \text{SHSW exist in } c_{\|1} < \hat{v}_n(\omega) < \nu_{12}. \end{aligned} \tag{2.29}$$

Now let $z_{\perp 1} < z_{\perp 2}$. (along with $c_{\|1} > c_{\|2}$). In this case, if $c_{\|2} z_{\perp 2} < c_{\|1} z_{\perp 1}$ then $0 < \nu_{12}^2 < c_{\|1}^2$, and if $c_{\|2} z_{\perp 2} > c_{\|1} z_{\perp 1}$ then $\nu_{12}^2 < 0$. Both these options imply that there is no crossing of Z_1 and Z_2 in the supersonic domain, where therefore the inequality between Z_1, Z_2 remains the same as between $z_{\perp 1}$, $z_{\perp 2}$. As a result,

$$Z_1 < Z_2 \text{ at } c_{\|1} < \hat{v}_n(\omega) < \infty \Leftrightarrow \text{no SHSW at } c_{\|1} < \hat{v}(\omega) < \infty. \tag{2.30}$$

Finally, an alternative initial assumption $c_{\|1} < c_{\|2}$ yields the precisely inverse predictions by virtue of the reciprocity property.

We are now in the position to conclude that a periodically bilayered halfspace admits two and only two possible types of SHSW spectral patterns. This overall prediction is as follows.

If $c_{\|1} > c_{\|2}$ and $z_{\perp 1} \le z_{\perp 2}$, then SHSW do not exist in the subsonic domain and exist in the supersonic domain.

If $c_{\|1} > c_{\|2}$ and $z_{\perp 1} > z_{\perp 2}$, then there is a velocity window of the SHSW-existence

$$\left(c_{\|2} <\right) c_{\|1} < v < \nu_{12}, \tag{2.31}$$

where ν_{12} is defined by (2.28). The lower and upper bounds of the SHSW-existence window are constant (non-dispersive) and exact. Beyond this window the SHSW do not exist.

Due to the reciprocity property, swapping the top and bottom layers within the bilayered unit cell leads to inverting existence and non-existence ranges in SHSW dispersion spectrum.

The two above types of SHSW spectra are exemplified in Figs. 2.3 and 2.4 (plotted in terms of the slowness versus frequency dependence). Note that the 'physical'/'non-physical' nature of SHSW changes precisely at the subsonic/supersonic threshold, where each dispersion branch touches the stopband edge. This is one of those particular features that comes about for, specifically, a bilayered unit cell and does not occur for 'discretely monotonic' unit cells consisting of more than two homogeneous layers. Further variety of options pertains to the case of an arbitrary piecewise homogeneous unit cell, for which the SHSW spectrum is generally irregular both in the subsonic and supersonic domain.

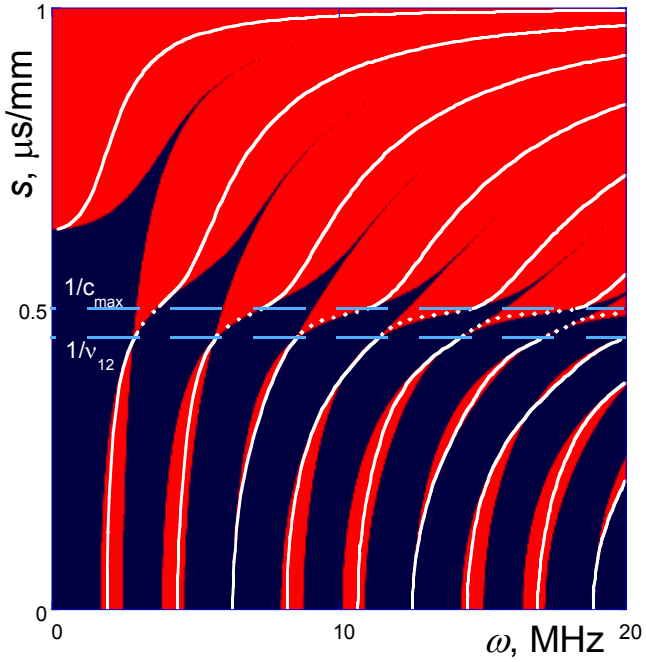

Fig. 2.3 *SHSW existence/non-existence for a bilayered halfspace: solid and dotted lines represent,respectively, non-physical and physical SHSW-solutions lying on the reference dispersion branches* $\hat{s}_n(\omega)$ *of a free unit cell (the latter are confined to the stopbands indicated by red). Dashed lines show the bounds of the spectral window of the SHSW- existence. The parameters of the layers are* $\rho_1 = \rho_2 = 1\,g/cm^3, c_{\|1} = 2\,mm/\mu s, c_{\|2} = 1\,mm/\mu s$ *, which corresponds to the case (2.29).*

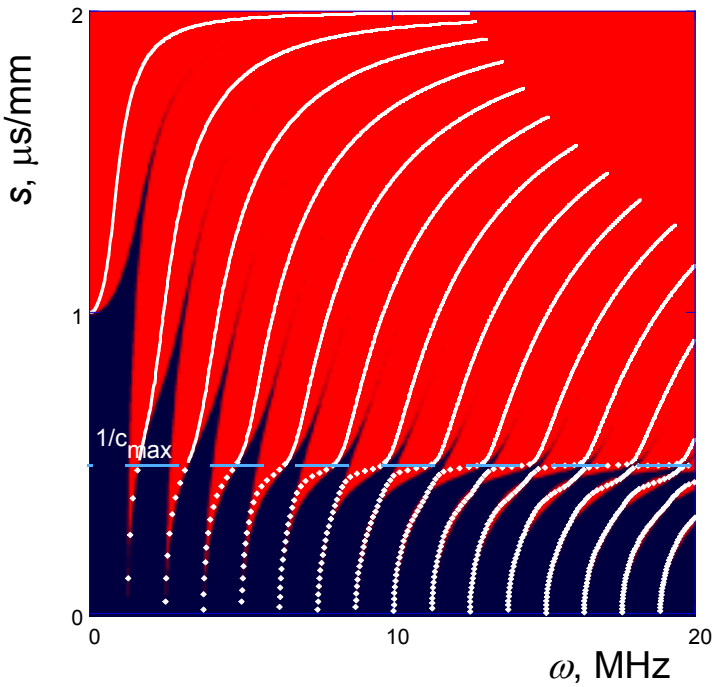

Fig. 2.4 *The same as in Fig. 2.3 for the bilayered unit cell with the parameters:* $\rho_1 = 1\,g/cm^3, \rho_2 = 4\,g/cm^3, c_{\|1} = 2\,mm/\mu s, c_{\|2} = 0,5\,mm/\mu s$. *This example corresponds to the case (2.30). The dashed line is the subsonic/supersonic threshold.*

2.5.3 Continuously inhomogeneous unit cell. The case of a monotonic profile

Let us consider a periodic halfspace, whose unit cell $y \in [0,T]$ is continuous and has different material properties at $y = 0$ and $y = T$ ($c_{\|}(0), z_{\perp}(0) \neq c_{\|}(T), z_{\perp}(T)$, using hereafter the same notations as in (2.20) but with an argument 'y' instead of a layer label 'j'). In fact, it can be shown that, regardless of the profile shape, the existence/non-existence of the supersonic SHSW may be inferred from knowing the values of $c_{\|}(y), z_{\perp}(y)$ solely at the edge points, namely, by comparing $c_{\|}(0)$ and $c_{\|}(T)$, $z_{\perp}(0)$ and $z_{\perp}(T)$. For instance, it can be shown that if $c_{\|}(0) > c_{\|}(T)$ and $z_{\perp}(0) < z_{\perp}(T)$, then the supersonic SHSW are confined to the velocity window

$$\left(c_{\|}(T) <\right) c_{\|}(0) < v < \nu_T, \tag{2.32}$$

where

$$\nu_T = \sqrt{\frac{c_{\|}^2(0) z_{\perp}^2(0) - c_{\|}^2(T) z_{\perp}^2(0)}{z_{\perp}^2(0) - z_{\perp}^2(T)}}. \tag{2.33}$$

The inverse statement for the case $c_{\|}(0) < c_{\|}(T)$ and $z_{\perp}(0) > z_{\perp}(T)$ follows from reciprocity property.

At the same time, it is worth underscoring that, in contrast to the case of a bilayered unit cell, the above estimate (2.32) of a supersonic spectral window for the case of a continuously inhomogeneous cell is approximate and becomes asymptotically exact only at high frequency. Another essential complication for the case of continuous inhomogeneity concerns the subsonic SHSW, which may exist within various, possibly irregular, spectral ranges. In this light, the more significant is the case of arbitrarily monotonic unit-cell profile, which yet provides a perfectly regular SHSW spectral patterns and can lead to their existence in a single velocity window.

According to [12], the following asymptotically valid predictions can be formulted for the case of a continuously inhomogeneous unit cell with a monotonic profile.

If $c_{\parallel}(0) > c_{\parallel}(T)$ *and* $z_{\perp}(0) < z_{\perp}(T)$, *then SHSW do not exist in the subsonic domain and exist in the supersonic domain.*

If $c_{\parallel}(0) > c_{\parallel}(T)$ *and* $z_{\perp}(0) > z_{\perp}(T)$, *then there is a velocity window* (2.32) *of the SHSW existence. Beyond this window the SHSW do not exist.*

The above properties are demonstrated in Fig. 2.5 for a simple example of a linear velocity profile of a unit cell $y \in [0, T]$ with the parameters:

$$c_{\parallel}(y) = c_0(2 - \frac{y}{2T}),\ c_0 = 1\,mm/\mu s,\ T = 1\,mm \quad (\rho = const = 1\,g/cm^3). \qquad (2.34)$$

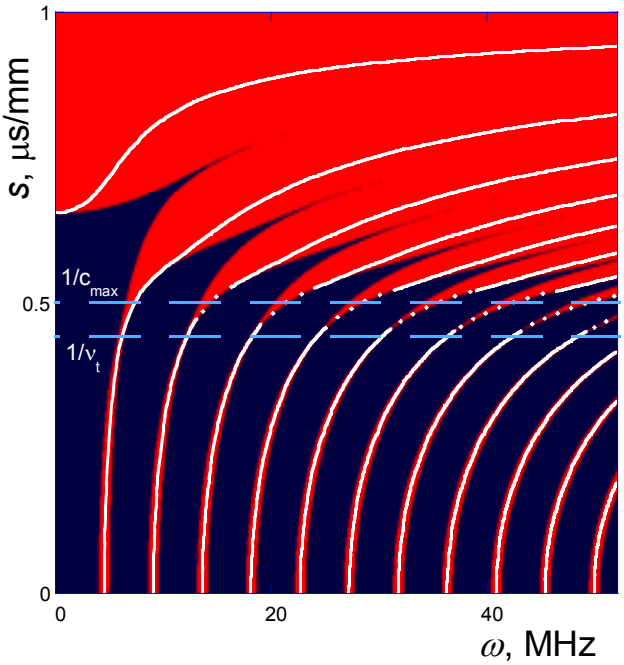

Fig. 2.5 *The same as in Fig. 2.3 for the continuously inhomogeneous and monotonic unit cell defined in (2.34).*

2.6 Periodic strip

Recall the SH-wave equation in the orthorhombic material with the material properties depending on the coordinate *y*:

$$c_{55}(y)\frac{\partial^2 u}{\partial x^2}+\frac{\partial}{\partial y}\left(c_{44}(y)\frac{\partial u}{\partial y}\right)=-\rho(y)\omega^2 u. \tag{2.35}$$

Consider a strip with traction-free faces $x=0,d$ and a traction-free edge $y=0$ (see Fig. 2.6), so that

$$\sigma_{13}(0,y)=0,\quad \sigma_{13}(d,y)=0,\quad \sigma_{23}(x,0)=0, \tag{2.36}$$

where $\sigma_{13}=c_{55}\partial u/\partial x$, $\sigma_{23}=c_{44}\partial u/\partial y$.

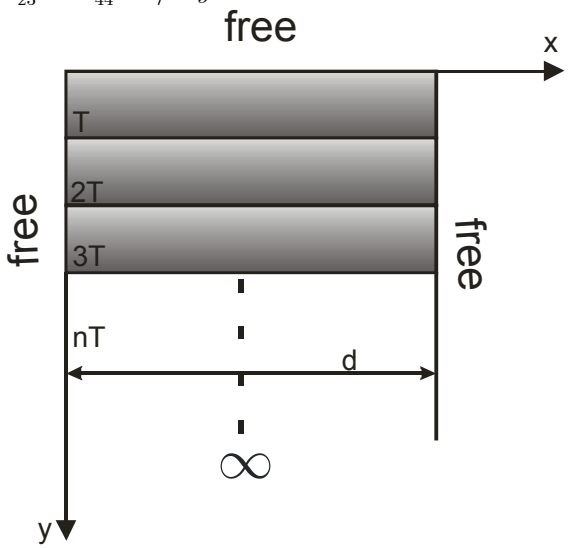

Fig. 2.6 *Periodic strip*

The scalar case of SH waves allows us to use instead the method of separation of variables. Assume a partial solution of the partial differential equation (2.35) in the form

$$u(x,y)=W_1(x)W_2(y). \tag{2.37}$$

Inserting (2.37) into (2.35) leads to two ordinary differential equations

$$\begin{cases} W_1''+k_x^2 W_1=0, \\ \left(c_{44}W_2'\right)'+\left(\rho\omega^2-k_x^2 c_{55}\right)W_2=0. \end{cases} \tag{2.38}$$

where $-k_x^2$ is a constant of variable separation. The solution to (2.35) with the boundary conditions (2.36) may be sought in the form

$$u_n(x,y)=W_2^{(n)}(y)\cos k_x^{(n)}(x-d), \tag{2.39}$$

where $W_1^{(n)}(x)=\cos k_x^{(n)}(x-d)$ with

$$k_x^{(n)} = \frac{\pi n}{d} \tag{2.40}$$

ensures that (2.39) fulfils the boundary conditions $(2.36)_{1,2}$ at $x = 0, d$. As discussed in Section 2.1, Eq. $(2.38)_2$ on $W_2^{(n)}(y)$ may be written as

$$\boldsymbol{\eta}^{(n)}(y) = \mathbf{M}(y, 0; \omega, k_x^{(n)})\boldsymbol{\eta}^{(n)}(0) \tag{2.41}$$

with respect to the state vector

$$\boldsymbol{\eta}^{(n)}(y) = \begin{pmatrix} \mathrm{i}\omega W_2^{(n)}(y) \\ F^{(n)}(y) \end{pmatrix}, \tag{2.42}$$

where $F^{(n)}(y) = c_{44}(y)\left[W_2^{(n)}(y)\right]'$. The remaining boundary condition $(2.36)_3$ demands that

$$F^{(n)}(0) \sim \left[W_2^{(n)}(y)\right]'_{y=0} = 0 \tag{2.43}$$

for any n. Thus, it can be observed that Eq. (2.41) with the boundary condition (2.43) and the radiation condition at $y \to \infty$ is identical to the problem of surface waves in an inhomogeneous halfspace $y \geq 0$, except that a continuous spectral parameter $k_x \equiv k$ is replaced by a discrete $k_x^{(n)}$, which is given by (2.40). Numerical illustrations for the SH waves in a periodically inhomogeneous strip are presented in the Chapter 5.

2.7 Conclusion

This chapter has dealt with the SH wave propagation in 1D-periodic structures. For this purpose, the matricant and its evaluation through the Peano series was introduced. The Floquet stopbands and passbands were defined via the eigenspectrum of a matricant over the period (the monodromy matrix). This formalism underlies the performed analytical derivations for SH waves in a periodic plate, halfspace and strip.

The main attention has been given to SH surface waves (SHSW) in vertically periodic halfspaces. It was shown that the dispersion branches of a single unit cell with traction-free interfaces split into the ranges corresponding to the 'physical' and 'non-physical' solutions for the SHSW that, respectively, decay or increase at the infinity. A particular spectral selectivity phenomenon was demonstrated for the SHSW in a periodic halfspace with a monotonic profile of material properties over a period. For this case, it was found that the SHSW exist within only a single velocity window and do not exist elsewhere or vice versa. The case of a bilayered unit cell have been investigated in detail. The results were extended to the case of continuously inhomogeneous monotonic unit cell. It was also shown that the same

considerations are valid for the SH waves in a periodic stip, except that the dispersion spectra become discretized.

References

1. M.C. Pease III, Method of Matrix Algebra, New York, London, 1965.

2. A.L. Shuvalov, O. Poncelet, A.N. Podlipenets, On the guided and surface shear horizontal waves in monoclinic transversely periodic layers and halfspace with arbitrary variation of material peroperties across the unit cell, Stud. Geophys. Geod. 50 (2006) 381-398.

3. A.N. Podlipenets, Surface Love Wave in Orthotropic Regularly Layered Composites, Mech. Comp. Matter. 18 (1982) 734-737.

4. R.E. Camley, B. Djafari-Rouhani, L. Dobrzynski, A.A. Maradudin, Transverse Elastic Waves in Periodically Layered Infinite and Semi-infinite Media, Phys. Rev. B 27 (1983) 7318-7329.

5. E.H. El Boudouti, B. Djafari-Rouhani, A. Akjouji, L. Dobrzynski, Theory of Surface and Interface Elastic Waves in N-layer Superlattices, Phys. Rev. B 54 (1996) 14728-14741.

6. N.A. Shul'ga, Propagation of Elastic Waves in Periodically Inhomogeneous Media, Int. Appl. Mech. 39 (2003) 763-796.

7. P. Gatignol, C. Potel, J.F.d. Belleval, Two families of modal waves for periodic structures with two field function: a Cayleigh-Hamilton approach, Acustica-Acta Acustica 96(6) (2007) 959-975.

8. A.L. Shuvalov, O. Poncelet, A.P. Kiselev, Shear horizontal waves in transversely inhomogeneous plates, Wave Motion 45 (2008) 605-615.

9. B.L.N. Kennett, Seismic Wave Propagation in Stratified Media, Cambridge, 1983.

10. K. Aki, P.G. Richards, Quantitative seismology, W. H. Freeman and Company, San Francisco, 1980.

11. M. Born, E. Wolf, Principles of Optics: Electromagnetic Theory of Propagation, Interference, and Diffraction of Light, 6th edition ed., Pergamon Press, New York, 1980.

12. A.L. Shuvalov, O. Poncelet, S.V. Golkin, Existence and spectral properties of shear horizontal surface acoustic waves in vertically periodic half-spaces, Proc. R. Soc. Lond. A 465 (2009) 1489-1511.

3 Finite Difference Time Domain Method (FDTD) for elastic waves

Table of contents

3.1 Introduction

Numerical simulations of elastic wave propagation performed in the thesis are based on the Finite Difference Time Domain (FDTD) method. This method has been broadly applied in various fields such as electromagnetics, geophysics and aero- or marine-acoustics applications. First proposed by Yee [1] in 1966 as a powerful calculation method for electromagnetic waves, it was later transferred to elastodynamics. We will implement finite difference on Cartesian 2D-grids with completely staggered grids [2]. It means that the field components (velocity and stress) are distributed between different nodes position.

The FDTD method implies that the coupled partial differential equations, which describe the wave propagation in elastic media, are directly discretized in time and space by using central differences numerical scheme. The staggered-grid FDTD scheme of the second-order accuracy in time and space, which is developed on the basis of a simple Taylor expansion, is both straightforward and provides a reasonable accuracy. Its practical implementation, coupled with an intelligent object-oriented coding, ensures a running-code efficiency and allows extensional-code features for further advanced applications (more complicated constitutive laws, multiphysics, etc.)

The present chapter demonstrates the FDTD schemes for SH and P/SV waves and the treatment of boundary conditions within these schemes which may involve discontinuities, sources, internal and external boundaries. We will also explain the concept and construction of a PML (Perfectly Matched Layer) which surrounds the computational domain and absorbs the outward travelling waves. We employ the PMLs for modelling the wave propagation at infinity.

3.2 Finite difference definition. Finite difference order. Types of finite differences

The *finite difference* of the first order of the function $f(x)$ is

$$\Delta f(x) = f(x+d) - f(x), \tag{3.1}$$

where d is a positive constant. The finite difference of the second order is

$$\Delta^2 f(x) = \Delta[\Delta f(x)] = \Delta f(x+d) - \Delta f(x) = f(x+2d) - 2f(x+d) + f(x). \tag{3.2}$$

Continuing this process leads to the differences of higher order $\Delta^3 f(x)$, $\Delta^4 f(x)$, etc. One can consider a finite difference as the discrete analogue of a derivative. A forward difference is an expression of the form

$$\Delta f(x) = f(x+d) - f(x). \tag{3.3}$$

Depending on the application, the spacing d is kept constant, or the limit $d \to 0$ is taken. A backward difference (denoted ∇f) arises when the point neighbouring to x is less than x,

$$\nabla f(x) = f(x) - f(x-d). \tag{3.4}$$

Finally, *the central difference* is the average of the forward and backward differences. It is given by

$$\delta f(x) = \frac{\Delta f(x) + \nabla f(x)}{2} = \frac{f(x+d) - f(x-d)}{2}. \tag{3.5}$$

Let us obtain the finite difference in the form that will be used in this thesis. Consider the forward and backward Taylor expansions of a function $f(x)$ about the point x,

$$f(x+d) = f(x) + df'(x) + \frac{1}{2}d^2 f''(x) + O(d^3), \tag{3.6}$$

$$f(x-d) = f(x) - df'(x) + \frac{1}{2}d^2 f''(x) + O(d^3). \tag{3.7}$$

Subtracting (3.7) from (3.6) allows eliminating the second order derivative of f, which leads to

$$f(x+d) - f(x-d) = 2f'(x)d + O(d^3). \tag{3.8}$$

It follows that

$$f'(x) = \frac{f(x+d) - f(x-d)}{2d} + O(d^2), \tag{3.9}$$

which estimates the derivative of a function with an error of the second order with respect to the small parameter d. Taking small enough values of d, a simple formula (3.9) is largely sufficient for practical use in the numerical simulations of this thesis.

3.3 2D-FDTD scheme definition and principles. Translating elastodynamics equations to FDTD scheme. SH waves. P/SV waves

3.3.1 Discretization of the data

All the functions related to the wave field are sampled spatially over a 2D uniform grid (rectangular mesh) and sampled over a uniform sequence of values of time (constant time steps). Therefore the sampled data are expressed in index notations

$$f_{i,j}^{n} = f\left(x_i, y_j, t_n\right), \tag{3.10}$$

in which the discretized spatial coordinates x_i, y_j and the discrete values of time t_n are defined as follows:

$$x_i = x_0 + i\Delta x, \quad y_j = y_0 + j\Delta y, \quad t_n = t_0 + n\Delta t, \tag{3.11}$$

where x_0, y_0 and t_0 are arbitrary origins, and Δx, Δy and Δt are the sampling steps over the variables x, y and t, respectively. Note that the range for indices i and j is completely arbitrary, and that the time-index is commonly chosen as positive along with $t_0 = 0$.
Therefore, for 2D simulations, the discretized transient wave field is a table with three entries. As we will see later, there is no need in practice to store the complete scene of simulation into the RAM. To make the scheme running, the full wave field just has to be known at two consecutive instants of time.

3.3.2 Leap-frog numerical scheme

The elastic-wave propagation is governed by the equation of motion and Hook's law. The system of elastodynamics equations (1.19) may be written in the form

$$\begin{cases} \rho\partial_t \mathbf{v} = \operatorname{div}\boldsymbol{\sigma} + \mathbf{f}, \\ \partial_t \boldsymbol{\sigma} = \mathbf{c} : (\dot{\boldsymbol{\varepsilon}} - \mathbf{h}), \end{cases} \tag{3.12}$$

where $\mathbf{f}$ is the density of external force per unit volume, $\mathbf{c}$ the fourth-rank stiffness tensor, $\dot{\boldsymbol{\varepsilon}} = \frac{1}{2}\left(\nabla\mathbf{v} + \nabla^{\mathrm{T}}\mathbf{v}\right)$ the tensor of strain rate and $\mathbf{h}$ the second-rank tensor of strain-rate source. The material is assumed stationary, i.e. the mass density and the elastic constants do not depend on time.

Taking note that (3.12) is satisfied at any instant of time and at any point in space, we can specialize Eq. $(3.12)_1$ at a time $t = t_n$ and at a point $(x, y) = \left(x_i, y_j\right)$ to the form

$$\left(\rho\partial_t \mathbf{v}\right)\Big|_{\substack{t=t_n\\x=x_i\\y=y_j}} = \left(\operatorname{div}\boldsymbol{\sigma}\right)\Big|_{\substack{t=t_n\\x=x_i\\y=y_j}} + \mathbf{f}\Big|_{\substack{t=t_n\\x=x_i\\y=y_j}}. \tag{3.13}$$

Since the mass density is independent of time ($\rho = \rho_{i,j}$), the evaluation of $\partial_t \mathbf{v}$ by the central difference formula about $t = t_n$ leads to

$$\left(\partial_t \mathbf{v}\right)\Big|_{\substack{t=t_n\\x=x_i\\y=y_j}} = \frac{\mathbf{v}_{i,j}^{n+\frac{1}{2}} - \mathbf{v}_{i,j}^{n-\frac{1}{2}}}{\Delta t} + O\left(\left(\Delta t\right)^2\right). \tag{3.14}$$

Note that evaluating the derivative of a function at a point by the central difference involves the values of the function at the points symmetrical about the point of interest but not at this point itself. That is why the temporal indices $n+\frac{1}{2}$ and $n-\frac{1}{2}$ appear in the quantities $\mathbf{v}_{i,j}^{n+\frac{1}{2}}$ and $\mathbf{v}_{i,j}^{n-\frac{1}{2}}$ in (3.14), while $\mathbf{v}_{i,j}^{n}$ does not have to be known for evaluating $\left(\partial_t \mathbf{v}\right)_{i,j}^{n}$. As regards the (stationary) mass density, it must be known at the same points than the velocity fields.

Consider next the term $\operatorname{div}\boldsymbol{\sigma}$ on the right-hand side of (3.13). It involves only the spatial partial derivatives over each coordinate. Therefore the stress field must be evaluated at time $t = t_n$, while the points, at which it must be known, are taken to be symmetrical about the point $\left(x_i, y_j\right)$ – for the same reasons as when using the central difference in time, see (3.14). Thus the approximations of variations of the stress tensor $\boldsymbol{\sigma}$ in x and y are given by:

$$\begin{aligned}
\left(\partial_x \boldsymbol{\sigma}\right)\Big|_{\substack{t=t_n\\x=x_i\\y=y_j}} &= \frac{\boldsymbol{\sigma}_{i+\frac{1}{2},j}^{n} - \boldsymbol{\sigma}_{i-\frac{1}{2},j}^{n}}{\Delta x} + O\left(\left(\Delta x\right)^2\right),\\
\left(\partial_y \boldsymbol{\sigma}\right)\Big|_{\substack{t=t_n\\x=x_i\\y=y_j}} &= \frac{\boldsymbol{\sigma}_{i,j+\frac{1}{2}}^{n} - \boldsymbol{\sigma}_{i,j-\frac{1}{2}}^{n}}{\Delta y} + O\left(\left(\Delta y\right)^2\right).
\end{aligned} \tag{3.15}$$

It is clear now that the first equation of (3.12) may be discretized with the central difference numerical scheme by considering a staggered-grid in space and time for the sampled transient wave-field data. The discrete stress field $\boldsymbol{\sigma}$ is probed over a space-time grid that is shifted by $\Delta t/2$ in time and by $\Delta x/2$ and $\Delta y/2$ in space with respect to the velocity-field grid. Applying a similar reasoning to the second equation of (3.12) leads to a similar staggered-grid scheme for discretizing the stress-strain law.

In view of Eq. (3.12), we conclude that the mass density ρ and the source of force $\mathbf{f}$ must be evaluated (or be known a priori) over the spatial grid of $\mathbf{v}$ and the time grid of $\boldsymbol{\sigma}$, while the stiffness constants $\mathbf{c}$ and the source of strain rate $\mathbf{h}$ must be sampled spatially over the grid of $\boldsymbol{\sigma}$ and temporally over the grid of $\mathbf{v}$. The relative spatial positions of each component v_i of $\mathbf{v}$ and σ_{ij} of $\boldsymbol{\sigma}$ must be in accordance with application of the central

difference scheme. This scheme is known as the Yee FDTD scheme [1] introduced first for the transient electrodynamics, or the Virieux FDTD scheme [2] for the elastodynamics. When defining the distribution of the sampled data over a unit cell, it is advisable to keep in mind as to where the boundaries and interfaces are supposed to appear within the mesh. For instance, if a portion of a possible surface of discontinuity of the material properties coincides with one face of a cell, using the component(s) of the wave field that are physically continuous along the normal to the interface enables a more straightforward treatment of the boundary or jump conditions. In the present work, the choice of a cell for the SH and P/SV waves is made with regard for this aspect, as detailed in Section 3.4.

3.3.3 Scheme for the case of SH waves

Let us develop the explicit equations for SH waves in the FDTD form. We proceed from Equation (3.12) for the case of an orthorhombic material,

$$\begin{cases} \rho \partial_t v_3 = \partial_x \sigma_5 + \partial_y \sigma_4 + f_3, \\ \partial_t \sigma_5 = c_{55}(\partial_x v_3 - h_5), \\ \partial_t \sigma_4 = c_{44}(\partial_y v_3 - h_4). \end{cases} \tag{3.16}$$

Combining it into the finite difference form by applying the central finite difference formula (3.9) yields:

$$\begin{cases} \rho^n_{i+\frac{1}{2},j+\frac{1}{2}} \dfrac{\left(v_3\right)^{n+\frac{1}{2}}_{i+\frac{1}{2},j+\frac{1}{2}} - \left(v_3\right)^{n-\frac{1}{2}}_{i+\frac{1}{2},j+\frac{1}{2}}}{\Delta t} = \dfrac{\left(\sigma_5\right)^{n}_{i+1,j+\frac{1}{2}} - \left(\sigma_5\right)^{n}_{i,j+\frac{1}{2}}}{\Delta x} + \dfrac{\left(\sigma_4\right)^{n}_{i+\frac{1}{2},j+1} - \left(\sigma_4\right)^{n}_{i+\frac{1}{2},j}}{\Delta y} + \left(f_3\right)^{n}_{i+\frac{1}{2},j+\frac{1}{2}}, \\ \dfrac{\left(\sigma_5\right)^{n+1}_{i,j+\frac{1}{2}} - \left(\sigma_5\right)^{n}_{i,j+\frac{1}{2}}}{\Delta t} = \left(c_{55}\right)^{n+\frac{1}{2}}_{i,j+\frac{1}{2}} \left(\dfrac{\left(v_3\right)^{n+\frac{1}{2}}_{i+\frac{1}{2},j+\frac{1}{2}} - \left(v_3\right)^{n+\frac{1}{2}}_{i-\frac{1}{2},j+\frac{1}{2}}}{\Delta x} - \left(h_5\right)^{n+\frac{1}{2}}_{i,j+\frac{1}{2}} \right), \\ \dfrac{\left(\sigma_4\right)^{n+1}_{i+\frac{1}{2},j} - \left(\sigma_4\right)^{n}_{i+\frac{1}{2},j}}{\Delta t} = \left(c_{44}\right)^{n+\frac{1}{2}}_{i+\frac{1}{2},j} \left(\dfrac{\left(v_3\right)^{n+\frac{1}{2}}_{i+\frac{1}{2},j+\frac{1}{2}} - \left(v_3\right)^{n+\frac{1}{2}}_{i+\frac{1}{2},j-\frac{1}{2}}}{\Delta y} - \left(h_4\right)^{n+\frac{1}{2}}_{i+\frac{1}{2},j} \right). \end{cases} \tag{3.17}$$

We will refer to the cell with no boundary or jump conditions at its aggregate boundary as a *Bulk Cell*. The system (3.17) is written for the case of a *Bulk Cell*. The distribution of the three non-zero components of the SH wave field within the elementary cell is shown in Fig. 3.1.

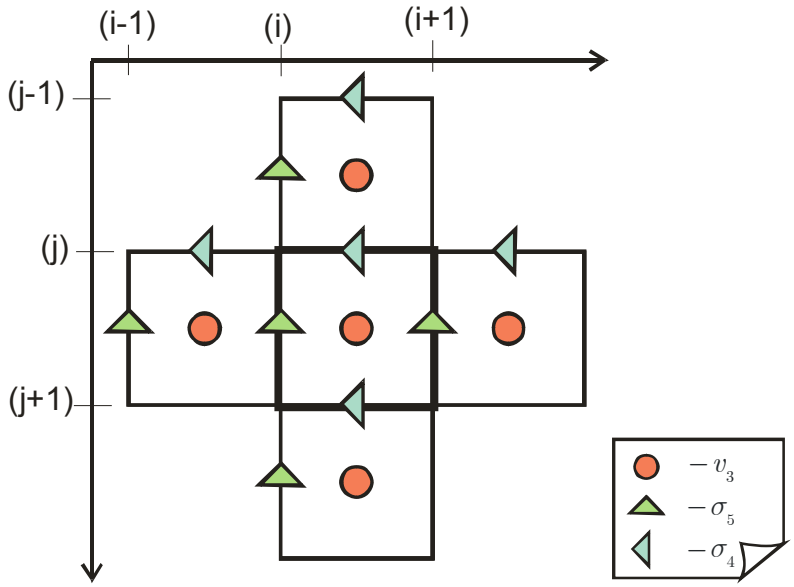

Fig. 3.1 *The distribution of the SH wave field components within the Bulk FDTD Cell*

Arranging the discretization mesh on the computational domain gives the characteristic staggered finite-difference grid. Figure 3.1 shows the position of the field components in the finite difference grid. In this grid, the velocity and stress field components are not defined at the same position in time and in space. They are taken with an offset by $\Delta t/2$ in time and by $\Delta x/2$ and $\Delta y/2$ in space. Rearranging (3.17) gives the expression of the explicit scheme (time integration) for getting updated values of the wave field:

$$\begin{cases} \left(v_3\right)_{i+\frac{1}{2},j+\frac{1}{2}}^{n+\frac{1}{2}} = \left(v_3\right)_{i+\frac{1}{2},j+\frac{1}{2}}^{n-\frac{1}{2}} + \dfrac{\Delta t}{\rho_{i+\frac{1}{2},j+\frac{1}{2}}^{n}} \left(\dfrac{\left(\sigma_5\right)_{i+1,j+\frac{1}{2}}^{n} - \left(\sigma_5\right)_{i,j+\frac{1}{2}}^{n}}{\Delta x} + \dfrac{\left(\sigma_4\right)_{i+\frac{1}{2},j+1}^{n} - \left(\sigma_4\right)_{i+\frac{1}{2},j}^{n}}{\Delta y} + \left(f_3\right)_{i+\frac{1}{2},j+\frac{1}{2}}^{n} \right), \\ \left(\sigma_5\right)_{i,j+\frac{1}{2}}^{n+1} = \left(\sigma_5\right)_{i,j+\frac{1}{2}}^{n} + \Delta t \left(c_{55}\right)_{i,j+\frac{1}{2}}^{n+\frac{1}{2}} \left(\dfrac{\left(v_3\right)_{i+\frac{1}{2},j+\frac{1}{2}}^{n+\frac{1}{2}} - \left(v_3\right)_{i-\frac{1}{2},j+\frac{1}{2}}^{n+\frac{1}{2}}}{\Delta x} - \left(h_5\right)_{i,j+\frac{1}{2}}^{n+\frac{1}{2}} \right), \\ \left(\sigma_4\right)_{i+\frac{1}{2},j}^{n+1} = \left(\sigma_4\right)_{i+\frac{1}{2},j}^{n} + \Delta t \left(c_{44}\right)_{i+\frac{1}{2},j}^{n+\frac{1}{2}} \left(\dfrac{\left(v_3\right)_{i+\frac{1}{2},j+\frac{1}{2}}^{n+\frac{1}{2}} - \left(v_3\right)_{i+\frac{1}{2},j-\frac{1}{2}}^{n+\frac{1}{2}}}{\Delta y} - \left(h_4\right)_{i+\frac{1}{2},j}^{n+\frac{1}{2}} \right). \end{cases} \tag{3.18}$$

The offset in time leads to the so-called leap-frog scheme, wherein the field components are updated sequentially in time. Assuming that the whole wave field at time moments $t_{n-\frac{1}{2}}$ and t_n is known, we calculate every v_3 at time $t_{n+\frac{1}{2}}$ through Eq. $(3.17)_1$; then we calculate the stress components σ_4 and σ_5 at the time t_{n+1} using the velocity components calculated above for $t_{n+\frac{1}{2}}$; then we again calculate the velocity components using the previously calculated stress components, and so on. Thus, knowing the velocity and stress field components

throughout the entire computational domain at the time $t_0 - 0.5\Delta t$ and t_0, respectively, the field components can be calculated for all subsequent steps $t > t_0$.

3.3.4 Scheme for the case of P/SV waves

Consider the two-dimensional case of the P and SV waves propagating in the plane (x, y). Eq. (3.12) reduces now to the form

$$\begin{cases} \rho\partial_t v_1 = \partial_1\sigma_1 + \partial_2\sigma_6 + f_1, \\ \rho\partial_t v_2 = \partial_1\sigma_6 + \partial_2\sigma_2 + f_2, \\ \partial_t\sigma_1 = c_{11}(\partial_1 v_1 - h_1) + c_{12}(\partial_2 v_2 - h_2), \\ \partial_t\sigma_2 = c_{12}(\partial_1 v_1 - h_1) + c_{22}(\partial_2 v_2 - h_2), \\ \partial_t\sigma_6 = c_{66}(\partial_1 v_2 + \partial_2 v_1 - h_6). \end{cases} \tag{3.19}$$

Similarly to the above case of SH waves, the sampled data of the wave field may be chosen in such a way that only central differences appear in the numerical scheme. Fig. 3.2 shows the locations, at which the components of the wave field are probed. The normal-stress components σ_1 and σ_2 are both shifted over the two spatial indices and are evaluated at each integer value of the time index. The components v_1 and v_2 are probed at the vertical and horizontal faces of the cell, respectively, while the stress σ_6 is taken at the corners. Such a choice enables dealing with those components of the wave field that are continuous across the cell boundaries. This is going to be useful when the physical interfaces are to be considered.

Thus the explicit staggered scheme for P/SV waves in a cell within the bulk is given by the following system of equations:

$$
\begin{cases}
\left(v_1\right)_{i,j+\frac{1}{2}}^{n+\frac{1}{2}} = \left(v_1\right)_{i,j+\frac{1}{2}}^{n-\frac{1}{2}} + \dfrac{\Delta t}{\rho_{i,j+\frac{1}{2}}}\left(\dfrac{\left(\sigma_1\right)_{i+\frac{1}{2},j+\frac{1}{2}}^{n} - \left(\sigma_1\right)_{i-\frac{1}{2},j+\frac{1}{2}}^{n}}{\Delta x} + \dfrac{\left(\sigma_6\right)_{i,j+1}^{n} - \left(\sigma_6\right)_{i,j}^{n}}{\Delta y} + \left(f_1\right)_{i,j+\frac{1}{2}}^{n}\right), \\
\left(v_2\right)_{i+\frac{1}{2},j}^{n+\frac{1}{2}} = \left(v_2\right)_{i+\frac{1}{2},j}^{n-\frac{1}{2}} + \dfrac{\Delta t}{\rho_{i+\frac{1}{2},j}}\left(\dfrac{\left(\sigma_6\right)_{i+1,j}^{n} - \left(\sigma_6\right)_{i,j}^{n}}{\Delta x} + \dfrac{\left(\sigma_2\right)_{i+\frac{1}{2},j+\frac{1}{2}}^{n} - \left(\sigma_2\right)_{i+\frac{1}{2},j-\frac{1}{2}}^{n}}{\Delta y} + \left(f_2\right)_{i+\frac{1}{2},j}^{n}\right), \\
\left(\sigma_1\right)_{i+\frac{1}{2},j+\frac{1}{2}}^{n+1} = \left(\sigma_1\right)_{i+\frac{1}{2},j+\frac{1}{2}}^{n} + \Delta t\left(c_{11}\right)_{i+\frac{1}{2},j+\frac{1}{2}}\left(\dfrac{\left(v_1\right)_{i+1,j+\frac{1}{2}}^{n+\frac{1}{2}} - \left(v_1\right)_{i,j+\frac{1}{2}}^{n+\frac{1}{2}}}{\Delta x} - \left(h_1\right)_{i+\frac{1}{2},j+\frac{1}{2}}^{n+\frac{1}{2}}\right) + \\
\qquad + \Delta t\left(c_{12}\right)_{i+\frac{1}{2},j+\frac{1}{2}}\left(\dfrac{\left(v_2\right)_{i+\frac{1}{2},j+1}^{n+\frac{1}{2}} - \left(v_2\right)_{i+\frac{1}{2},j}^{n+\frac{1}{2}}}{\Delta y} - \left(h_2\right)_{i+\frac{1}{2},j+\frac{1}{2}}^{n+\frac{1}{2}}\right), \\
\left(\sigma_2\right)_{i+\frac{1}{2},j+\frac{1}{2}}^{n+1} = \left(\sigma_2\right)_{i+\frac{1}{2},j+\frac{1}{2}}^{n} + \Delta t\left(c_{12}\right)_{i+\frac{1}{2},j+\frac{1}{2}}\left(\dfrac{\left(v_1\right)_{i+1,j+\frac{1}{2}}^{n+\frac{1}{2}} - \left(v_1\right)_{i,j+\frac{1}{2}}^{n+\frac{1}{2}}}{\Delta x} - \left(h_1\right)_{i+\frac{1}{2},j+\frac{1}{2}}^{n+\frac{1}{2}}\right) + \\
\qquad + \Delta t\left(c_{22}\right)_{i+\frac{1}{2},j+\frac{1}{2}}\left(\dfrac{\left(v_2\right)_{i+\frac{1}{2},j+1}^{n+\frac{1}{2}} - \left(v_2\right)_{i+\frac{1}{2},j}^{n+\frac{1}{2}}}{\Delta y} - \left(h_2\right)_{i+\frac{1}{2},j+\frac{1}{2}}^{n+\frac{1}{2}}\right), \\
\left(\sigma_6\right)_{i,j}^{n+1} = \left(\sigma_6\right)_{i,j}^{n} + \Delta t\left(c_{66}\right)_{i,j}\left(\dfrac{\left(v_2\right)_{i+\frac{1}{2},j}^{n+\frac{1}{2}} - \left(v_2\right)_{i-\frac{1}{2},j}^{n+\frac{1}{2}}}{\Delta x} + \dfrac{\left(v_1\right)_{i,j+\frac{1}{2}}^{n+\frac{1}{2}} - \left(v_1\right)_{i,j-\frac{1}{2}}^{n+\frac{1}{2}}}{\Delta y} - \left(h_6\right)_{i,j}^{n+\frac{1}{2}}\right).
\end{cases}
\tag{3.20}
$$

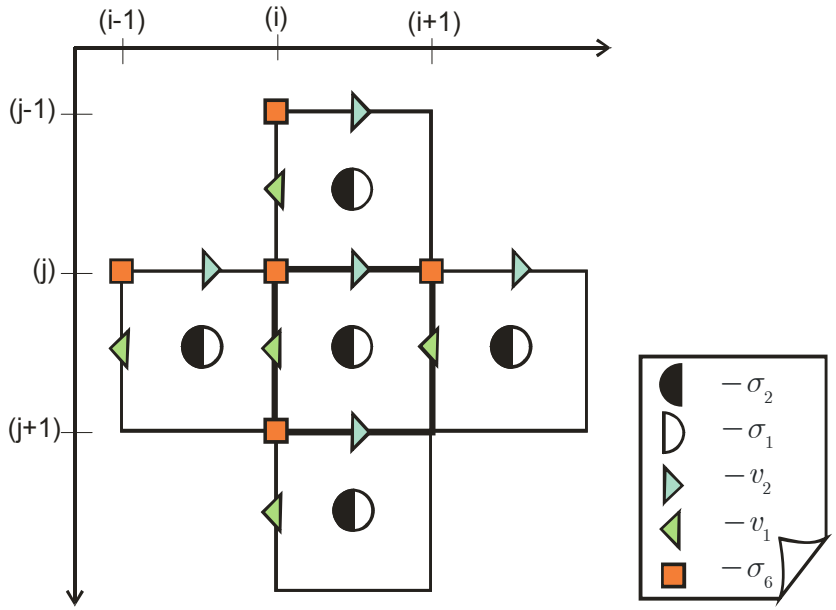

Fig. 3.2 *Example of the Bulk FD cell for the P/SV waves.*

3.4 Treatment of boundary conditions by FDTD scheme

The use of the schemes (3.18) and (3.20) is subject to certain conditions on the discretization parameters Δx, Δy and Δt to ensure stability and low dispersion of the numerical schemes. These aspects are discussed in Chapter 4 and mainly concern the propagation of waves in the bulk of the materials. Before that, we consider another important aspect of the numerical discretization of the wave problems in inhomogeneous media, namely, the issue of modelling of the boundary conditions.

Treatment of the boundary conditions (BC) within the finite difference scheme needs a special care. We consider the following types of BC: external boundary (conditions at the grid edges); discontinuity within the computational domain (infinitely narrow cracks, cavities); contact source (imposing stress or velocity field at a surface) and internal boundary (interfaces separating materials with different physical properties). All these physical BC amount to the following numerical conditions:

- *Free or forced traction conditions;*
- *Sliding contact conditions;*
- *Continuity conditions at rigid interfaces in between different solid materials;*
- *Conditions of no reflection at external boundaries (PML).*

Implementation of these conditions is discussed in the following sections for the case of SH waves, while the case of P/SV waves is detailed in **Appendix A** .

3.4.1 FDTD cell types for SH waves

For the case of SH waves (see Fig. 3.1) the *free* or *forced traction condition* imposes, respectively, zero or non-zero stress at the cell face where this condition applies. The velocity field component v_3 is calculated as in the bulk of a medium (with no concern for a possible presence of an interface in the neighbourhood), because it has to be known only at the centre of the cell while its knowledge at the cell edges is not needed. In practice, the application of BC, such as a free surface or a contact force, on either the top or the left face of the cell is rather straightforward. Instead of computing Eqs. (3.18) for the stress σ_4 and/or σ_5, these stresses are directly set to zero for the free-surface BC, or equated to the imposed value corresponding to the transient surface-source term. For example, assume that the top surface

of the cell is free (Fig. 3.3). Then the components v_3 and σ_5 are updated according to (3.18), while σ_4 is set to a given value $(s_4)^n_{i+\frac{1}{2},j}$ according to the boundary condition:

$$(s_4)^n_{i+\frac{1}{2},j} = \begin{cases} 0 \quad \text{for traction-free BC,} \\ s_4(x_{i+\frac{1}{2}}, y_j, t_n) \quad \text{for the source BC.} \end{cases} \tag{3.21}$$

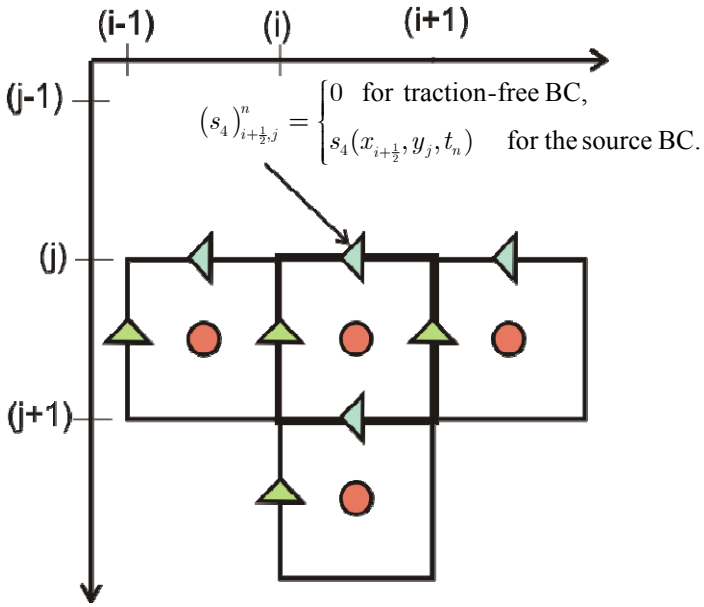

Fig. 3.3 *Free Top BC cell for the SH-wave case*

Let us now analyze the less evident case of right and/or bottom free surface(s) of the cell. As an example, consider in the following a cell that is situated at the corner formed by two perpendicular free surfaces (Fig. 3.4). In order to update the velocity value v_3 at the cell centre, the values of σ_4 and σ_5 are required at the bottom and right boundaries of the cell, respectively. These values are normally supposed to belong to the cells adjacent to the given one on the right and from below; however, such cells do not exist around a corner cell in hand. For this case, additional values for σ_4 and σ_5 are used in the mesh which are specified according to the boundary conditions. The value v_3 can therefore be updated in a standard way using (3.18).

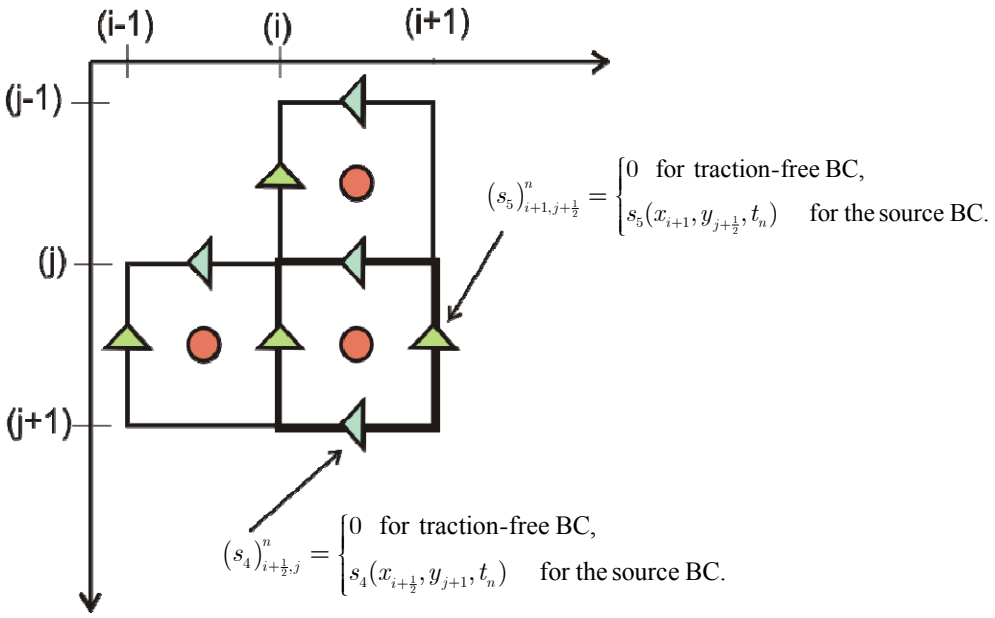

Fig. 3.4 *Right and Bottom Free cell for the SH wave case*

For the case of SH waves, the *sliding contact condition* is identical to the *free-traction condition* and is therefore handled in exactly the same way. Treatment of the sliding contact and of all the other types of BC for the case of P/SV waves is discussed in **Appendix A** .

We have implemented the described FDTD scheme by using object-oriented programming (C++) with multiple derivation classes. A hierarchy of C++ classes was created in close connection with the type of cells, which depends on the possible presence of BC and on the position where the BC is applied. The central class “Bulk Cell” with no BC at its aggregate boundary and the other eight classes derived from the “Bulk Cell” class are presented in Fig. 3.5.

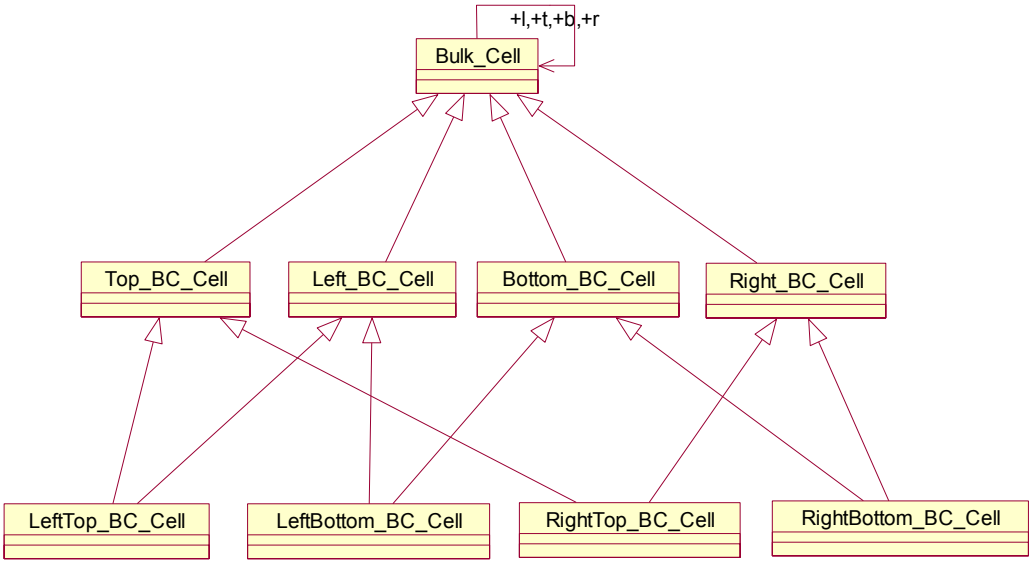

Fig. 3.5 *Object Class diagram for BC treatment using UML (Unified Modelling Language) notations*

3.4.2 Treatment of a discontinuity in FDTD scheme (crack model)

Having introduced all types of computational cells for different kinds of BC, we exemplify here the crack (or slit) modelling in the FDTD-code implementation. We consider a flat crack as a discontinuity within the bulk and assume that this rupture is located along the regular mesh, see Fig. 3.6. The latter restriction implies that only the cracks with either horizontal or vertical orientations will be treated. In this framework, a crack is modelled by the internal free BC applied to the adjacent cells and entailing their disconnection across the slit. For this model, the scheme (3.18) does not have to be modified, since all the components of the acoustic field can be calculated likewise the case of a continuous medium. The only difference is that certain stress components (σ_4 for horizontal cracks and σ_5 for vertical cracks) are taken to be zero along the crack.

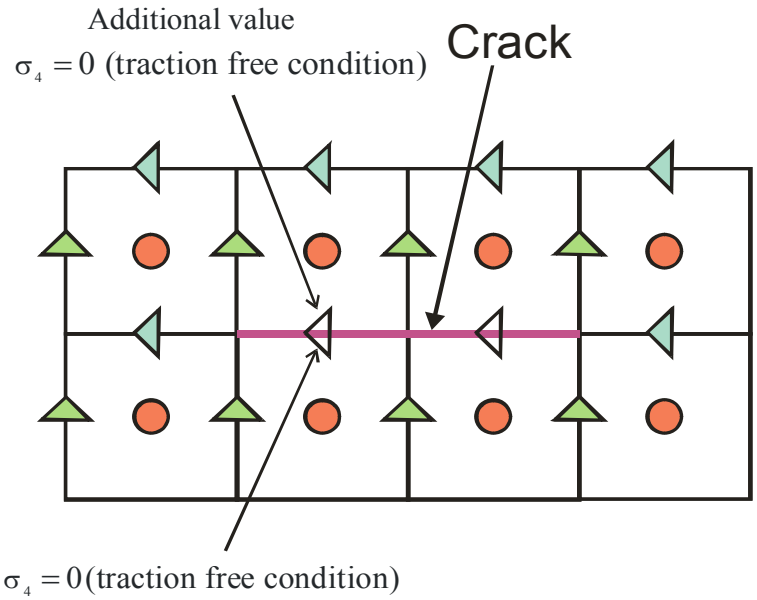

Fig. 3.6 *Crack model*

3.4.3 Rigid contact of two materials

A loose approach allows one to use an intact system (3.18) for updating the wave-field components that are continuous across the rigid-contact interface (σ_4 for horizontal and σ_5 for vertical boundaries). Note, however, that the two last equations in (3.18), which update the stress, evaluate the derivative of the velocity v_3 by means of a central difference and that in turn requires continuous differentiability of v_3 across the rigid-contact interface. We know that the latter is not the case: in fact, the normal gradient of v_3 has a jump despite that v_3 is

continuous across the interface. A possible course of action, which minimizes the error of using Eq. (3.18) for the case of rigid contact, is to replace the central difference evaluation of the normal gradient of v_3 at the interface by its averaged evaluation. As a result, the central difference is split into backward and forward finite differences that lead to a modified central difference scheme with averaged material parameters. It is noted that this modified scheme anyway loses an order of accuracy in the neighbourhood of the interface: the committed error is now of the order of 1 in Δx or Δy and is proportional to the jump of material properties.

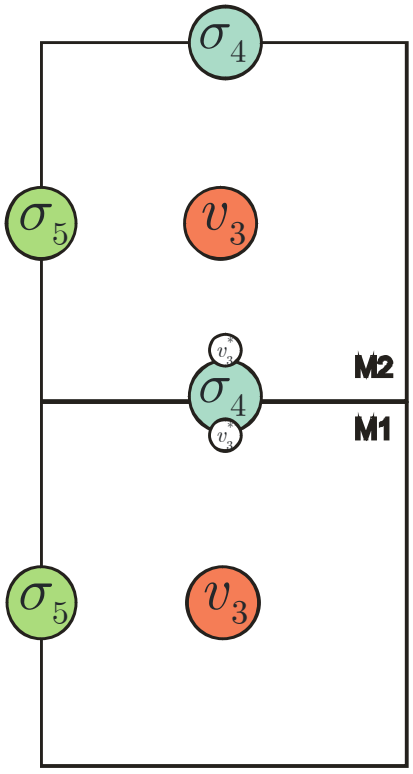

Fig. 3.7 *Two cells of different materials separated by a horizontal rigid interface*

To exemplify this feature, let us consider a horizontal rigid interface between two media (Fig. 3.7). Calculating the wave field for the upper cell does not pose any problem, since no data needs to be updated at the boundary and so the scheme (3.18) can be used as it is. For the same reason, (3.18) can also be utilized for updating v_3 and σ_5 of the lower cell,. The difficulty arises for the update of σ_4 in the lower cell, since v_3 is not differentiable at the interface. In this regard, taking advantage of the continuity of v_3, the interface value of the velocity field v_3^*, which does not belong to the set of discretized data in the mesh, is introduced for the moment. Then the value of σ_4 can be updated by using a unilateral finite difference of the first order. This can be performed either in the upper medium (calculation of $\sigma_4^{(1)}$) or in the lower one (calculation of $\sigma_4^{(2)}$):

$$\frac{\partial_t \sigma_4^{(1)}}{c_{44}^{(1)}} = \frac{v_3^* - v_3^{(1)}}{\Delta y / 2}, \tag{3.22}$$

$$\frac{\partial_t \sigma_4^{(2)}}{c_{44}^{(2)}} = \frac{v_3^{(2)} - v_3^*}{\Delta y / 2}. \tag{3.23}$$

Knowing that $\sigma_4^{(1)} = \sigma_4^{(2)} = \sigma_4$, we take the sum of the two last expressions to obtain

$$\partial_t \sigma_4 = \frac{2c_{44}^{(1)} c_{44}^{(2)}}{c_{44}^{(2)} + c_{44}^{(1)}} \left(\frac{v_3^{(1)} - v_3^{(2)}}{\Delta y} \right), \tag{3.24}$$

where the unknown auxiliary v_3^* has now disappeared. The finite difference scheme for σ_4 finally takes the same form as in (3.18):

$$\left(\sigma_4\right)_{i+\frac{1}{2},j}^{n+1} = \left(\sigma_4\right)_{i+\frac{1}{2},j}^{n} + \Delta t \frac{2c_{44}^{(1)} c_{44}^{(2)}}{c_{44}^{(2)} + c_{44}^{(1)}} \left(\frac{\left(v_3\right)_{i+\frac{1}{2},j+\frac{1}{2}}^{n+\frac{1}{2}} - \left(v_3\right)_{i+\frac{1}{2},j-\frac{1}{2}}^{n+\frac{1}{2}}}{\Delta y} \right), \tag{3.25}$$

except that the elastic constant c_{44} has been replaced by the harmonic mean of c_{44} averaged over the two media. Following the same procedure now for vertical rigid interface (Fig. 3.8), the value σ_5 at the interface is updated according to

$$\left(\sigma_5\right)_{i,j+\frac{1}{2}}^{n+1} = \left(\sigma_5\right)_{i,j+\frac{1}{2}}^{n} + \Delta t \frac{2c_{55}^{(1)} c_{55}^{(2)}}{c_{55}^{(2)} + c_{55}^{(1)}} \left(\frac{\left(v_3\right)_{i+\frac{1}{2},j+\frac{1}{2}}^{n+\frac{1}{2}} - \left(v_3\right)_{i-\frac{1}{2},j+\frac{1}{2}}^{n+\frac{1}{2}}}{\Delta y} \right). \tag{3.26}$$

In the case of a cell in contact with two other different materials (both on top and on left), the equations (3.25) and (3.26) are used for updating σ_4 and σ_5, respectively.

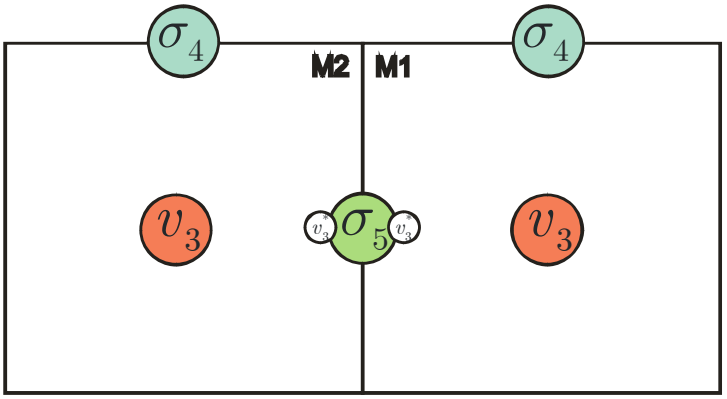

Fig. 3.8 *Two cells of different materials separated by a vertical rigid interface*

3.4.4 Perfectly Matched Layer (PML) conception. Plugging PML into FDTD scheme

Because a numerical mesh is necessarily finite, the simulation of the wave propagation in open domains requires a special treatment at the computational domain boundaries. In order to emulate infinity, all the waves reaching the edges of the mesh must not be reflected at the boundaries. One way to treat this problem accurately is to use a Perfectly Match Layer (PML), first introduced by Berenger in electromagnetics [3] and later adapted to elastodynamics by Chew and Liu [4]. In the essence, PML is a zone that surrounds a discretized finite physical domain and acts as a perfect absorber for the outgoing waves without introducing their spurious reflections at the PML/physical domain interfaces. In other words, the waves departing from the physical domain must disappear in the PML.

Let us present the general principles of the PML model. Consider the left half-space as a part of the physical domain and the right half-space as an artificial layer. Then the objective of the PML can be formulated as follows: *to couple the wave equation in the left half-space with the wave equation in the right half-space so that there is* **no reflection** *at the interface, and so that the wave* **decreases exponentially** *into the depth of the layer.*

To realize this objective, we first express the actual field components (say, v_3) as a sum of two abstract ones (v_3^x and v_3^y),

$$v_3 = v_3^x + v_3^y. \tag{3.27}$$

Taking the superscripts as ^{x} and ^{y} is actually associated with the type of derivatives, which the abstract wave-field component is linked to. For instance, the equation of motion $\rho\partial_t v_3 = \partial_x \sigma_5 + \partial_y \sigma_4$ obviously shows that the variation of v_3 results from both the variation of σ_5 in x ($\partial_x \sigma_5$) and the variation of σ_4 in y ($\partial_y \sigma_4$). The idea is to split the main equation by way of the decomposition (3.27) into a coupled system

$$\begin{cases} \rho\partial_t v_3^x = \partial_x \sigma_5, \\ \rho\partial_t v_3^y = \partial_y \sigma_4. \end{cases} \tag{3.28}$$

The auxiliary components v_3^x and v_3^y defined by (3.27) have of themselves no physical meaning. The role of the above field splitting enabled by v_3^x and v_3^y is to introduce a directional attenuation solely in the components related to the partial derivative taken through the depth of the PML (e.g., the attenuation of v_3^x along x in Eq. $(3.28)_1$).

As the second step, the damping terms are added to the wave equation to provide a directional artificial attenuation of the wave field into the depth of the layer; at the same time, these damping terms must not cause a decrease of the waves along other directions. Therefore the PML must take on the mechanical properties of the last cell of the physical domain for avoiding an impedance mismatch at the entrance of the PML. Another aspect is to define the damping factor in such a way that the attenuation of the waves, which have entered the PML, still maintains no jump of impedance at the interface. This can be achieved by introducing functional damping factors $d^x(x)$ and $d^y(y)$ as continuous functions of space coordinates. They should start with a zero value at the edge of the physical domain (so that there is no damping close the interface) and acquire greater values with growing depth in order to increase the attenuation process. In practice, the surrounding PML is supposed to be not so thick to avoid a large number of computational cells in the mesh. Hence the damping functions must evolve rapidly enough through the depth for providing a sufficient attenuation of the wave field before it reaches the end of the computational domain. At the PML exit boundary, the wave field is reflected backwards and returns to the physical domain; however, its amplitude after a return trip through the PML is much less than at the entrance. The order of magnitude of the spurious reflection depends therefore on:

- the length of the PML in terms of cells;
- the rate of change and the final value of the functional damping factor at the end of the PML.

Rapid increase of the damping factors makes the local damping process more efficient, but at the same time there can be some unwanted spurious reflections due to the strong inhomogeneity of the PML (local reflections). Thus there is a competition between the thickness of PML and the variation of damping factors for achieving a given efficiency. The PML must be thick enough for allowing relatively smooth damping functions and hence for avoiding partial reflections. In our simulations, the PMLs have usually contained from 10 up to 20 additional cells that induced a reflectivity of about 10^{-6}.

Let us now present the PML layout for the continuous elastodynamics problems with respect to the particular case of SH waves. The field splitting as in (3.27) for both velocity and stress field components is given by

$$
\begin{aligned}
v_3 &= v_3^x + v_3^y, \\
\sigma_4 &= \sigma_4^x + \sigma_4^y, \\
\sigma_5 &= \sigma_5^x + \sigma_5^y.
\end{aligned}
\tag{3.29}
$$

Using this decomposition casts Eq. (3.16) with no source terms (which are obviously useless in the PML) in the form of a coupled system

$$
\begin{cases}
\rho\left(\partial_t + d^x(x)\right) v_3^x = \partial_x \sigma_5, \\
\rho\left(\partial_t + d^y(y)\right) v_3^y = \partial_y \sigma_4, \\
\left(\partial_t + d^x(x)\right) \sigma_5^x = c_{55} \partial_x v_3, \\
\left(\partial_t + d^y(y)\right) \sigma_5^y = 0, \\
\left(\partial_t + d^x(x)\right) \sigma_4^x = 0, \\
\left(\partial_t + d^y(y)\right) \sigma_4^y = c_{44} \partial_y v_3.
\end{cases}
\tag{3.30}
$$

In the discretized version of the above system we adopt the same as above conventions for evaluating the finite differences. Considering for the moment only the time discretization, Eq. (3.30) becomes

$$
\begin{cases}
\rho\left[\left(\partial_t + d^x(x)\right) v_3^x\right]^n = \partial_x \sigma_5^n, \\
\rho\left[\left(\partial_t + d^y(y)\right) v_3^y\right]^n = \partial_y \sigma_4, \\
\left[\left(\partial_t + d^x(x)\right) \sigma_5^x\right]^{n+\frac{1}{2}} = c_{55} \partial_x v_3^{n+\frac{1}{2}}, \\
\left[\left(\partial_t + d^y(y)\right) \sigma_5^y\right]^{n+\frac{1}{2}} = 0, \\
\left[\left(\partial_t + d^x(x)\right) \sigma_4^x\right]^{n+\frac{1}{2}} = 0, \\
\left[\left(\partial_t + d^y(y)\right) \sigma_4^y\right]^{n+\frac{1}{2}} = c_{44} \partial_y v_3^{n+\frac{1}{2}}.
\end{cases}
\tag{3.31}
$$

As it has been shown earlier, in the central difference scheme the derivative of v_3 with respect to time at the instant t_n requires knowledge of v_3 at the instants $t_{n+\frac{1}{2}}$ and $t_{n-\frac{1}{2}}$: $\left(\partial_t v_3\right)^n = \left(\left(v_3\right)^{n+\frac{1}{2}} - \left(v_3\right)^{n-\frac{1}{2}}\right) / \Delta t$. Equation (3.31) involves the value $\left(v_3\right)^n$ of v_3 at the instant t_n, but it is not supposed to be known in the leap-frog scheme. To overcome this problem, an estimate of $\left(v_3\right)^n$ via an average of the sampled values $\left(v_3\right)^{n+\frac{1}{2}}$ and $\left(v_3\right)^{n-\frac{1}{2}}$ is used:

$$
\left(v_3\right)^n = \frac{\left(v_3\right)^{n+\frac{1}{2}} + \left(v_3\right)^{n-\frac{1}{2}}}{2}.
\tag{3.32}
$$

Doing the same for the other components of the wave field in (3.31) leads to the discritized system in the form:

$$
\begin{cases}
\rho\left(\dfrac{\left(v_3^x\right)_{i+\frac{1}{2},j+\frac{1}{2}}^{n+\frac{1}{2}}-\left(v_3^x\right)_{i+\frac{1}{2},j+\frac{1}{2}}^{n-\frac{1}{2}}}{\Delta t}+d_{i+\frac{1}{2}}^x\dfrac{\left(v_3^x\right)_{i+\frac{1}{2},j+\frac{1}{2}}^{n+\frac{1}{2}}+\left(v_3^x\right)_{i+\frac{1}{2},j+\frac{1}{2}}^{n-\frac{1}{2}}}{2}\right)=\dfrac{\left(\sigma_5\right)_{i+1,j+\frac{1}{2}}^n-\left(\sigma_5\right)_{i,j+\frac{1}{2}}^n}{\Delta x},\\
\rho\left(\dfrac{\left(v_3^y\right)_{i+\frac{1}{2},j+\frac{1}{2}}^{n+\frac{1}{2}}-\left(v_3^y\right)_{i+\frac{1}{2},j+\frac{1}{2}}^{n-\frac{1}{2}}}{\Delta t}+d_{j+\frac{1}{2}}^y\dfrac{\left(v_3^y\right)_{i+\frac{1}{2},j+\frac{1}{2}}^{n+\frac{1}{2}}+\left(v_3^y\right)_{i+\frac{1}{2},j+\frac{1}{2}}^{n-\frac{1}{2}}}{2}\right)=\dfrac{\left(\sigma_4\right)_{i+\frac{1}{2},j+1}^n-\left(\sigma_4\right)_{i+\frac{1}{2},j}^n}{\Delta y},\\
\dfrac{\left(\sigma_5^x\right)_{i,j+\frac{1}{2}}^{n+1}-\left(\sigma_5^x\right)_{i,j+\frac{1}{2}}^n}{\Delta t}+d_i^x\dfrac{\left(\sigma_5^x\right)_{i,j+\frac{1}{2}}^{n+1}+\left(\sigma_5^x\right)_{i,j+\frac{1}{2}}^n}{2}=c_{55}\dfrac{\left(v_3\right)_{i+\frac{1}{2},j+\frac{1}{2}}^{n+\frac{1}{2}}-\left(v_3\right)_{i-\frac{1}{2},j+\frac{1}{2}}^{n+\frac{1}{2}}}{\Delta x},\\
\dfrac{\left(\sigma_5^y\right)_{i,j+\frac{1}{2}}^{n+1}-\left(\sigma_5^y\right)_{i,j+\frac{1}{2}}^n}{\Delta t}+d_{j+\frac{1}{2}}^y\dfrac{\left(\sigma_5^y\right)_{i,j+\frac{1}{2}}^{n+1}+\left(\sigma_5^y\right)_{i,j+\frac{1}{2}}^n}{2}=0,\\
\dfrac{\left(\sigma_4^x\right)_{i+\frac{1}{2},j}^{n+1}-\left(\sigma_4^x\right)_{i+\frac{1}{2},j}^n}{\Delta t}+d_{i+\frac{1}{2}}^x\dfrac{\left(\sigma_4^x\right)_{i+\frac{1}{2},j}^{n+1}+\left(\sigma_4^x\right)_{i+\frac{1}{2},j}^n}{2}=0,\\
\dfrac{\left(\sigma_4^y\right)_{i+\frac{1}{2},j}^{n+1}-\left(\sigma_4^y\right)_{i+\frac{1}{2},j}^n}{\Delta t}+d_j^y\dfrac{\left(\sigma_4^y\right)_{i+\frac{1}{2},j}^{n+1}+\left(\sigma_4^y\right)_{i+\frac{1}{2},j}^n}{2}=c_{44}\dfrac{\left(v_3\right)_{i+\frac{1}{2},j+\frac{1}{2}}^{n+\frac{1}{2}}-\left(v_3\right)_{i+\frac{1}{2},j-\frac{1}{2}}^{n+\frac{1}{2}}}{\Delta y}.
\end{cases}
\tag{3.33}
$$

Thus the explicit scheme for the PML becomes:

$$
\begin{cases}
\left(v_3^x\right)_{i+\frac{1}{2},j+\frac{1}{2}}^{n+\frac{1}{2}}=\dfrac{1-\frac{1}{2}d_{i+\frac{1}{2}}^x\Delta t}{1+\frac{1}{2}d_{i+\frac{1}{2}}^x\Delta t}\left(v_3^x\right)_{i+\frac{1}{2},j+\frac{1}{2}}^{n-\frac{1}{2}}+\dfrac{\Delta t}{\rho\left(1+\frac{1}{2}d_{i+\frac{1}{2}}^x\Delta t\right)}\dfrac{\left(\sigma_5\right)_{i+1,j+\frac{1}{2}}^n-\left(\sigma_5\right)_{i,j+\frac{1}{2}}^n}{\Delta x},\\
\left(v_3^y\right)_{i+\frac{1}{2},j+\frac{1}{2}}^{n+\frac{1}{2}}=\dfrac{1-\frac{1}{2}d_{j+\frac{1}{2}}^y\Delta t}{1+\frac{1}{2}d_{j+\frac{1}{2}}^y\Delta t}\left(v_3^y\right)_{i+\frac{1}{2},j+\frac{1}{2}}^{n-\frac{1}{2}}+\dfrac{\Delta t}{\rho\left(1+\frac{1}{2}d_{j+\frac{1}{2}}^y\Delta t\right)}\dfrac{\left(\sigma_4\right)_{i+\frac{1}{2},j+1}^n-\left(\sigma_4\right)_{i+\frac{1}{2},j}^n}{\Delta y},\\
\left(\sigma_5^x\right)_{i,j+\frac{1}{2}}^{n+1}=\dfrac{1-\frac{1}{2}d_i^x\Delta t}{1+\frac{1}{2}d_i^x\Delta t}\left(\sigma_5^x\right)_{i,j+\frac{1}{2}}^n+\dfrac{\Delta t}{1+\frac{1}{2}d_i^x\Delta t}c_{55}\dfrac{\left(v_3\right)_{i+\frac{1}{2},j+\frac{1}{2}}^{n+\frac{1}{2}}-\left(v_3\right)_{i-\frac{1}{2},j+\frac{1}{2}}^{n+\frac{1}{2}}}{\Delta x},\\
\left(\sigma_5^y\right)_{i,j+\frac{1}{2}}^{n+1}=\dfrac{1-\frac{1}{2}d_{j+\frac{1}{2}}^y\Delta t}{1+\frac{1}{2}d_{j+\frac{1}{2}}^y\Delta t}\left(\sigma_5^y\right)_{i,j+\frac{1}{2}}^n,\\
\left(\sigma_4^x\right)_{i+\frac{1}{2},j}^{n+1}=\dfrac{1-\frac{1}{2}d_{i+\frac{1}{2}}^x\Delta t}{1+\frac{1}{2}d_{i+\frac{1}{2}}^x\Delta t}\left(\sigma_4^x\right)_{i+\frac{1}{2},j}^n,\\
\left(\sigma_4^y\right)_{i+\frac{1}{2},j}^{n+1}=\dfrac{1-\frac{1}{2}d_j^y\Delta t}{1+\frac{1}{2}d_j^y\Delta t}\left(\sigma_4^y\right)_{i+\frac{1}{2},j}^n+\dfrac{\Delta t}{1+\frac{1}{2}d_j^y\Delta t}c_{44}\dfrac{\left(v_3\right)_{i+\frac{1}{2},j+\frac{1}{2}}^{n+\frac{1}{2}}-\left(v_3\right)_{i+\frac{1}{2},j-\frac{1}{2}}^{n+\frac{1}{2}}}{\Delta y}.
\end{cases}
\tag{3.34}
$$

This obtained system corresponds to the PML model when an artificial attenuation is needed in both direction x and y (e.g., at the corners of the mesh). When the PML must attenuate the wave field in one direction only, the unnecessary damping factor is set to zero. For example, the damping function $d^y(y)$ is equal to zero for a PML attenuating the waves in the x-direction. Figure 3.9 shows the values of $d^x(x)$ and $d^y(y)$ for the different PMLs surrounding a rectangular physical domain.

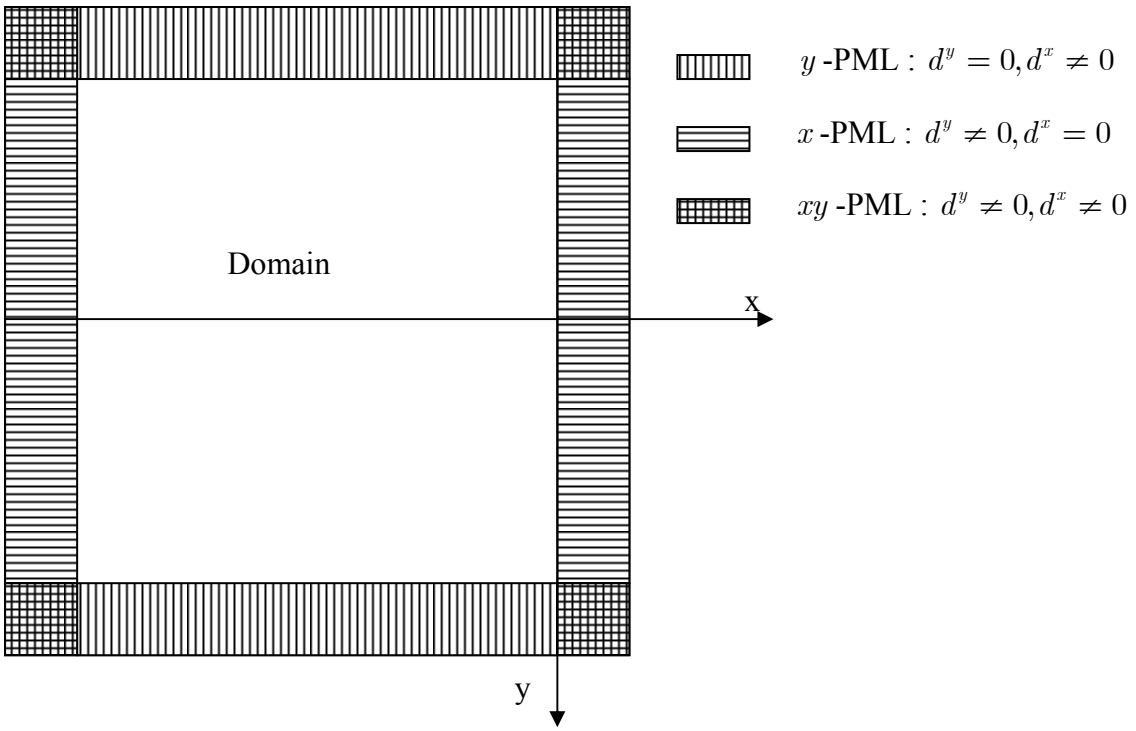

Fig. 3.9 *Perfectly Matched Layers (PMLs)*

We use a quadratic dependence for the damping factors d^x and d^y in the absorbing layers. For example, d^x is

$$d^x(x) = d_0 \left(\frac{x}{\delta}\right)^2, \tag{3.35}$$

where δ is the physical thickness of the PML and d_0 is the maximum value of the damping factor at the edge of the PML. The latter depends on the expected order of magnitude of the spurious reflectivity R (supposed to be small) and also on the thickness and material properties of the PML. For the case of SH waves, the constant coefficient d_0 estimated from the reflection of a plane wave front at normal incidence onto the PML is given by

$$d_0 = \log(\frac{1}{R})\frac{3c_t}{2\delta}, \tag{3.36}$$

where c_t is the SH-wave speed (see [5] for the details). This formula allows us to quantify the damping functions with respect to the layer thickness δ and the expected reflectivity R. The inverse proportionality of d_0 and δ in (3.36) implies low values of d_0 for a thick PML that is good for its efficiency. At the same time, a care should taken against too large values of δ, which would mean a large number of additional cells in the mesh.

Proceeding in the same manner, the PML scheme can be obtained for the case of P/SV waves. It has been implemented for the simulations presented in this work; however, its derivation will not be reported here.

3.5 Conclusion

The FDTD method described in this chapter is a classical technique resting on quite general and intuitively understandable principles. It has several important advantages. First, it is based on simple mathematics. Second, it is relatively easy to implement in any programming language. Third, it is not so much expensive in terms of computational time at least for 2D simulations, especially when using multithread programming along with multi-core processors. As the main disadvantages that one can face with such a technique, we can mention a rather complicated treatment of complex geometries and boundary conditions due to a strong dependence of the numerical scheme on the rectangular uniform mesh, and the high requirement to the RAM memory capacity for big computational domains. However, a lot of developments have been made for improving FDTD method during recent years, so nowadays there exist numerous ’tricks‘ for tackling complex physical problems and obtaining reliable results [6]. Within the purposes of the present work, the classical formulation of the FDTD scheme is largely sufficient for delivering quantitative results with a good accuracy.

References

1. K.S. Yee, Numerical solution of initial boundary value problems involving Maxwell’s equations in isotropic media, IEEE Transactions on Antennas and Propagation 40 (1966) 302-307.

2. J. Virieux, P-SV wave propagation in heterogeneous media: velocity-stress finite-difference method, Geophysics 51 (1986) 889-901.

3. J.-P. Berenger, A perfectly matched mayer for the absorption of electromagnetic waves, J. Comput. Phys. 114 (1994) 185-200.

4. W.C. Chew, Q.H. Liu, Perfectly matched layer for elastodynamics; a new absorbing boundary condition, J. Comput. Acoust. 4 (1996) 341-359.

5. F. Collino, C. Tsogka, Application of the perfectly matched absorbing layer model to the linear elastodynamic problem in anisotropic heterogeneous media, Geophys. J. Int. 66 (2001) 294-307.

6. A. Taflove, S.C. Hagness, Computational electrodynamics. The finite-difference time-domain method, Artech House, Boston, 2005.

4 Analysis and processing of FDTD numerical scheme

Table of contents

4.1 Introduction

Performing FDTD numerical simulations requires managing different parameters and satisfying several conditions. In this chapter we will consider the so-called CFL conditions for FDTD method, which must be fulfilled in order to have a numerically stable scheme. We will also touch upon problems of the numerical dispersion and numerical precision of the scheme taking into account the computational time and memory capacity needed for the high precision. Another important problem discussed in the chapter is the modelling of incident wave as a true plane wave for reflection/transmission simulations with a view to achieve a reliable comparison with theoretical results involving harmonic plane waves that are infinite in space and time.

Any numerical simulation demands data storage and efficient signal post-processing in order to extract the output acoustical information. To do so, it is necessary to save a simulated wave field in an optimal manner for further treatments which involve different signal processing methods and algorithms. The objective of FDTD elastodynamics simulations is a quantitative investigation of the different characteristics of the waves interacting with structures. Because FDTD method provides simulations in the time domain while we often need the spectral characteristics of the wave field, we should pass from the physical space to the frequency (Fourier) space. Thus, for the purpose of extracting the required data from the simulated wave field, we will extensively use FFT (Fast Fourier Transform) algorithm that is a discrete and fast approximation of the continuous Fourier transform. We will especially employ the 2D-FFT method for extracting the dispersion spectrum of guided waves. Also, we will discuss some efficient implementations of FFT such as the zero-padding technique.

Another important point in setting up FDTD simulations is the time and spectral characteristics of the acoustic sources (spectral width, time-duration of signals…). It is closely related to the aforementioned stability conditions, the plane-wave modelling, the computational time and, of course, the targeted wave characteristics that will be extracted from the simulations. We will carry out an analysis of the interrelations between all those factors.

4.2 FDTD simulation setup

Setting up FDTD simulations assumes not only the building of the FDTD cells according to the boundary conditions and material properties, but also requires fixing other crucial items including *the source definition, the stability conditions, the numerical accuracy and the data storage*. All these points will be considered in this section.

4.2.1 Numerical dispersion, accuracy and stability conditions

The discretization parameters of the FDTD numerical scheme are very important for its numerical stability and dispersion. Making more accurate schemes often leads to increasing the computational domain and the number of time steps, because it requires more discretization points (cells) per wavelength for a controlled dispersion and, as a result, a lower time stepping ensuring the stability of the scheme.

The stability of FDTD scheme is defined through the CFL (Courant-Friedrichs-Lewy) conditions [1]. In the general multidimensional case, it takes the following form for a regular Cartesian grid and time stepping [2-4]:

$$c_{\max}\Delta t\sqrt{\sum_{i=1}^{n}\frac{1}{\Delta x_i^2}}<1, \tag{4.1}$$

where n is the spatial dimension of the problem, $c_{\max}$ is the greatest local phase velocity in the whole domain, Δt is the time step and Δx_i is the spatial discretization step in the direction i. For the special case of a uniform spatial grid ($\Delta x_i = \Delta x$), (4.1) reduces to

$$\Delta t < \Delta t_{\max} = \frac{1}{\sqrt{n}}\frac{\Delta x}{c_{\max}}. \tag{4.2}$$

In this work only 2D simulations are considered and n will be therefore equal to 2. The phase velocity $c_{\max}$ will be either the shear-wave phase velocity for the SH-wave simulations, or the longitudinal-wave phase velocity for the P/SV-wave problems.

Since only uniform Cartesian grids are going to be considered for all further simulations, the inequality (4.2) constitutes the upper bound for the time discretization step in the remainder of this manuscript. While the value of Δt must be in agreement with the stability condition (4.2), the choice of Δx will condition the accuracy of the scheme and also its numerical dispersion. Roughly speaking, in order to have a simulated wave-field that does not 'feel' the lattice constituted by the discretization nodes, the spatial steps must be small

enough in comparison with the smallest wavelength in the domain. Choosing a sufficiently large number N of points of discretization per wavelength will ensure a low level of dispersion and a reasonable accuracy for the harmonic components at the highest frequencies. This choice can be formulated via the following relation:

$$\Delta x < \Delta x_{\max} = \frac{\lambda_{\min}}{N} = \frac{c_{\min}}{N f_{\max}}, \tag{4.3}$$

where N is the chosen number of points per smallest wavelength in the simulation. Here $\lambda_{\min}$ is considered as the wavelength in the slowest part of the domain at the highest frequency. Since the frequency spectra of the sources are not strictly confined to a frequency band, the highest frequency is also chosen arbitrarily. The latter is supposed to be the frequency beyond which the scheme does not have (from the user's point of view) to satisfy the same accuracy and level of dispersion as in the frequency domain of main interest. This upper frequency of interest is usually defined as the frequency at which the frequency spectrum of the source magnitude is much less than the peak magnitude of the whole spectrum of the source. Then, after this level of accuracy has been set by the choice of N, the spatial step of discretization Δx must satisfy the inequality provided by (4.3) (i.e. the spatial step must be less than the upper bound $\Delta x_{\max}$ defined from N and from the characteristics of the source and the medium). Once Δx has been specified, the time step Δt can be set in accordance with (4.2).

In practice, artificial (numerical) dispersion is one of the main problems, especially if several dozens of thousand of time steps are computed. After some trials within the context of the type of simulations we are interested in, we have noted that in order to have enough accurate numerical results with neglected numerical dispersion for the second-order scheme at high frequencies, we should consider at least 20 points per smallest wavelength (see Chapter 5). Alternatively, increasing the order of the FDTD scheme (e.g. a central fourth-order finite-difference scheme) could drastically reduce the number of points per wavelength under the same demand of accuracy and level of numerical dispersion. But the main drawback would be a higher CPU consumption and a much more difficult boundary-condition coding.

4.2.2 Spectral characteristics of the source

4.2.2.1 Limitation of the spectral width of the source

It has already been mentioned that time and spectral characteristics of the source play a very important role in the numerical simulation. As seen in equation (4.3), the discretization spatial step must be inversely proportional to the highest frequency in the simulation, which means that Δx has to be set in accordance to the highest frequency in the spectrum of the source. Hence the frequency content of the source will be chosen in view of both the desired frequency-range for the simulation and the capacity of the hardware.

4.2.2.2 Signals for sources

Most generally, the choice of the source (punctual or extended, harmonic or transient, tone burst etc.) is conditioned by the physics of the problem under simulation. At the same time, the goal of a simulation can be to provide and highlight specific properties of the wave field, such as reflection/transmission coefficients or dispersion diagrams. The latter is the case in the present work, where therefore the choice of the type of sources will be subject only to constraints of display, processing or alike. For instance, as explained in the Section 4.2.3, we aim at visualizing dispersion curves of surface waves in the $\left(\omega, k\right)$-space as spectrum intensity images. In order to get uniform pictures in intensity allowing then a clear display of the dispersion curves trajectories, the acoustic source must have a rather flat frequency spectrum in the range of interest. The sine cardinal function is therefore appropriate for such image construction in the spectral domain (flat and bounded spectrum), whereas it is not so suitable in the time domain. For FDTD simulations, the sine cardinal function has a too small decay in time ($\sim t^{-1}$). For circumventing the long duration of the sine cardinal pulse (very long time for the source to establish itself), its amplitude is modulated in time by a Gaussian envelope. The typical function used is as follows:

$$s(t) = \Pi(t)\,\mathrm{e}^{-\alpha t^2}, \tag{4.4}$$

where

$$\Pi(t) = \frac{\sin(2\pi t/\tau)}{2\pi t/\tau}. \tag{4.5}$$

In the Fourier space, the sinc function has a finite-width spectral window $\left[-\frac{1}{\tau}, \frac{1}{\tau}\right]$, in which the amplitude remains constant throughout the interval. The amplitude modulation

provided by the Gaussian envelope in the expression (4.4) speeds up the decay of the sinc function at large values of time (see Fig. 4.1), without modifying too much the spectrum of $\Pi(t)$. For small values of α the spectrum of $s(t)$ is roughly speaking of trapezoidal shape (see Fig. 4.3). In addition, the amplitude of the source at time $t = 0$ (first step of time in our simulations) should be very close to zero in order to keep smooth time variations. Therefore the signal $s(t)$ must be sufficiently time shifted ($s(t - t_0)$).

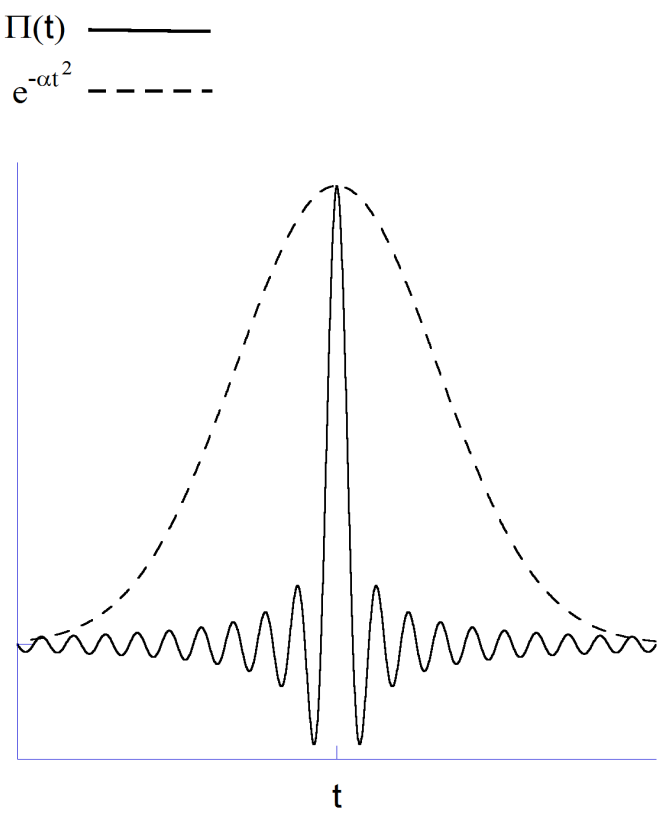

Fig. 4.1 *Superposed function of cardinal sin and Gaussian envelope give the function presented in Fig. 4.2*

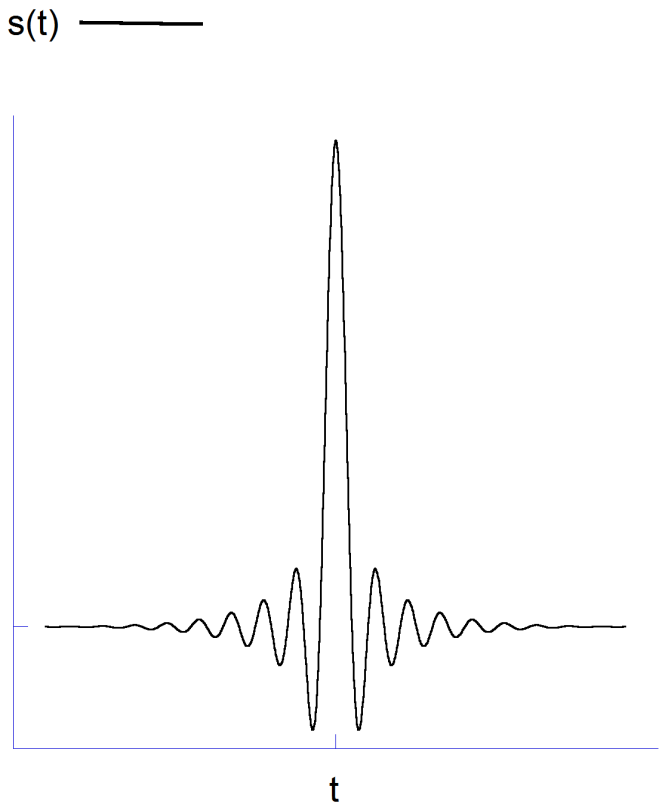

Fig. 4.2 *Typical signal* $s(t)$ *issued from (4.4) as a source for simulations*

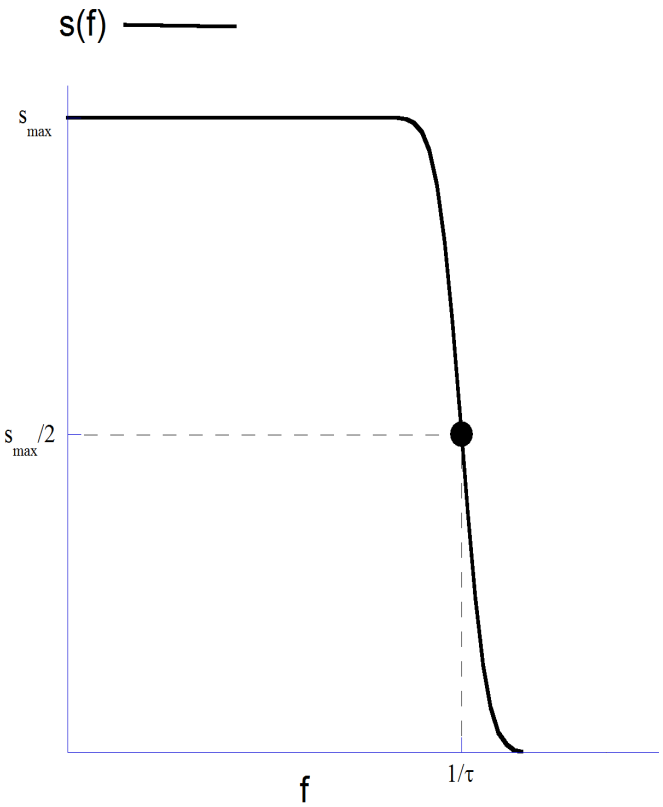

Fig. 4.3 *Spectrum of signal* $s(t)$ *issued from (4.4).*

4.2.3 Example of FDTD simulation setup

Let us use a concrete example to show how the different parameters of FDTD simulation can be specified. We consider a simulation for SH waves. We choose an isotropic material with the following properties:

$$\rho = 1\,\mathrm{g/cm^3}, \quad c_t = 1\,\mathrm{mm}/\mu\mathrm{s}$$

for the whole computational domain. A punctual-force source is considered in the bulk of the medium and is taken in the form

$$\mathbf{F}(\mathbf{r},t) = \mathbf{f}(\mathbf{r})s(t) = \mathbf{F}_0\delta(\mathbf{r}-\mathbf{r}_0)s(t), \tag{4.6}$$

where $\mathbf{r}_0$ is the vector position of the punctual source. For this example, we have chosen $\tau = 1\,\mu\mathrm{s}$ and $\alpha = -0.05\,\mathrm{mm}^{-1}$ in $s(t)$. The shape of the frequency spectrum of the generated signal has approximately a trapezoidal shape in the interval $|f| = |\omega/2\pi| < 1\,\mathrm{MHz}$. As one can see in the Fig. 4.4, the amplitude spectrum of $s(t)$ is relatively flat until about 1 MHz, while it spreads up to infinity beyond $1\ \mathrm{MHz}$ but with a rapidly decaying amplitude. Therefore we will adopt that the maximum frequency to be taken into account in the simulation is $f_{\max} = 1\,\mathrm{MHz}$, from which the shortest wavelength $\lambda_{\min}$ is going to be determined as

$$\lambda_{\min} = \frac{c_t}{f_{\max}} = \frac{1}{1} = 1\,\mathrm{mm}. \tag{4.7}$$

If we choose to resolve the shortest wavelength with 20 samples ($N = 20$) then, according to the formula (4.3), the spatial discretization should be such that

$$\Delta x \le \frac{1}{20} = 0.05\,\mathrm{mm}. \tag{4.8}$$

Thus, using (4.2) we obtain the following CFL condition

$$\Delta t \le \frac{1}{\sqrt{2}}\frac{0.05}{1} \approx 0.035\,\mu\mathrm{s}. \tag{4.9}$$

Now, having specified the conditions for the discretization steps of the space-time grid, we return to the source expression (4.6) to consider the time delay t_0 within $s(t)$ in order to start the simulation with a sufficiently small amplitude of the source at the first time step. In the present example, we see that taking $t_0 = 12\,\mu\mathrm{s}$ yields less than 10^{-7} for the ratio of the

amplitude of the source at $t = 0\,\mu s$ to its overall peak value. The input signal source and its amplitude spectrum are shown in the Fig. 4.4.

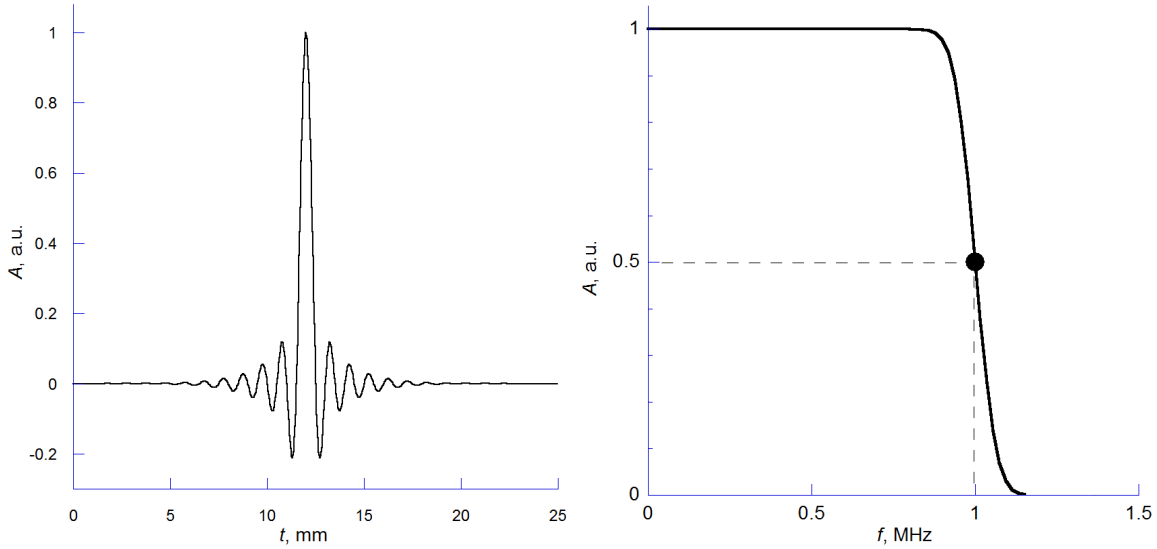

Fig. 4.4 *Transient and spectral characteristics of chosen signal*

4.2.4 Plane wave model

Simulations of realistic problems usually imply that sources are localized in space and time. However, modelling of a plane wave can be necessary when using FDTD codes for accessing numerically spectral properties of acoustic fields such as, for instance, reflection and transmission coefficients of plane waves or scattering coefficients of objects. Concerning the ω-spectral properties, there is no particular problem in using transient sources, since any properties can be accessed in the frequency domain via Fourier transform of the output data of the time simulation. If the running time of the simulations is long enough, the full range of frequency contained within the source is analysable, even for small values of ω. On the other hand, for the spatial-frequency domain, the (spatial) Fourier analysis often requires large domains of simulation and consequently long running time for ensuring good spectral resolution (in wavenumber). So it may be preferable to simulate directly the generation of the plane wave. Moreover, sometimes there is no alternative. In particular, the multiple scattering problems, dealt with in our study, necessitate modelling of the incident wave as a plane wave since the overall interaction of the incoming waves with the whole set of scatterers is not spatially invariant for Fourier analysis.

In this section, modelling of a plane wave in the FDTD simulations is discussed. Our code enables two methods for generating transient plane waves. The first method uses initial condition for the wave field before the code starts to run, and the second one employs a very wide line source. The initial condition approach imposes the exact spatial wave field of a transient plane wave where it exists in the whole domain, including the PML if necessary. This technique is relatively easy to implement so long as the direction of propagation coincides with one of the principal axes of the rectangular mesh and hence the spatial extension along the direction of propagation is limited (transient acoustic pulse) while the lateral extension of the plane-wave front disappears into the PML. On the other hand, if the plane wave propagates obliquely with respect to the mesh axes, then the above simulation demands a very large computational domain in order to well resolve the oblique plane front and to handle the plane wave mismatching the PML. In this case, the preferable method is such that uses a line source, along which a phase delay is performed to generate an oblique wave.

4.2.4.1 Generation of the incident wave from the initial conditions

In this section, the implementation of the plane-wave initial conditions (IC) in the computational domain is explained. The main idea is to arrange the initial values of the velocity and stress field components at the time $-\Delta t$ and $-\Delta\frac{t}{2}$ within the specified area in such a way that the spatial distribution of the wave-field components corresponds to a transient plane wave propagating in a chosen direction. In order to do so, it is necessary to set appropriate values of stress and velocity at the nodes of the mesh within the IC area. Outside this zone, the components of the wave field are set to zero.

In the following, the implementation for the case of SH waves is elaborated (the generalization for P/SV waves is straightforward). With no loss of generality, the propagation direction of the plane wave is chosen as the y-direction. An important prerequisite of this technique is that the zone of setting IC must correspond to a part of the propagating medium where it is homogeneous in order to admit a local solution in the form of a plane wave field. We start by writing the displacement field u of the transient plane SH wave propagating in the y-direction in the general form

$$u\left(t,x,y\right)=f\left(t-\frac{y}{c}\right), \tag{4.10}$$

where $c = \sqrt{\frac{c_{44}}{\rho}}$ is the wave speed of SH-waves in the direction y, and the function f corresponds to the transient signal of the plane wave. Recalling that we work in a velocity-stress formulation in the FDTD model, the velocity field v_3 of the SH wave is given by

$$v_3 = \frac{\partial u}{\partial t} = f'\left(t - \frac{y}{c}\right). \tag{4.11}$$

From constitutive equations (3.25) for SH waves it follows

$$\begin{aligned} \sigma_4 &= c_{44}\frac{\partial u}{\partial y} = -\frac{c_{44}}{c} f'\left(t - \frac{y}{c}\right), \\ \sigma_5 &= c_{55}\frac{\partial u}{\partial x} = 0. \end{aligned} \tag{4.12}$$

Thus, denoting

$$v_3 = f'\left(t - \frac{y}{c}\right) = F\left(t - \frac{y}{c}\right), \tag{4.13}$$

we obtain for the stress field

$$\begin{aligned} \sigma_4 &= -\frac{c_{44}}{c} F\left(t - \frac{y}{c}\right) = -\sqrt{\rho c_{44}} F\left(t - \frac{y}{c}\right), \\ \sigma_5 &= 0. \end{aligned} \tag{4.14}$$

Finally, the conditions that should be applied in the IC area are

$$\begin{cases} v_3 = F\left(t - \frac{y}{c}\right), \\ \sigma_4 = -\sqrt{\rho c_{44}} F\left(t - \frac{y}{c}\right), \\ \sigma_5 = 0. \end{cases} \tag{4.15}$$

Therefore, it suffices to apply these conditions at the initial values of time of the simulation, and to let run the FDTD code according to the leap-frog scheme. If $t = \Delta t$ is the first instant at which the quantity v_3 is updated, then the stress field $\sigma_4\left(x, y, t = \frac{\Delta t}{2}\right)$ and the velocity field $v_3\left(x, y, t = 0\right)$ must be determined according to (4.15). Concerning the size of the spatial area wherein the initial conditions are set, the extent of this zone along the propagation direction is related to the function $F(t)$ (i.e. the signal itself). The longer the signal, the longer the length of this area. Moreover, if the signal F does not formally have a compact support, then the area, which should be finite in practice, must include most of the part of the wavelet. It means that the amplitude of the plane wave at the border of the IC area must be small enough in

order to sufficiently reduce spurious generation of acoustic field. Practically, we demand that the ratio of the amplitude at the border of the IC area to the maximum amplitude in the overall signal should be less than 10^{-6}.

Another important point in emulating the theoretically infinite plane-wave front is that it is useful and efficient to terminate the lateral borders of the IC area within the PML. By this way, the effect of finite lateral extent of the IC area is 'absorbed' by the PML, and the planar front of the initial field is conserved all along the simulation.

In conclusion, it is in order to remark that designing initial conditions for emulating an obliquely incident plane wave is not an easy matter. For such a case, the initial wave field should be parameterized by the two space variables x and y as $F\left(t - s_x x - s_y y\right)$, where s_x and s_y are the two components of the phase-slowness vector $\mathbf{s}$ of the plane wave. The IC area may be limited in the direction of $\mathbf{s}$ due to the 'compact' nature of the transient plane wave, but it must be of infinite extent orthogonally to $\mathbf{s}$ (plane-front feature), which means in practical terms that it must disappear into the PML. This may require a very large simulation grid and may even be not applicable to the problem in hand. For instance, the fact that the obliquely incident plane front will theoretically 'always' interact with the interface, despite that the incident wave is transient, makes it very difficult to simulate the reflection/transmission problem numerically – in contrast to the case of a normally incident plane wave. Since the IC area incorporates both media in contact, specifying the initial field on both sides of the interface would require to solve the problem for the initial field itself before running the simulation! Therefore the technique of the line-source with a phase delay will be reserved for generating oblique plane fronts.

4.2.4.2 Generation from a line source

The technique of using a line source for generating plane fronts is a rather conventional approach and may look simple at the first sight. However, our simulation tests have revealed certain technical problems to be fixed for making the technique efficient.

The idea of the plane wave generation by the line source is basically as follows. In order to launch a plane wave in a given direction, we may consider a set of points (i.e. FDTD cells) on a straight line parallel to the horizontal or vertical edges of the grid, and impose the same punctual source at every point along this set (possibly a linear combination of the different types of volume sources) for controlling the polarization of the plane front. It means that we

assign a transient function (discretized according to the time step $\triangle t$) to the volume sources f_i and h_j in the discrete elastodynamic equations of FDTD.

In view of the Huygens principle, a plane front (or several fronts depending on the linear combination of sources) will be generated and will propagate perpendicular to the line source. This technique does not allow to 'launch' a plane front toward only one side of the line source, but it emits a wave field on both sides. Practically the backward wave (the one that is undesirable in the simulation) is not a real concern as long as it is going to disappear into the PML. If otherwise, then another approach should be applied. The overall constraint in using line sources as a system of emission is to comply with the mesh. Generating plane fronts along the directions of the rectangular mesh is easy. If however the source is not oriented along the mesh, then, due to the rectangular discretization grid, the actual line-source does not pass via the nodes of discretization. Therefore a phase shift must be applied on the neighboring nodes in the vicinity of the line source. The technique is still applicable but is a little more complicated. With such an approach, we have realized the plane-front generation with a relative amplitude variation along the phase front of less than 10^{-4}. Such accuracy is largely sufficient for the simulations performed in our studies.

The issue of the endpoints of line sources (smoothing effects of truncation)

While the efficiency of the line source technique is sufficient for a good resolution of the plane front itself, the ending points of the line source on their own introduce artifacts in the generated wave field. These points do not have adjacent source points on one side. Such a situation leads to a discontinuity in the source spatial function and provides an additional circular wave front (centered on the ending point) which is of $10^{-1} - 10^{-2}$ order of magnitude relatively to the amplitude of the plane front. This parasite wave cause errors in the simulations involving incident plane waves.

For circumventing this problem, or at least for reducing drastically the contribution of those artifacts, we introduce a transition zone at the ends of the line source for which the amplitude of the source function $F(t)$ is scaled by a smoothly varying factor running from 1 to 0. The purpose of these zones is to reduce the parasite effects of the end points of the line source by removing the jump due to the finite length of the source.

Let us show how we have chosen the scaling function that enables a smooth varying amplitude in the transition zones. First we fix a segment of length L within the line source, where the signal of the source will be the same at all points (no scaling of the amplitude). Hereafter, x is the coordinate along the line source and $x = 0$ corresponds to the center of the line. Outside of the zone of uniform source function ($|x| > \frac{L}{2}$), the scaling zones of length l_{scal} are considered. The scaling function is chosen in such a way that no jumps in the source function and in its derivative occur at the points $|x| = \frac{L}{2}$. At the same time, a sufficiently strong decay toward the edge of the line source is required. Using a Gaussian-type function with a power factor of 3 has proved to be a good compromise between the decay at the edges $|x| = \frac{L}{2} + l_{scal}$ and the smoothness of the profile at the points $|x| = \frac{L}{2}$. The scaling function, which we have used most often, is thus as follows:

$$A(x) = H\left(\tfrac{L}{2} - |x|\right) + H\left(|x| - \tfrac{L}{2}\right)\exp - \left(\alpha \frac{|x| - \frac{L}{2}}{l_{scal}}\right)^3, \tag{4.16}$$

where α is related to the desirable decay rate and $H(x)$ stands for the step-function

$$H(x) = \begin{cases} 0 & \text{when} \quad x < 0 \\ 1 & \text{when} \quad x \geq 0 \end{cases} \tag{4.17}$$

Note that though this technique is supposed to drastically reduce the artifacts of the edges of the line source, some parasite waves (with small amplitude) still exist and perturb the plane front. In practice, the width of interest is reduced to a smaller size in order to move it away from the first point of varying amplitude. This is to secure the zone of interest where we can ensure a plane front with constant amplitude.

In conclusion, we demonstrate an example of scaling function used with a line source. Suppose that the simulation requires a plane front with constant amplitude in the interval of $25\,\mathrm{mm}$ width. On both sides of this interval, the unscaled area is first extended in order to move aside the beginning of the transition zone from the plane-front interval of interest. This extension is chosen here as 50% of the width of plane-front interval, that is $12.5\,\mathrm{mm}$. Adjacent to this interval is the transition zone where the scaling function is used to decrease the amplitude of the source toward the edge of the line. This transition zone must be relatively long compared to the plane-wave interval of constant amplitude. In practice, we have noticed that the decay zone must be at least as long as the constant-amplitude zone. In the considered example, choosing them of the same width gives the decay zone of $50\,\mathrm{mm}$. On the whole, the

total width of the line source represents 300% of the initial width of the desired plane front. It is at this expense that we can drastically reduce the drawbacks of the edge effects.

The scaling function $A(x)$ for the above configuration is therefore

$$A(x) = H(25 - |x|) + H(|x| - 25)\exp - \left(\alpha \frac{|x| - 25}{50}\right)^3 . \tag{4.18}$$

Fig. 4.5 shows the shape of the function $A(x)$ with the factor α equal to 2. With such value for α, the magnitude of the source is multiplied by a factor of the order of 10^{-4} at the edges. The wave field generated from the transition zone has thereby minor consequences on the front located in the initial area $|x| \leq 12.5\,\mathrm{mm}$.

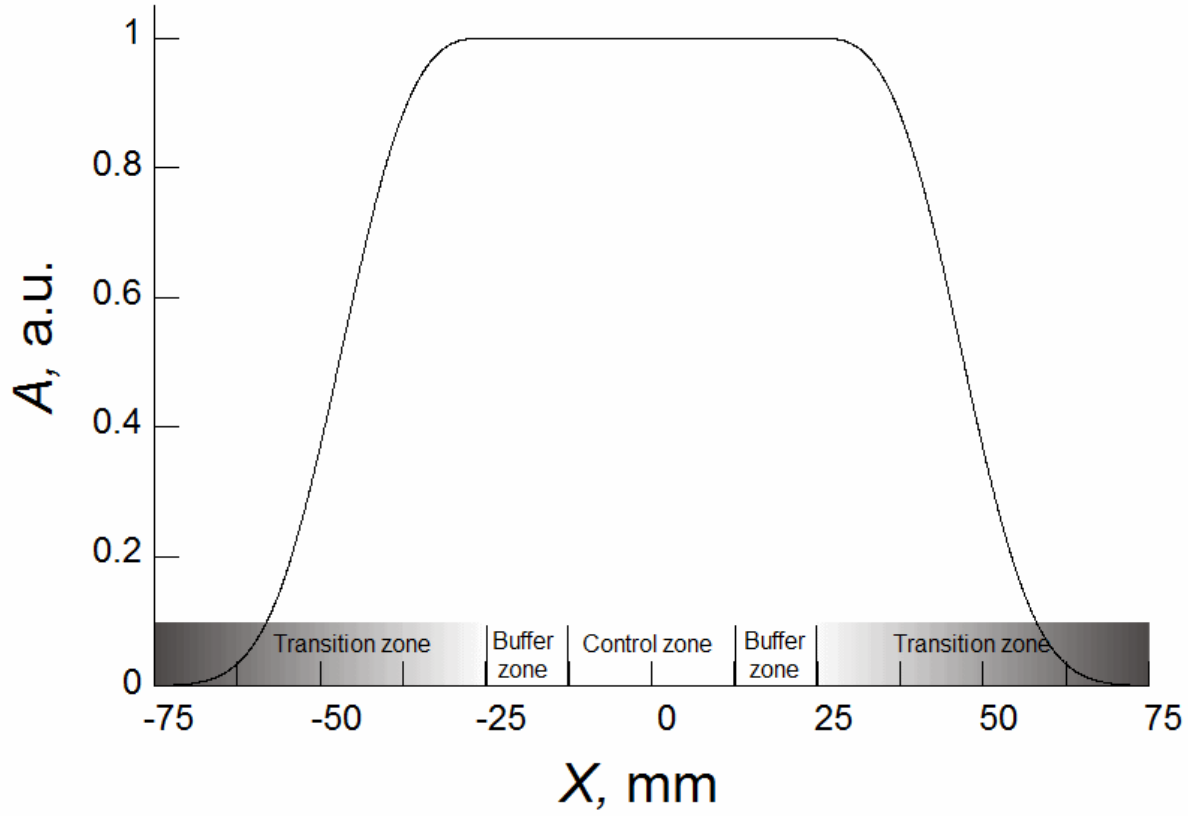

Fig. 4.5 *Example of scaling function along the line source.*

The issue of oblique plane-front generation (modeling obliquely incident plane wave)

Another important problem tackled in our numerical simulations is the generation of oblique plane fronts with a prescribed angle of propagation. As it has been discussed above, the technique of initial conditions for generating oblique plane fronts is not really appropriate due to a too large increase of the computational domain. It has also been noted that the use of an oblique line source is not an easy-to-use technique because the line does not cross the

nodes of the mesh. That is why the method of the line-source is retained. It enables to deal subsequently with a reasonable grid size.

Up to here, we have been considering source functions defined as products of a function of time by a function of space variables. Now the idea is to consider a moving source which is modeled by coupling the time and space variables in the source function. A supersonic source enables the generation of a conical wave (Mach wave front) whose angle of propagation is directly determined by the speed of the apparent motion of the source. The corresponding formula for isotropic media is

$$v = \frac{c}{\sin\theta}, \tag{4.19}$$

where v is the speed of the moving source, c is the speed of the plane front to be generated into the bulk and θ is the half-aperture angle of the Mach cone or, in other words, the angle of propagation of the plane front with respect to the normal to the line source. The time source function corresponding to the signal of the oblique plane wave is then coupled to space variable, say x, according to the relation

$$F\left(t - \frac{x}{v}\right) = F\left(t - x\frac{\sin\theta}{c}\right). \tag{4.20}$$

The main advantage of this technique is that it enables quite a precise tuning of the value of the incident angle θ and also an accurate control of the quality of the synthesized oblique plane front (constant amplitude and phase along a straight line). If required, a scaling function in space can be employed, as in the previous section, for avoiding the effects of the edges of the line-source. In general, a source function $F(t,x) = f_t(t) f_x(x)$ (giving rise to the wave propagating in the y-direction), which is uncoupled in time and space, can be used for generating plane fronts with the same given time signal but with arbitrary angle of propagation θ with respect to y. This angle can be chosen by simply connecting the time variable with the motion of the source:

$$F(t,x) \rightarrow F\left(t - x\tfrac{\sin\theta}{c}, x\right). \tag{4.21}$$

Note that applying the similar equations to the case of anisotropic media implies replacing the factor $\frac{\sin\theta}{c}$ with the slowness component s_x of the chosen plane front, where s_x is defined by the Christoffel equation and the chosen angle of incidence θ.

4.3 Signal processing

The aim of any numerical simulation is a quantitative investigation of physical phenomena. For the present case of elastic-wave propagation, we certainly access the transient field in the time and space domain, but we may also need some spectral characteristics, such as reflection/transmission spectra and/or velocity dispersion of guided waves. In this case, the output data of the simulations should also be read in the frequency space. Analysing data both in time and space frequencies presumes an intensive use of the Fast Fourier Transformation.

4.3.1 Some technicalities on the storage of the wave field

In order to extract the desired characteristics from the simulation, we first of all need to store the calculated field in the efficient way. This implies that the computer memory should not be overloaded (primarily by reducing the writing of data onto the hard drive) due to selecting only the information required for post-processing. At the same time, the data must be saved in the most convenient form for optimal application of the FFT algorithm. To satisfy these requirements we have designed specific oriented-object tools in our FDTD code.

These programming tools include geometrical sub-area within the computational domain, for which the field components are saved according to some predefined rules such as probing the field at each node, probing periodically (skipping some nodes and therefore avoiding a too high sampling rate for the data extraction), choosing some particular components of the wave field and disregarding others, etc. The typical ways of extracting data are: a one-point probing (obtaining just a single signal at a node), a straight-line probing of the field along the direction of a rectangular mesh (obtaining a 1D-array of time-signals), and also a rectangular area (a 2D-array of time-signals). Usually these three ways of probing are used in order to extract different types of acoustical properties. Point-probes are used for investigating local transient fields, to which the FFT algorithm can be applied to access the frequency content at that point. The line-probes may be considered as a list of point-probes, for which there is a possibility of performing a 2D-FFT in order to read the field in the frequency and wave-number domain ($[t,x] \overset{Fourier}{\longrightarrow} [\omega,k]$), with the aim of extracting dispersion features like e.g. dispersion curves of guided waves. Rectangular probes are used for

performing 3D-FFT on the transient field and analyzing the wave field in the (ω, k_x, k_y)-space. The latter procedure allows a plane-wave angular spectrum reading of the data.

4.3.2 Fourier analysis of the discrete data (Fast Fourier Transform)

In this work, we use the following definition of the Fourier transform $F(\omega)$ of a function $f(t)$:

$$F(\omega) = \int_{-\infty}^{\infty} f(t) \mathrm{e}^{\mathrm{i}\omega t} \mathrm{d}t, \tag{4.22}$$

where the Fourier transformation parameter ω is the angular frequency $\omega = 2\pi f$. The inverse Fourier transform is then given by

$$f(t) = \frac{1}{2\pi} \int_{-\infty}^{\infty} F(\omega) \mathrm{e}^{-\mathrm{i}\omega t} \mathrm{d}\omega. \tag{4.23}$$

Since the wave fields in many numerical problems are sampled over time and space, the Fourier transforms are only accessible via their discrete approximation, namely, the Discrete Fourier Transforms (DFT):

$$F_k = \sum_{n=0}^{N-1} f_n \mathrm{e}^{-\frac{2\pi \mathrm{i}}{N} nk}, \quad k = 0, \ldots, N-1 \tag{4.24}$$

where $f_n = f(t_n)$ and $F_k = F(\omega_k)$ are the N sampled values of the signals in the original space and the N sampled values of the spectrum in the transform space, respectively. The sampling of both the original and transformed functions is performed over the uniform grids with a constant step Δt and $\Delta\omega$.

The Fast Fourier Transforms (FFT) are efficient algorithms for evaluating the DFT (4.24) which reduce the number of required elementary operations from the order of N^2 to the order of $N \log N$. This drastic decrease of time of computation of the DFT via the FFT has rendered the latter quite popular and very often essential in a wide variety of applications, and especially in the multi-dimensional form of the DFT, for which the FFT have to be engaged for keeping CPU times reasonable.

In our context, after a FDTD simulation is completed, we access the transient wave field as an array of data of length N corresponding to the time window of the physical running time of the simulation. Denote this time window as $t \in [0, T]$. The discretization parameters of the time signals are:

- N : the number of samples;
- Δt : the sampling step in time;
- $t_n = n\Delta t$: discretized values of time ($n = 0,...,N-1$);
- $T = N\Delta t$: the length of the signal (or period of the signal in the FFT context);
- $\Delta f = \frac{1}{T} = \frac{1}{N\Delta t}$: the sampling step in frequency (also the least non zero frequency in the discrete spectrum);
- $f_{\max} = \frac{1}{2\Delta t} = \frac{1}{2} f_{samp}$: the maximum frequency contained in the discrete spectrum, that is half the sampling frequency f_{samp} of the time signals;
- $f_n = n\Delta f - f_{\max}$: discretized values of frequency ($n = 0,...,N-1$).

4.3.3 2D-FFT (dispersion features)

One way to access the quantitative description of wave dispersion (say, the spectrum of guided waves) is to analyze the spectral content of propagating signals in the frequency-wave number domain. The 2D Fourier transformation of signals in the physical space (t,x) is a simple approach for obtaining the spectral characteristics in the (ω,k) space. This may be done by applying successively the 1D Fourier transforms, first over the time variable and then over the space one. The 2D continuous Fourier transform is defined for our acoustical problems as follows:

$$F(\omega,k) = \int_{-\infty}^{\infty}\int_{-\infty}^{\infty} f(t,x)\,\mathrm{e}^{-\mathrm{i}(kx-\omega t)}\mathrm{d}t\mathrm{d}x\,, \tag{4.25}$$

which can be evaluated (approximated) by using a multi-dimensional FFT algorithm.

In our simulations, the discretized functions are known over the interval $t \in [0,T]$ and $x \in [0,L]$, where T is the duration of the signals, and L is the length of the line along which the wave-field is probed, with $L = M\Delta x$ and M being the number of samples in space. The time-sampling parameters are those defined in the previous subsection. For the space discretization, the following for sampling parameters are introduced (recalling that $k = 2\pi\nu$):

- M : the number of samples;
- Δx : the sampling step in space;
- $x_m = m\Delta x$: discretized values of space ($m = 0,...,M-1$);
- $L = M\Delta x$: the length of the spatial probed area;
- $\Delta\nu = \frac{1}{L} = \frac{1}{M\Delta x}$: the sampling step in spatial frequency;

- $\nu_{\max} = \frac{1}{2\Delta x} = \frac{1}{2}\nu_{samp}$: the maximum frequency contained in the discrete spatial spectrum;
- $\nu_m = m\Delta\nu - \nu_{\max}$: discretized values of spatial frequency ($m = 0,...,M-1$).

For many practical reasons (the way of storing the data, the necessity of re-arranging the data according to the requirements of the N[th]-dimensional FFT, the problems of contiguous memory allocations for large amount of data, etc.), we have adopted the approach of performing successive 1D-FFT rather than using directly a 2D-FFT. This enables us to divide the whole set of data into different parts of the computer RAM. The latter point can be crucial for very large simulation size. In this regard, transforming the data from the physical space to the 2D-transformed space implies building an array with two entries $s_{nm} = s(t_n, x_m)$ of the discrete values of $s(t,x)$. Each line m in this 2D-array is formed by the values of the discrete signal at points x_m as it can be seen in Table 4.1. Then the FFT is applied to each line m in order to switch from temporal description to frequency description $(t \to \omega)$. As the next step, the FFT is applied to each column of the new table for switching from spatial description to wave number description $(x \to k)$. Finally we obtain a 2D table (see Table 4.2) whose entries correspond to the amplitude of the spectrum at (ω_n, k_m).

	t_0	t_1	⋯	⋯	t_n
x_0	$s(t_0,x_0)$	$s(t_1,x_0)$	⋯	⋯	$s(t_n,x_0)$
x_1	$s(t_0,x_1)$	$s(t_1,x_1)$	⋯	⋯	$s(t_n,x_1)$
⋯	⋯	⋯	⋯	⋯	•••
⋯	⋯	⋯	⋯	⋯	•••
x_m	$s(t_0,x_m)$	$s(t_1,x_m)$	•••	•••	$s(t_n,x_m)$

Table 4.1 *Signal table for 2D-FFT.*

	ω_0	ω_1	⋯	⋯	ω_n
k_{x0}	$S(\omega_0,k_0)$	$S(\omega_1,k_0)$	⋯	⋯	$S(\omega_n,k_0)$
k_{x1}	$S(\omega_0,k_1)$	$S(\omega_1,k_1)$	⋯	⋯	$s(\omega_n,k_1)$
⋯	⋯	⋯	⋯	⋯	•••
⋯	⋯	⋯	⋯	⋯	•••
k_{xm}	$S(w_0,k_m)$	$S(\omega_1,k_m)$	•••	•••	$S(\omega_n,k_m)$

Table 4.2 *Result table after 2D-FFT.*

Among plenty of different methods of displaying spectral data, we choose the one that uses 2D-graphs in the (ω, k) space and assigns color values to the pixels (n, m) of the digitized graph according to the magnitude of the sampled spectrum $S(\omega_n, k_m)$. Doing so, one can visualize the distribution of the wave-field spectral content in the (ω, k)-space and thereby the dispersion curves of guided waves (see Fig. 4.6). This tool will be extensively used below for the quantitative and qualitative analysis of the dispersion spectrum of shear acoustic waves guided by the surface of a periodic half-space.

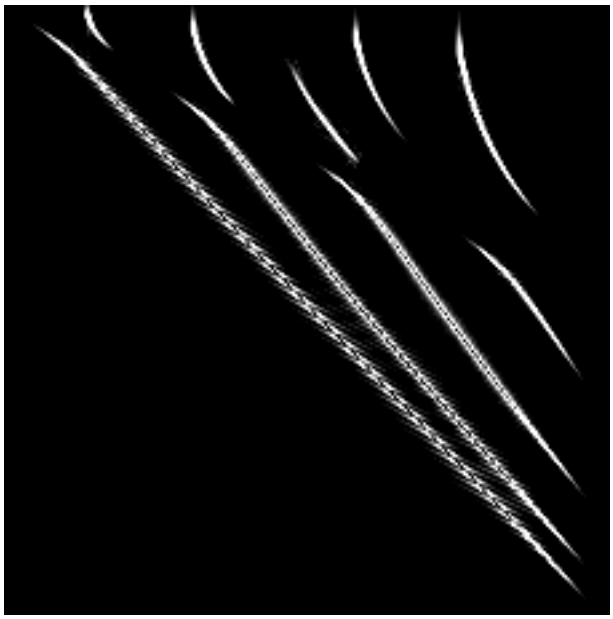

Fig. 4.6 *Example of the dispersion curves in white and black*

4.3.4 Increasing resolution in the spectral domain (zero-padding technique)

In this section, we describe a technique that was used for optimizing the procedure of reading the output data and thus reaching a better resolution in the spectral domain without affecting the size of simulation (i.e. keeping a constant number of time steps and a constant spatial grid). From the set of discretization parameters listed in §4.3.2 and §4.3.3, we can observe that the sampling step in the transformed space depends on the length of the discrete signal in the physical space. It means that a priori we can obtain a better sampling in the transformed space by increasing the duration of the simulations and by increasing the area where the wave field is probed. The major consequence of that would be a much longer running time of simulations only for the sake of increasing spectral resolution of data that we have already at hand.

A simple and efficient way to reach a better sampling step in the spectral domain is the zero-padding technique. Its idea is to artificially increase the length of the signals in the physical space without modifying the spectral content of the original signals. This is done by appending a list of zero-valued samples to the end of the signals. The signals are longer and the spectral resolution is therefore higher (i.e. $\Delta\omega$ is smaller).

The same technique may be applied for the spatial Fourier Transform $x \rightleftharpoons k$ in the 2D-FFT, for instance, to provide a better resolution of the dispersion curves. At the same time, this technique is certainly not a 'magic trick'. If there is not enough information in the signals in the time domain, we cannot gain higher accuracy in the frequency domain.

4.4 Conclusion

In this chapter, we have discussed some essential elements of running the FDTD simulations of acoustic problems and of the intelligent way of extracting the data of interest. It was pointed out that the choice of the FDTD parameters must satisfy the stability conditions and that it strongly depends on the spectral and transient characteristics of the source. Examples were provided to illuminate how specific types of simulations can be organized.

References

1. A. Taflove, S.C. Hagness, Computational electrodynamics. The finite-difference time-domain method, Artech House, Boston, 2005.

2. J. Virieux, P-SV wave propagation in heterogeneous media: velocity-stress finite-difference method, Geophysics 51 (1986) 889-901.

3. J. Max, Methodes et Techniques de Traitement du signal et application aux mesures physiques, Masson et C, Paris, 1972.

4. D. Royer, E. Dieulesaint, Ondes élastiques sans les solides, Masson, Paris, 1996.

5 Numerical results for the SH surface waves in periodic structures.

Table of Contents

5.1 Introduction

In this chapter we will present numerical results extracted from the FDTD modeling of the SH wave propagation in vertically periodic structures which was analytically described in Chapter 2. Some technical details will be given on the simulation set-up and the procedure of retrieving the numerical results and on their comparison with the analytical predictions. The main issue in setting up the numerical simulation is to find such configurations and such parameters of post-processing treatment which provide the optimal compromise between the accuracy of the results and the computing resources requirements.

With this objective, we will provide a numerical demonstration for a simple case of SH guided waves in a bilayered plate. We will describe the simulation parameters and elaborate details of the performed post-processing. Then we will pass to the more complicated cases of the SH surface waves (SHSW) in a periodic halfspace and periodic semi-infinite strip. We will consider both continuously inhomogeneous and piecewise homogeneous unit cells. For confirming consistency of our surface-wave modeling, we will recover the distribution of signal amplitude through the depth of the halfspace and compare it with the Floquet exponential form predicted by the theory. We will also analyze the numerical precision of performed simulations.

5.2 Example of SH guided waves in a bilayered plate

Let us demonstrate the application of FDTD technique to the propagation of SH guided waves in a bilayered plate. The two layers constituting the plate are assumed to be homogeneous, that is, with constant values of mass density and transverse-wave phase velocity. These values and the thickness d of the layers are chosen to be

$$\rho_1 = \rho_2 = 1\,\mathrm{g/cm^3},\ c_{t1} = 1\,\mathrm{mm}/\mu\mathrm{s},\ c_{t2} = 2\,\mathrm{mm}/\mu\mathrm{s},\ d_1 = d_2 = 1\,\mathrm{mm}\,. \tag{5.1}$$

In the following, the axes X and Y are, respectively, parallel and orthogonal to the plane of interfaces between the layers. We shall verify the predictions made in the Chapter 2 by simulating a time-space SH wave field in this bilayered plate by means of the second-order FDTD method.

The numerical simulation is as follows. In order to visualize the full spectrum within the frequency range of 0 to 5 MHz, a surface punctual source generating SH transient waves is taken in the form described in the Section 4.2.2.2 of the Chapter 4 (cardinal sine)

$$f_3(\mathbf{r},t) = F_3\delta(\mathbf{r}-\mathbf{r}_0)\frac{\sin\left(10\pi(t-t_0)\right)}{10\pi(t-t_0)}\mathrm{e}^{-0.05(t-t_0)^2}, \tag{5.2}$$

where $\mathbf{r}_0$ locates the point source at the top free surface. This time function of the source is convenient because its frequency spectrum is flat within the chosen range. Therefore it will enable getting (ω,k)-spectrum from one simulation only, and it will be scaled by the source uniformly throughout the frequency range (see §4.2.2.2). We have chosen $\Delta x = \Delta y = 0.01\,\mathrm{mm}$ for the spatial discretization of the $42\,\mathrm{mm}$ long and $2\,\mathrm{mm}$ thick computational domain in the plate, which corresponds to a grid of 4200×200 cells along the axis *X* and *Y*, respectively. For the highest frequency in the simulation ($f_{\max} = 5\,\mathrm{MHz}$) the shortest wavelength in the domain is $\lambda_{\min} = 0.2\,\mathrm{mm}$ and is sampled by 20 nodes of the mesh. The time step is $\Delta t = 0.003\,\mu\mathrm{s}$ which satisfies the stability condition (4.2), and the simulation runs over 16384 steps taking approximately $49\,\mu\mathrm{s}$. All these parameters for the FDTD simulation are gathered in the following table.

Frequency range	Discretization	Physical domain	Computational domain
$0-5\,\mathrm{MHz}$	$\Delta x = 0.01\,\mathrm{mm}$	$L = 4\,200$ cells (X)	$L = 42\,\mathrm{mm}$
$\lambda_{\min} = \dfrac{c_{\min}}{f_{\max}} = 20\Delta x$	$\Delta y = 0.01\,\mathrm{mm}$	$l = 200$ cells (Y)	$l = 2\,\mathrm{mm}$
	$\Delta t = 0.003\,\mu\mathrm{s}$	16 384 time steps	running time $49\,\mu\mathrm{s}$

Table 5.1 *Parameters of the FDTD simulation for SH waves in the bilayered plate (5.1)*

Traction-free condition ($\sigma_{23} = 0$) is set at the top and the bottom of the domain, and PML are added at both lateral edges for modeling an infinite plate. The punctual source is located at the top free surface near the left edge of the computational domain. The computational domain and the duration of the simulation are large enough for the formation of SH guided waves in space and time. Thereby, picking a collection of m signals $s_j(t)$ at m equidistant points along the surface we create a 2D-array $s_j(t_i)$, $i = 1..n$ and $j = 1..m$. The surface response data obtained in space and time is then subjected to the 2D-FFT calculation (see §4.3.3) to find the wave amplitude distribution in (ω,k)-domain. This amplitude spectrum, visualized as an intensity picture, is shown in Fig. 5.1.

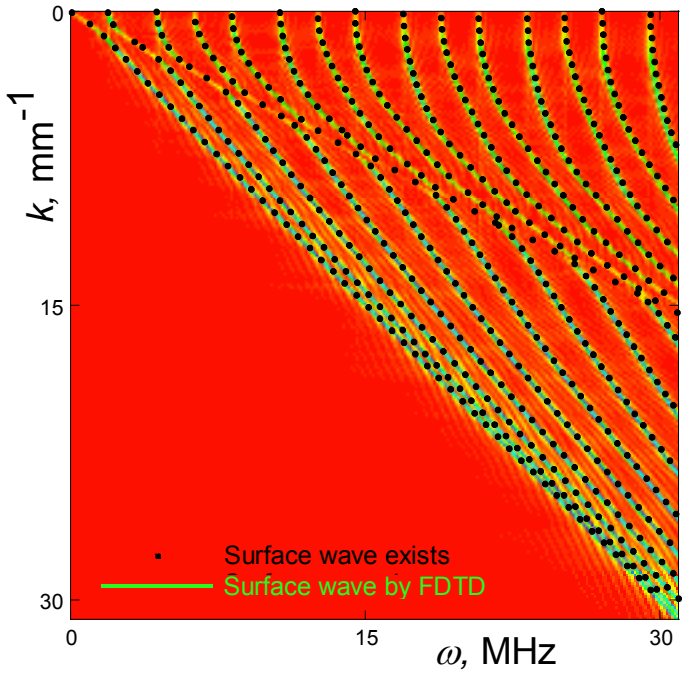

Fig. 5.1 *Dispersion curves for SH waves for the bilayered plate (5.1). The dotted-lines represent the theoretical dispersion curves calculated from the dispersion equation (2.16). The intensity picture in the background displays the amplitude spectrum at the top surface of the plate.*

The numerical results are superposed in Fig. 5.1 with the analytically predicted dispersion curves (see Chapter 2). A very good correspondence between both sets of data is observed.

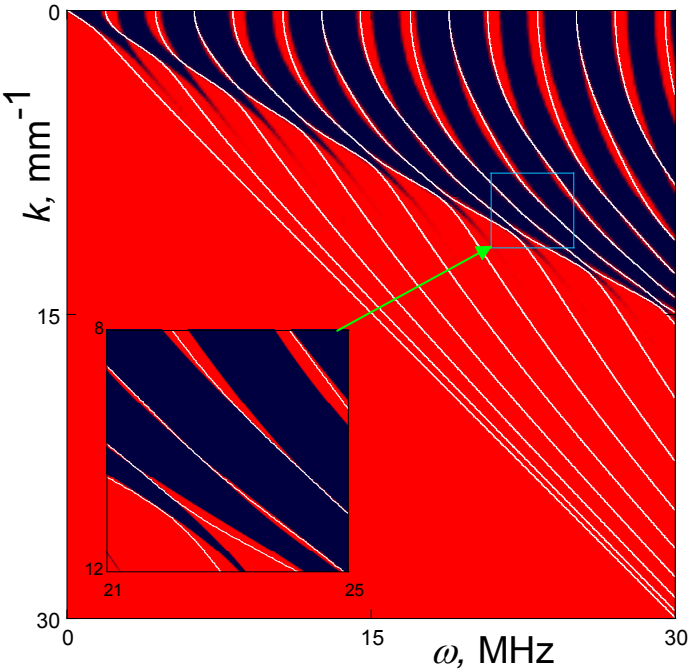

Fig. 5.2 *The dispersion curves for the bilayered plate (white continuous lines) of Fig. 5.1, overlaid onto the Floquet passbands (dark zones) and stopbands (gray zones) of an infinite periodic structure with the given bilayer as a unit cell.*

5.3 SH surface waves in a periodic halfspace

We now pass to the case of the SH surface waves (SHSW) in periodic halfspaces whose material properties are either continuously varying or piecewise constant through the depth. By means of the FDTD technique, we will obtain the numerical results and compare them with the analytical predictions of Chapter 2.

5.3.1 Continuously inhomogeneous unit cell

We consider a periodically inhomogeneous isotropic halfspace $y \geq 0$ with a traction-free surface at $y = 0$. To highlight the principal features in question, we confine to the same as in Section 2.4.3 example of constant mass density and a linearly decreasing profile of the velocity $c_t(y) = \sqrt{c_{44}(y)/\rho}$:

$$\rho = 1\,\mathrm{g/mm^3}; \quad c_t(y) = c_t(0)(2 - \frac{y - nT}{T}) \text{ for } 0 \leq y \leq T \qquad (5.3),$$

with $c_t(0) = 1\,\mathrm{mm}/\mu\mathrm{s}$, $T = 2\,\mathrm{mm}$, where n is the label of the cell (starting at $n = 0$ for the top layer) and T is the (least) period.

The numerical procedure is as follows. The source in this FDTD simulation is the same as for the case presented in the Section 5.2. The configuration has been chosen in accordance with the fact that the surface waves are localized near the surface of a halfspace and hence a finite number of layers in the simulation is sufficient. The tests have shown that a numerical domain modeling the six upper periods generally enables us to well capture the depth dependence. At the same time, the length of this domain along the *X*-axis and the running time of the simulation should be sufficiently large to enable probing the surface response far enough from the source where the contribution of the bulk waves in comparison to that of surface waves is negligible. The parameters of the FDTD simulation recapitulated in Table 5.2 have been finally chosen as a good compromise between the above requirements on the size of computational domain and a reasonable running time of computation. The PMLs were added at both side edges of the simulation domain and below the sixth period of the stack for emulating the infinite halfspace.

Frequency range	Discretization	Physical domain	Computational domain

$0-5\,\mathrm{MHz}$ $\lambda_{\min}=\dfrac{c_{\min}}{f_{\max}}=20\Delta x$	$\Delta x=0.01\,\mathrm{mm}$ $\Delta y=0.01\,\mathrm{mm}$ $\Delta t=0.003\,\mu\mathrm{s}$	$L=4\,800$ cells (X) $l=1\,200$ cells (Y) $16\,384$ time steps	$L=48\,\mathrm{mm}$ $l=12\,\mathrm{mm}$ running time $49\,\mu\mathrm{s}$

Table 5.2 *Parameters of the FDTD simulation for SHSW in a continuously periodic halfspace with the unit-cell profiles (5.3) and (5.4).*

The transient wave field probed at the surface was Fourier transformed by applying 2D-FFT (the same algorithm as described above for the case of the bilayered plate) in order to generate the intensity pictures of the surface response in the (ω,k)-domain and thereby to visualize the dispersion spectrum. For a good resolution of these pictures (see Section 4.3.4), we were picking up signals uniformly over a long distance along the surface, with skipping some nodes in space and time. Specifically, the 2D-matrix data were built over space and time by probing the wave field one node over five along the surface and one node over eight in time. A good spectral resolution is therefore ensured in the (ω,k)-domain which we are interested in, while the amount of data to process has been drastically reduced. With such a procedure, the pictures are much neater and the trajectories of the dispersion curves are much more discernible.

Fig. 5.3 compares the results of the post-signal processing of the FDTD-simulated wave with the analytically predicted dispersion curves. A good correspondence between both spectra is observed. We recall that the dispersion branches of the physical SHSW in the periodic halfspace represent certain spectral ranges of the branches of the SH waves in the free plate comprising a single unit cell. One can see that the intensity spectrum of the SHSW amplitudes reveals correctly the locus where the SHSW-existence was theoretically predicted. An artifact slightly seen on the second branch is due to the fact that only six periods have been modeled in the numerical emulation of the halfspace. Increasing the number of layers in the simulation eliminates this artifact.

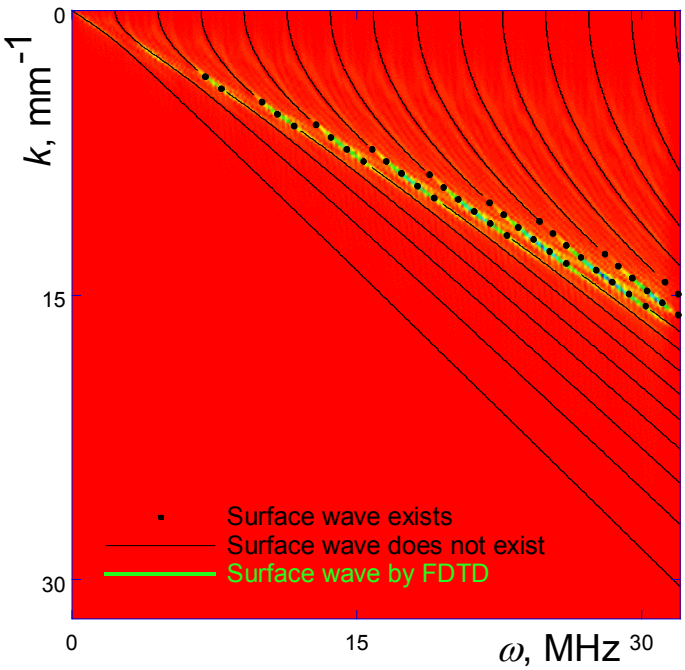

Fig. 5.3 *The intensity picture of the FDTD-simulated wave field superposed on the analytically predicted dispersion curves for SHSW in the periodic halfspace with the unit-cell profile (5.3).*

Let us now see what happens in the inverse to (5.3) case of the velocity profile

$$\rho = 1\,\mathrm{g/mm^3}\ c_t(y) = c_t(0)\left(1 + \frac{y - nT}{T}\right) \text{ for } 0 \le y \le T \tag{5.4}$$

(the values $\rho = 1\,\mathrm{g/mm^3}$, $c_t(0) = 1\,\mathrm{mm}/\mu\mathrm{s}$ and $T = 2\,\mathrm{mm}$ are kept intact), which implies turning the unit cell (5.3) 'upside down'. According to the reciprocity property (see §2.5.1), the replacement of (5.3) by (5.4) does not affect the 'guiding' dispersion curves related to a single unit cell with free boundaries, but the SHSW for the profile (5.4) exist precisely where they do not exist (as non-physical) for the profile (5.3) and vice versa. Moreover, in the case of monotonic profiles (which is the case in hand) the velocity window (spectral corridor on the $\{\omega, k\}$-plane) of the SHSW existence (or their non-existence for the inverse profile) lies within the asymptotically constant velocity bounds $c_1 \lessapprox \omega / k \lessapprox c_2$ (see §2.5.3). These bounds can be estimated by a simple and general formula (2.32), involving only the values of $\rho(y)$ and $c_t(y)$ at the unit-cell edges $y = 0, T$. For the present case where density is constant, Eq. (2.32) simplifies to

$$c_1 \lessapprox \max\left\{c_t(0), c_t(T)\right\},\ c_2 \approx \sqrt{c_t^2(0) + c_t^2(T)}. \tag{5.5}$$

Fig. 5.4 displays the numerical and analytical data for the profile (5.4) inverse to (5.3). Comparing Figs. 5.3 and 5.4 corroborates the reciprocity property.

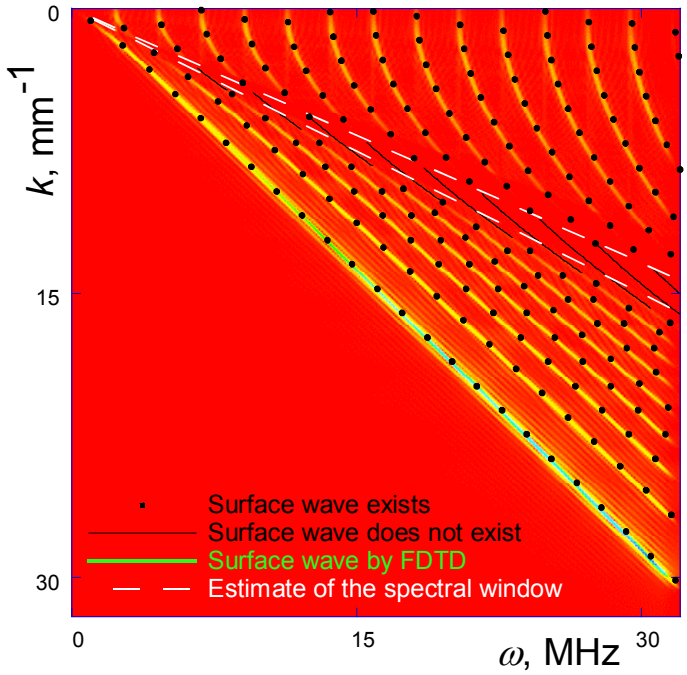

Fig. 5.4 *The same display of numerical and analytical data as in Fig. 5.3 but for the inverted unit-cell profile (5.4). The spectral corridor (5.5) of SHSW non-existence is indicated by white dashed lines.*

Next, with a view of confirming the consistency of our surface-wave modeling, we will examine the modal shape of SHSW through the depth. The velocity profile (5.4) is taken, and the same source as in the previous cases is used. In order to resolve the mode shapes, the simulated physical domain now includes more unit cells (20 periods) and has a lesser distance along the free surface than before. The parameters of this simulation are given in Table 5.3.

Frequency range	Discretization	Physical domain	Computational domain
$0-5\,\mathrm{MHz}$	$\Delta x = 0.01\,\mathrm{mm}$	$L = 800$ cells (X)	$L = 8\,\mathrm{mm}$
$\lambda_{\min} = \dfrac{c_{\min}}{f_{\max}} = 20\Delta x$	$\Delta y = 0.01\,\mathrm{mm}$	$l = 4\,000$ cells (Y)	$l = 40\,\mathrm{mm}$
	$\Delta t = 0.003\,\mu\mathrm{s}$	32 768 time steps	running time $98\,\mu\mathrm{s}$

Table 5.3 *Parameters of the FDTD simulation used for recovering the modal shape of SHSW.*

The simulation time is chosen quite long to allow principal wave front emitted by the source to reach the edges of the computational domain and to disappear within the PML. Once it is gone, we observe the wave field produced by reflections and transmissions at the interfaces of unit cells which forms the surface waves. As an example, Fig. 5.5 shows the depth distribution of the particle velocity $v_3(x,y,t)$ at the time $t = 81\,\mu\mathrm{s}$ and the distance x=$5.5\,\mathrm{mm}$ away from the source.

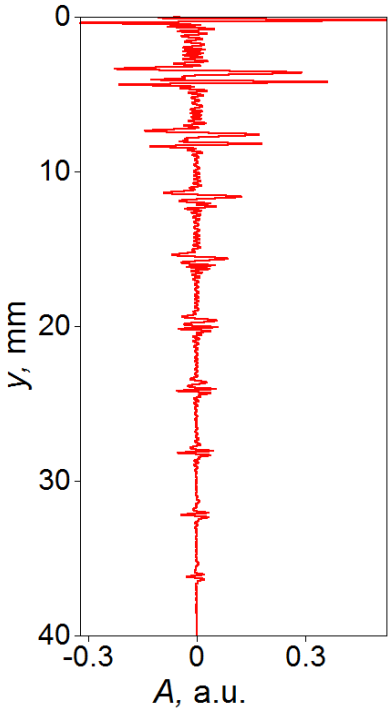

Fig. 5.5 *Dependence of the FDTD-simulated particle velocity* v_3 *on the depth coordinate* y *at* $t = 81\,\mu\text{s}$ *and* $x = 5.5\,\text{mm}$.

Transient wave field decaying into the depth corresponds in general to the superposition of several surface modes. In order to numerically recover the damping coefficient $K'' \equiv \operatorname{Im} K(\omega, k)$ of the Floquet modes, the space-time wave field must first be Fourier-transformed over the horizontal coordinate x and over time, thus switching from the (x,t)-domain to the (ω,k)-domain of the dispersion curves. This is performed by applying the 2D-FFT: $v_3(t,x,y) \rightarrow v_3(\omega,k,y)$, which yields the wave field in the Fourier domain (ω,k) as a continuous function of the physical coordinate y. The obtained Fourier-transformed wave field $v_3(\omega_0,k_0,y)$ taken at a point (ω_0,k_0) of the SHSW-dispersion curve (which lies in the *m*-th stopband where $K' \equiv \operatorname{Re} K = 0,\pi$ for even and odd *m*, respectively) has the *y*-dependence of the form

$$v_3(\omega_0,k_0,y) = (-1)^m V(y) \exp\left[-K''y\right] \quad \text{with} \quad V(y) = V(y+nT) \tag{5.6}$$

Thus, the second step is to probe this dependence with a period T which enables us to extract the sought coefficient K''. Generally speaking, it suffices to compare the values of $v_3(\omega_0,k_0,y)$ at any two points y separated by an integer number of periods T. However, rather than confining to only two probe points, a more stable output can be achieved by picking up a discrete set of magnitudes of the wave field $\left|v_3(\omega_0,k_0,y)\right|$ at $y = 0,T,2T,\cdots,nT$

and, after normalization by $\left|v_3\left(\omega_0,k_0,0\right)\right|$, fitting them to the dependence $\exp(-K''y)$ which follows from (5.6).

Consider the implementation of this procedure. The mode at the spectral point $(\omega_0,k_0)=(20.39,0.98)$ along the 9-th branch is chosen. The profile $v_3\left(\omega_0,k_0,y\right)$ obtained after FDTD simulation and 2D-FFT process, provides the set of 21 values of the magnitudes $\left|v_3^{(n)}\right|=\left|v_3^{(n)}\left(\omega_0,k_0,y_n\right)\right|$ at the $y_n=nT$ located at the interfaces between the unit cells. Fitting this set $\left|v_3^{(n)}\right|$ normalized by $\left|v_3^{(0)}\right|$ to the function $\exp(-K''y)$ yields the damping factor $K''=0.35\,mm^{-1}$ for the SHSW mode at (ω_0,k_0), see Fig. 5.6. The analytical value of K'' is defined by the formula $K''=-T^{-1}\ln|q|$, where $q(\omega,k)$ is the eigenvalue of the propagator **M**(T,0) discussed in Chapter 2. Substituting $(\omega_0,k_0)=(20.39,0.98)$ in Eq. (2.9) yields $q=-1.414$ and hence $K''=0.346\ \mathrm{mm}^{-1}$. This is perfectly close to the above value extracted from the simulation.

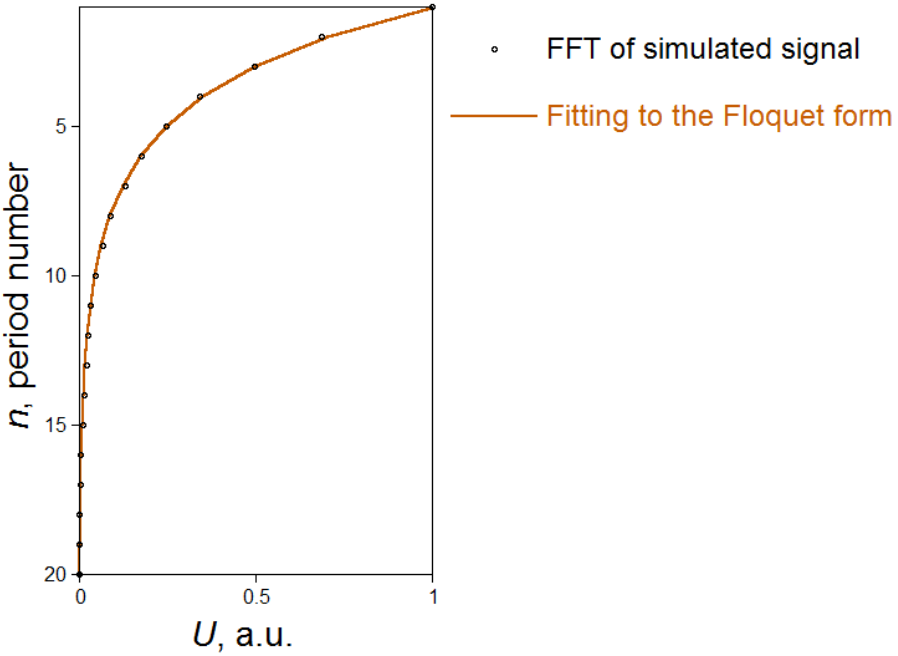

Fig. 5.6 *Depth dependence of the particle velocity* $\left|v_3\left(\omega_0,k_0,y_n\right)\right|$ *of the SHSW mode, extracted from FDTD simulation at* $(\omega_0,k_0)=(20.39,0.98)$, *and its fitting to the Floquet form* $\exp(-K''y)$ *with* $K''=0.35\ \mathrm{mm}^{-1}$.

5.3.2 Piecewise homogeneous unit cell

We now consider a periodic halfspace with the piecewise homogeneous unit cell. Let it be composed of two equidistant layers with the material parameters as in (5.1), namely,

$$\rho_1=\rho_2=1\,\mathrm{g/cm}^3,\ c_{t1}=2\,\mathrm{mm}/\mu\mathrm{s},\ c_{t2}=1\,\mathrm{mm}/\mu\mathrm{s},\ T=2\,\mathrm{mm}, \tag{5.7}$$

where the subscript 1 and 2 indicate the upper and lower layers respectively (this matters for the case of a halfspace). Note that any bilayered piecewise homogeneous unit cell obviously falls under the case of a (discretely) monotonic unit-cell profile discussed in Chapter 2. In particular, since the profile (5.7) implies that both the shear-wave velocity c_t and the impedance ρc_t decrease into the depth within the unit cell, the SHSW in a periodic halfspace with such unit cell must exist in a narrow spectral range of velocity ω / k only and not exist elsewhere (see Section 2.5.2). The bounds of this spectral range are given by the same equation (5.5) as in the case of a continuously inhomogeneous unit cell, except that the lower bound and its evaluation become exact. Thus

$$c_1 \le \omega / k \lessapprox c_2 \text{, where } c_1 \lessapprox \max\left\{c_{t1}, c_{t2}\right\},\ c_2 \approx \sqrt{c_{t1}^2 + c_{t2}^2} \tag{5.8}$$

The numerical simulation uses the source (5.2) and is performed with the parameters presented in Table 5.4

Frequency range	Discretization	Physical domain	Computational domain
$0 - 5\,\mathrm{MHz}$	$\Delta x = 0.01\,\mathrm{mm}$	$L = 4\,200$ cells (X)	$L = 42\,\mathrm{mm}$
$\lambda_{\min} = \dfrac{c_{\min}}{f_{\max}} = 20\Delta x$	$\Delta y = 0.01\,\mathrm{mm}$	$l = 1\,200$ cells (Y)	$l = 12\,\mathrm{mm}$
	$\Delta t = 0.003\,\mu\mathrm{s}$	$16\,384$ time steps	running time $49\,\mu\mathrm{s}$

Table 5.4 *Parameters of the FDTD simulation for SHSW waves in the periodic halfspace with a piecewise homogeneous bilayered unit cell.*

Fig. 5.7 displays the spectral intensity picture generated from the 2D-FFT process on the surface response of the halfspace. The numerical data are superimposed on the analytically predicted dispersion curves. Like in Fig. 5.3, it is clearly seen that only a small 'noise' wave field is observed beyond the spectral window (5.8). It is due to the fact that the simulation cannot emulate perfectly the actual infinite halfspace when surface waves are supersonic with respect to the SH-wave speeds in the bilayer (bulk partial waves in both layers).

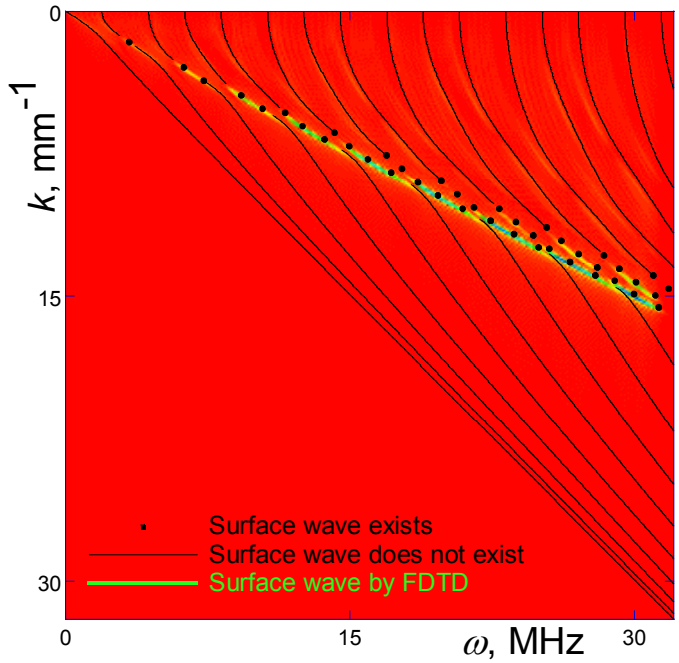

Fig. 5.7 *The intensity picture of the FDTD-simulated wave field superposed on the analytically predicted dispersion curves for SHSW in the periodic piecewise homogeneous halfspace with the unit-cell profile (5.7).*

The results for the inverse to (5.7) case of the unit cell with discretely increasing c_t and ρc_t:

$$\rho_1 = \rho_2 = 1\,\mathrm{g/cm^3}\,,\ c_{t1} = 1\,\mathrm{mm/\mu s}\,,\ c_{t2} = 2\,\mathrm{mm/\mu s} \tag{5.9}$$

are presented in Fig. 5.8. As expected, the spectral zones of the SHSW existence and non-existence swap with respect to Fig. 5.7.

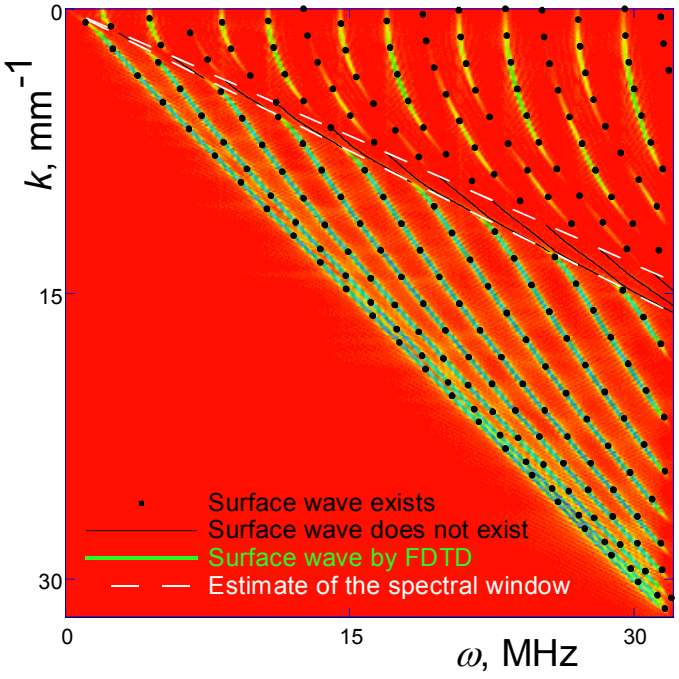

Fig. 5.8 *The same display of numerical and analytical data as in Fig. 5.7 but for the inverted unit-cell profile (5.9). The spectral corridor (5.8) of SHSW non-existence is indicated by white dashedlines.*

5.4 SH surface waves in a periodic semi-infinite strip

Let us now consider the case of a semi-infinite periodic strip with the traction-free edge and side faces which was described in Section 2.6. In this case, the SHSW are understood as surface waves in the sense that they are localized at the strip edge. Accordingly, the axis *Y* is directed along the strip. We choose the profile of the unit cell to be continuously inhomogeneous as in (5.4). The punctual source at the surface of the strip is taken in the same form as in (5.2) but with the factor 10π replaced by 8π in order to decrease the maximum frequency $f_{\max}$ in the spectrum of the source, which in turn decreases the calculation time and memory. The FDTD scheme is implemented for 10 periodic unit cells. The parameters of the FDTD simulation are given in Table 5.5.

Frequency range	Discretization	Physical domain	Computational domain
$0-4$ MHz	$\Delta x = 0.0125$ mm	$L = d = 600$ cells (X)	$L = 7.5$ mm
$\lambda_{\min} = \dfrac{c_{\min}}{f_{\max}} = 20\Delta x$	$\Delta y = 0.0125$ mm	$l = 1600$ cells (Y)	$l = 20$ mm
	$\Delta t = 0.004\ \mu$s	32 768 time steps	running time 131 μs

Table 5.5 *Parameters of the FDTD simulation for SHSW in a periodic semi-infinite strip with the unit-cell profile(5.4).*

Traction-free conditions are applied at the top, left and right of the computational domain, and PMLs are added at the bottom of the domain in order to model a semi-infinite strip. The duration of the simulation is chosen long enough in order to allow the resonance to develop and to get rid of the transient part preceding the steady state. These measures are prerequisite to visualizing the discretization (2.40) of dispersion curves along the k-axis. Besides, the width d of the strip (the length of computational domain along *X*) must not be too large, since otherwise the interval between two successive wavenumbers of the strip resonances $\Delta k_x^{(n)} = k_x^{(n)} - k_x^{(n-1)} = \pi / d$ will be too small and hence the discretization will be hardly discernible with account of the resolution of the intensity picture itself, which in turn is determined by the length of the actual probed zone. By default, the resolution in k of the intensity picture is $\Delta k = 2\pi / L$ that at *L=d* is twice greater than $\Delta k_x^{(n)}$ of the strip. In order to increase the intensity picture resolution (i.e. to decrease Δk and $\Delta\omega$) we have performed

the zero-padding technique (see Section 4.3.4) over spatial and temporal data. This also allows us to avoid signal probing at each node of the mesh along the surface; instead the data used for plotting Fig. 5.9 were picked up periodically at one point over four along the surface and at one point over sixteen in time. As a result, the resolution of the intensity picture displayed in Fig. 5.9 is $\Delta k \approx 0.12\,\mathrm{mm}^{-1}$, which is four times smaller than it would be provided Δk obtained from the raw data. Due to this procedure, Fig. 5.9 clearly reveals the resonances of the strip.

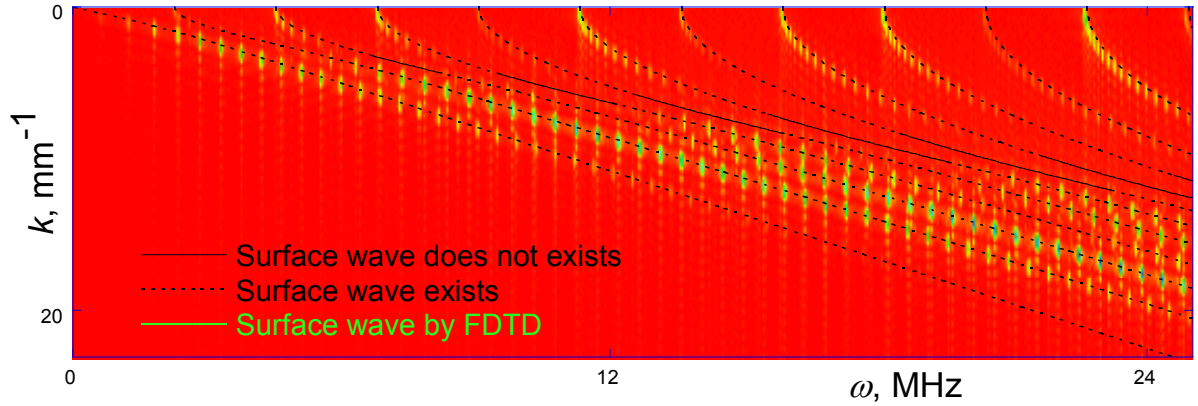

Fig. 5.9 *The intensity picture of the FDTD-simulated wave field superposed on the analytically predicted dispersion curves for SHSW in the periodic semi-infinite strip with the unit-cell profile (5.4).*

Moreover, in order to quantify the correspondence between the numerical data and the analytical predictions, the picture was additionally magnified by applying 2D-FFT with zero-padding over 16384 points on x, which enables a much higher resolution on k equal to $\Delta k \approx 0.01023$. Using this data processing, the average distance between six successive spots in the intensity picture (three of them are shown in the Fig. 5.10) has been evaluated as $l = 0.426$. This value corresponds quite well to the analytically predicted value $l = \pi / d = \pi / 7.5 \approx 0.419\,\mathrm{mm}^{-1}$. The relative error, which is less than 2%, is close to the above-mentioned resolution on k ($\Delta k \approx 0.01023$).

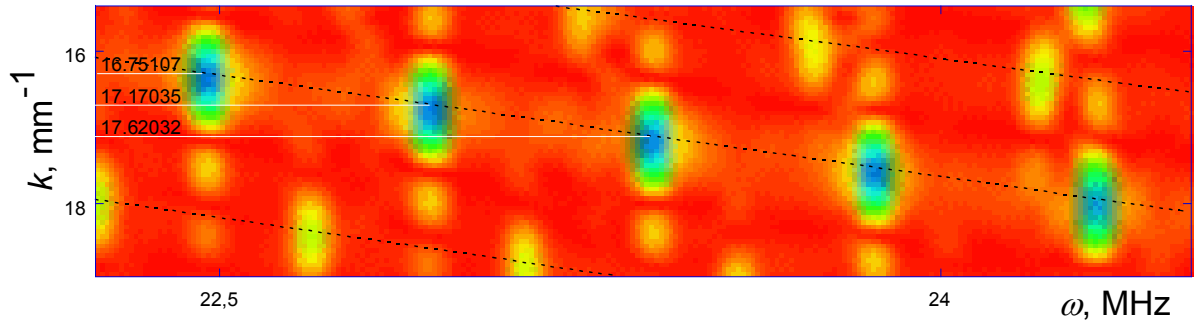

Fig. 5.10 *Magnified intensity picture of Fig. 5.9 for evaluating the k-distance between two neighbouring resonances.*

5.5 Remark on the accuracy of high-frequency numerical calculations

It may be noticed from all intensity pictures that the maximums of magnitudes at high frequencies have a slight frequency shift with respect to the analytical predictions. This is mainly due to the numerical dispersion of the FDTD scheme caused by a lack of precision in the resolution of the least wavelengths in the scheme. For illuminating this issue, we have repeated one of the simulations (namely, the one corresponding to Fig. 5.4), where we deliberately took the least wavelength resolved with only 7.5 points (instead of the 20 points as before, see Table 5.3). The parameters of the mesh are then $\Delta x = \Delta y = 0.025\,\mathrm{mm}$ and $\Delta t = 0.0075\,\mu\mathrm{s}$ (cf. Table 5.3). The spectrum obtained from this simulation is presented in Fig. 5.11.

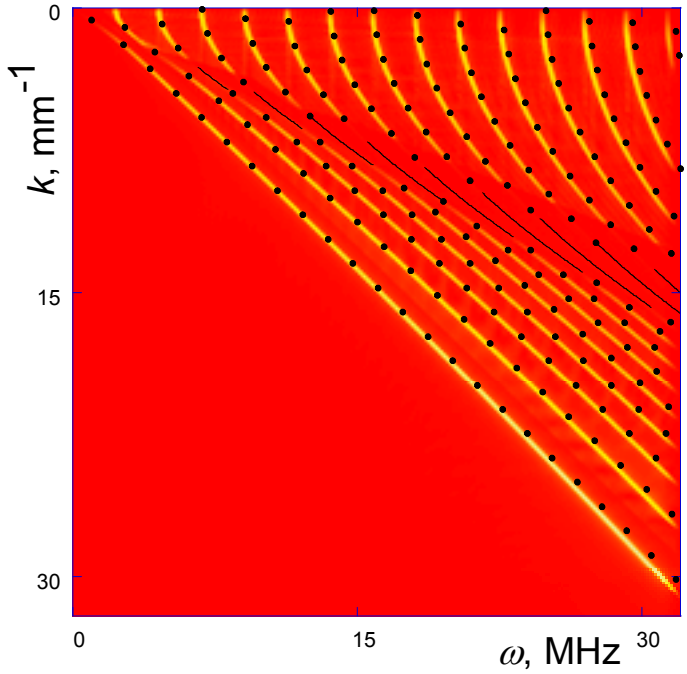

Fig. 5.11 *The dispersion spectrum of Fig. 5.4 recalculated by means of the mesh with a poorer high-frequency resolution.*

It is seen that the ridges in the intensity picture deviate at high frequencies from the theoretical predictions (black points on the plot). At the same time, it is noted that refining a mesh for the sake of the better high-frequency resolution may lead to a drastic increase of the computational domain. In this regard, a sampling rate of 20 points per least wavelength that was used in this work is a good compromise between the accuracy and the computing resources requirements.

5.6 Conclusion

In this Chapter, we have presented the application of the FDTD scheme for analyzing the SH-wave propagation in vertically periodic structures. The spectral data extracted from the FDTD simulations was compared to the analytical predictions of Chapter 2. We have numerically verified two significant properties of the SH surface waves (SHSW) in a periodic halfspace with continuously or discretely monotonic unit cell, namely, the reciprocity property and the fact that there is a single spectral window where the SHSW exist if the unit-cell profile is decreasing and where SHSW do not exist if the profile increasing. We confirmed the surface localization of the SHSW by visualizing the exponential decay of the amplitude in the physical (space-time) domain, and obtained a perfect agreement between the numerical and analytical values of the decay coefficient. The FDTD simulations were also implemented for a periodic semi-infinite strip and a similar cross-verification of the numerical and analytical results was achieved.

6 Application of the FDTD method to a multiple scattering problem

Table of Contents

6.1 Introduction

In the preceding chapter, we have described numerical experiments performed by means of FDTD simulations of wave propagation in deterministic configurations of multilayered structures. Since the theoretical results were obtained from exact calculations and so long as the numerical scheme was accurate enough, there was no particular reason for having a large discrepancy between the numerical experiments and the analytical data coming from elastodynamics theory. The FDTD technique was just a numerical way of solving a 'well-stated' problem of elastodynamics. In the present chapter we propose to exploit the FDTD numerical simulations for drastically different kind of wave-propagation problems: we aim at using FDTD for the study of waves propagating in a randomly distributed population of scatterers [1, 2] . Due to the non-deterministic character of the problem, it does not admit any exact and closed-form solutions. The most usual way for tackling such a problem is to describe the wave propagation in terms of coherent wave field (or mean wave) and non-coherent field (random part) [3]. This (formal) splitting of the sought full wave solution enables us to extract the statistical mean field. This latter field is defined on the basis of configurational averaging of the scatterers while the incoherent field is supposed to disappear under the configurational average [1]. To the mean wave are attached the notions of phase velocity and exponential attenuation and consequently the concept of effective medium which allows a description of the actual medium as an equivalent homogeneous medium whose dispersive properties take into account the statistical properties of the original inhomogeneous medium. It is therefore natural to describe the coherent part through a wave equation (of Helmholtz type) [1, 3] while the incoherent field is usually modelled by a diffusion equation [3]. (In this thesis we will be interested in the coherent-wave propagation only.) The purpose of the multiple scattering theory (MST) is to determine analytically the effective wavenumber [1, 3, 4] along with material parameters such as the dynamical mass density and elastic coefficients [5-8], of the mean waves propagating in inhomogeneous media constituted of a (generally uniform) random distribution of scatterers.

In this chapter, the goal is to make use of numerical experiments by FDTD in the same conceptual framework than that of MST, which means recovering numerically some properties of the coherent-wave propagation, e.g. the reflection/transmission spectra of inhomogeneous slab, and to compare them to the results stemming from some MST

techniques. To access those configurational-averaged properties by means of the FDTD which is a deterministic numerical tool, it will be necessary to proceed to a series of simulations over different samples of random distributions of scatterers [9] and then to sum up the space and time wave fields of each material configuration. In practice, at least in this work, less than a hundred of simulations will be sufficient for obtaining convergence to stable mean fields. A similar kind of procedure has been developed in the works of [9] (our approach is though slightly different).

In the beginning of this chapter we will present the basic notions concerning the effective properties of inhomogeneous media formed by spatially uniform random distribution of identical scatterers embedded into a solid matrix. The 2D configurations studied in this work describe the propagation within micro-cracked media and scattering by a random distribution of solid cylinders within a solid matrix. The complex effective wavenumber [4] and the dynamical effective mechanical properties of the equivalent homogeneous media [10] (namely, the dispersive mass density and the dispersive elastic constants) allow one to obtain the reflection and transmission spectra of the coherent wave through an inhomogeneous slab. These theoretical reflection/transmission spectra based on the effective properties will be taken from the literature [4, 11]. The objective is to compare them to the spectra obtained by numerical FDTD simulations performed over several samples of disorder.

Several practical cases of scattering and multiple scattering will be shown. First, we will consider scattering by only one object (flat crack and cylindrical inclusion subjected to normal and oblique incidence) in order to gauge our FDTD numerical code against exact analytical results. This will allow us to quantify the ability of the FDTD to recover numerically the scattering characteristics of a single inclusion before performing simulations in the multiple scattering context. The first set of 2D configurations dealt with in this work is the SH-wave propagation through a spatially uniform micro-cracked slab, for which we will explore the impact of the slab thickness, of the volume fraction of inclusions and of the angle of incidence of the incident plane wave. Also some numerical experiments will be implemented for the particular case of a continuous profile of volume fraction of scatterers through the thickness of the slab [12, 13]. The second set of multiple scattering problems concerns the propagation of longitudinal and transverse waves through a random slab of solid cylinders embedded into a solid matrix [3, 14]. The aim of this latter configuration is to extend the previous

observations to a coupled-waves system (P and SV waves) within the actual inhomogeneous media. The practical issue of the definition of the thickness of a random slab containing finite-volume scatterers will also be approached.

6.2 Multiple scattering and effective media

This section intends to remind the basic results that can be obtained from the multiple scattering theory (MST). The primary wave characteristics of interest provided by the MST is a complex-valued effective wavenumber that describes the propagation of the coherent wave in a random medium [1, 15-17] . It is not the purpose of this work to present the details of the techniques of multiple scattering. We will just introduce the concept of dispersive mechanical properties of the equivalent homogeneous media as defined in the framework of the MST [5, 6]. These quantities will be used in the subsequent sections as benchmarks for comparison with the results of FDTD simulation.

Under the hypothesis of the existence of coherent wave regime of propagation (often implying relatively small volume fractions of scatterers and reasonably low ka frequency regimes), it is possible to define an equivalent homogeneous medium which relies directly upon the properties of the coherent wave. Using the MST yields the effective wavenumber and the dispersive effective impedance, which in turn can be used to determine the dispersive effective mass density and dispersive effective mechanical moduli. These equivalent mechanical properties of the inhomogeneous medium can then be used as 'simple' inputs in standard reflection/transmission problems for which the medium is now seen/described as an homogeneous material. Note that the equivalent properties are modelled on the basis of only the coherent part of the wave field, leaving aside the incoherent wave motion.

6.2.1 The effective wavenumber provided by Waterman and Truell (W&T)

Waterman and Truell [15] have established a formalism for deriving an explicit form of the effective wavenumber K of the coherent wave propagating in a random medium composed of a uniform distribution of scatterers dispersed in an homogeneous and isotropic matrix. For the 2D case (the inclusions extend to infinity in the third dimension), this explicit form is given by

$$\frac{K^2}{k_0^2} = \left[1 - \frac{2\mathrm{i}n_0}{k_0^2} f(0)\right]^2 - \left[\frac{2\mathrm{i}n_0}{k_0^2} f(\pi)\right]^2 \tag{6.1}$$

where k_0 is the wavenumber in the matrix, n_0 is the number density of inclusions (i.e. the number of objects per unit volume), $f(0)$ and $f(\pi)$ are the forward and backward scattering amplitudes of the scattered field. The function $f(\theta)$ is the angular form function defined by

$$f(\theta) = \sum_{n=-\infty}^{\infty} T_n e^{\mathrm{i}n\theta}\,, \tag{6.2}$$

where T_n are the modal scattering coefficients of the scatterers that depend on the frequency and on the inclusion properties (material parameters and geometry). Note that the volume fraction of scatterers is $\Phi = n_0 v$ where v is the volume of a single object. It is seen that the effective wavenumber derived by W&T depends only on the forward and backward scattering properties. The modal scattering coefficients are also specialized with respect to the problem to be solved: that is, if a longitudinal coherent plane wave is considered then the coefficients T_n are the modal coefficients of the scattered longitudinal wave field coming from the scattering of a longitudinal incident wave onto the scatterer (T_n^{P-P}), and in the case of a transverse wave the scattering coefficients are T_n^{SV-SV}.

6.2.2 Effective mechanical properties stemming from W&T results

Proceeding from the effective wavenumber (6.1) of W&T, Aristégui and Angel [5, 6] have developed the approach which enables one to define the effective dynamical impedance of a random slab. They have obtained the following expression which involves the effective wavenumber itself, the forward and backward scattering properties and the concentration of objects at the first order:

$$Z_{eff} = Z_0 \frac{k_0}{K}\left(1 - \frac{2in_0}{k_0^2}\left[f(0) - f(\pi)\right]\right), \tag{6.3}$$

where $Z_0 = \rho_0 c_0$ is the acoustic impedance of the matrix. Depending on the type of coherent waves considered (longitudinal or transverse waves), the value of Z_0 is either the impedance for longitudinal waves (P waves) or for transverse waves (SV waves polarized in the plane of propagation and SH waves polarized along the third dimension that is orthogonal to the plane of propagation).

6.2.3 The crack problem (line-like & finite-size cracks approaches)

For the comparisons concerning the cracked media, we have chosen two different theoretical techniques.

The first one is the direct application of the W&T formula (6.1) which is based on the amplitudes $f(0)$ and $f(\pi)$ of forward and backward scattering on cracks parallel to the plane incident front. Note that the W&T formalism, formally reduces the scatterers to points, which justifies the denomination of line-like cracks.

The second technique is a method which allows taking into account the actual size of the cracks, contrary to the technique employed by W&T. The details of this can be found in [4, 10]. Schematically, when the crack is represented as a line of discontinuity, the solution of the wave-crack scattering problem can be expressed in terms of a dislocation density b, which is a solution of a singular integral equation. For a crack of length $2a$ with a cross-section located along the segment ($y=0, |x| \le a$), the forward scattering amplitude $f(\theta)$ is defined in the *XY* plane by [14]

$$f(\theta) = \frac{\cot\theta}{2\pi} \int_{-a}^{a} b(x)\, \mathrm{e}^{-\mathrm{i}k_T x \sin\theta} \mathrm{d}x\,, \tag{6.4}$$

where θ represents the angle of propagation of the wave incident on the crack. In the following simulations, the cracks will be parallel to the slab faces and therefore the value of $f(\theta)$ will be taken at $\theta = 0$.

The two above approaches underlie estimations of the reflection and transmission coefficients of a slab of randomly distributed cracks, which will be used for comparison with the results of the FDTD numerical experiments.

6.2.4 The reflection/transmission coefficients of a slab

Assuming normal incidence of a plane wave on a slab of randomly distributed cracks, the theoretical values of the reflection and the transmission coefficients R and T of the coherent wave are [11]

$$\begin{aligned} R &= \frac{-Qe^{-\mathrm{i}k_0 d}}{1-Q^2 e^{2\mathrm{i}Kd}}\left(1-e^{2\mathrm{i}Kd}\right), \\ T &= \frac{1-Q^2}{1-Q^2 e^{2\mathrm{i}Kd}}\, e^{\mathrm{i}(K-k_0)d}, \end{aligned} \tag{6.5}$$

where

$$Q = \frac{Z_0 - Z_{eff}}{Z_0 + Z_{eff}}. \tag{6.6}$$

Therefore the coefficients R and T depend on all the parameters of the problem: on the frequency, on the material properties of the matrix, and on the material and geometrical properties of the scatterers. These theoretical values of R and T provided by the MST will be compared with the numerical data extracted from the simulations (the mean field).

6.3 SH wave scattering by a single obstacle

In this section we consider the case of SH field scattered by one obstacle. We will perform simulations of the normal and oblique SH plane wave scattered, first, by a crack and, second, by a cylindrical solid inclusion. The displacement field at a fixed location (in the forward scattering region) versus nondimensional frequency will be extracted and compared with the theoretical predictions. The aim of this preliminary study is to examine the accuracy of our numerical code in the case of scattering by a single object. The results should estimate the level of confidence for using the FDTD in the following multiple scattering numerical experiments which engage a multiple scattering process over many inclusions in the random slabs.

6.3.1 The case of normal incidence.

First we will consider scattering of SH plane wave by a single crack parallel to the wave front. The main task is to inspect reliability of FDTD for modelling the scattering at the tips of the crack, knowing that the (internal) boundary conditions for the flat part of the crack are those of a free surface (sliding contact between the two faces of the crack). Then the case of the scattering by a cylindrical inclusion will be treated. For each of these two cases, we will compare the FDTD and the theoretical evaluation of the particle velocity spectrum at a point whose distance from the center of the scatterer is equal to the size of the scatterer.

6.3.1.1 Flat-crack inclusion (sliding contact assumption)

We assume an isolated flat-crack of length $2a$ surrounded by a 2D isotropic homogeneous elastic medium with properties

$$\rho = 1\,g\,/\,cm^3, c_t = 1\,mm\,/\,\mu s\,, \tag{6.7}$$

where c_t is the speed of the out-of-plane polarized SH wave (propagation in the plane *XY* and polarization along *Z*). Let the crack be parallel to the *X*-axis and the normal to the crack be parallel to the *Y*-axis. The faces of the crack are supposed to satisfy the traction-free condition, that is, $\sigma \cdot \mathbf{n} = \mathbf{0}$ with $\mathbf{n}$ along *Y* (sliding contact assumption). The treatment of the crack in the FDTD scheme is described in Section 3.4.2. The numerical procedure is as follows: a transient plane wave is generated by using the initial condition setup in the numerical code above the crack, with a lateral extension along the *X*-axis over the entire computational domain including PMLs (see Section 4.2.4.3). We choose the following time function for the transient field:

$$s(t) = \cos\left(2\pi(t - t_0)\right)\exp\left(-(t - t_0)^2\right). \tag{6.8}$$

The frequency spectrum of this signal lies mainly within the frequency interval

$$0 \le f = \omega / 2\pi \le 2\,MHz\,. \tag{6.9}$$

The transient incident plane wave has therefore the function $s\left(t - \frac{1}{c_t} y\right)$ as a common factor for the wave-field components v_3 and σ_4 (σ_5 being null, as detailed in Chapter 4).

We choose $\Delta x = \Delta y = 0.025\,mm$ as dimensions for the FDTD cell in the numerical code and a computational domain of $\left(7.5\,mm, 15\,mm\right)$ which corresponds to a grid of 300×600 cells along *X* and *Y*, respectively[1]. The half-length of the crack is $a = 1\,mm$, which corresponds to 40 grid-cells of the rectangular mesh. At the highest frequency in the simulation ($f_{\max} = 2\,MHz$), the wavelength in the domain ($\lambda_{\min} = 0.5\,mm$) is sampled by 20 nodes. The time step $\Delta t = 0.014\,\mu s$ satisfies the stability condition (4.2) and the simulation runs over 4 096 steps of time (approximately $57\,\mu s$). The PMLs are added all around the computational domain for modelling an infinite medium. After the simulation is finished, the v_3-signal is picked up at the observation point $(0, 2a)$ relatively to the centre of the crack. By performing FFT of this signal and by dividing its spectrum by the incident-wave spectrum, we obtain the normalized amplitude spectrum versus the dimensionless frequency $ka = \frac{2\pi f}{c_t} a$. We compare these results coming from the numerical experiment with those calculated from analytical expressions. The latter technique resting on the boundary integral methods is described in [4, 18]. Figure 6.1 shows a very good agreement in between the FDTD results and the theoretical ones. It tells us that the FDTD technique rather accurately describes the

[1] The full set of parameters used for the FDTD will be displayed below in tables.

interaction of SH wave with a crack (especially with its tips) in the ka-range $[0,10]$, which is a reasonable range for studying multiple scattering in random media.

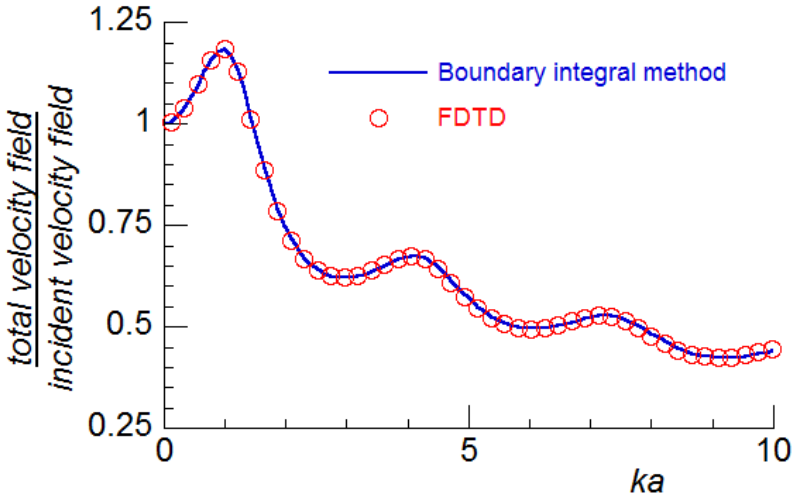

Fig. 6.1 *Normalised velocity field v_3 versus dimensionless frequency for a single crack of 2-mm length. The solid line presents the theoretical results; the empty circles present the numerical data extracted from the FDTD.*

6.3.1.2 Cylindrical inclusion

Let us now consider the SH-wave scattering by a filled cylinder. The main objective here is quantify the reliability of FDTD technique for tackling curved-shape objects while the FDTD-mesh is rectangular and uniform. The surrounding medium is isotropic and homogeneous with the same properties as in the flat-crack case. The cylindrical inclusion (2D circle inclusion) in the computational domain has the following material properties

$$\rho = 1\,g\,/\,cm^3, c_t = \sqrt{2}\,mm\,/\,\mu s\,. \tag{6.10}$$

The circle is arranged in the 2D Cartesian FDTD scheme according to the grid discretization. We need a sufficient spatial resolution of the mesh in order to decrease the geometrical description error caused by the mapping of the circle onto the rectangular grid. This is a systematic error but it can be reduced significantly by means of a refined grid. The following is a test in order to gauge as to how the FDTD can resolve the scattering by a circularly shaped object in a reasonable range of ka.

The numerical procedure is as follows. We generate a plane wave in the same way and with the same characteristics (6.8) and (6.9) as it has been done for the crack simulation in the previous section. We choose $\Delta x = \Delta y = 0.025\,mm$ as dimensions for the FDTD cell in the numerical code, and a computational domain of $\left(7.5\,mm, 20\,mm\right)$ which corresponds to a grid of 300×800 cells along *X* and *Y*, respectively. The radius of the inclusion is $a = 1\,mm$,

which corresponds to 40 grid-cells. At the highest frequency in the simulation ($f_{\max} = 2\,MHz$) the wavelength in the domain ($\lambda_{\min} = 0.5\,mm$) is sampled by 20 points. The time step $\Delta t = 0.007\,\mu s$ satisfies the stability condition (4.2) and the simulation runs over 4 096 steps (approximately $29\,\mu s$). The PMLs are added at the both edges and faces of the computational domain for modelling an infinite medium. After the simulation is finished we probe the wave-field at an offset $(0, 2a)$ relatively to the centre of the inclusion (below the inclusion in the forward scattering region). By performing FFT of this signal and by dividing it by the amplitude of the incident plane wave, we obtain the normalized amplitude of the scattered field at the probe-point (see Fig. 6.2). In the same plot we compare the numerically simulated scattered field with the exact calculation provided by the multipole expansion technique (cylindrical harmonics decomposition). A very good agreement is observed between the simulated and the theoretical results in the range $0 \le ka \le 10$, with a resolution of 80 cells covering the diameter of the cylindrical inclusion. Since the forthcoming numerical simulations of multiple scattering by a population of cylinders will be performed in the same ka-range, this latter result confirms the reliability of the FDTD technique using of a sufficiently refined mesh.

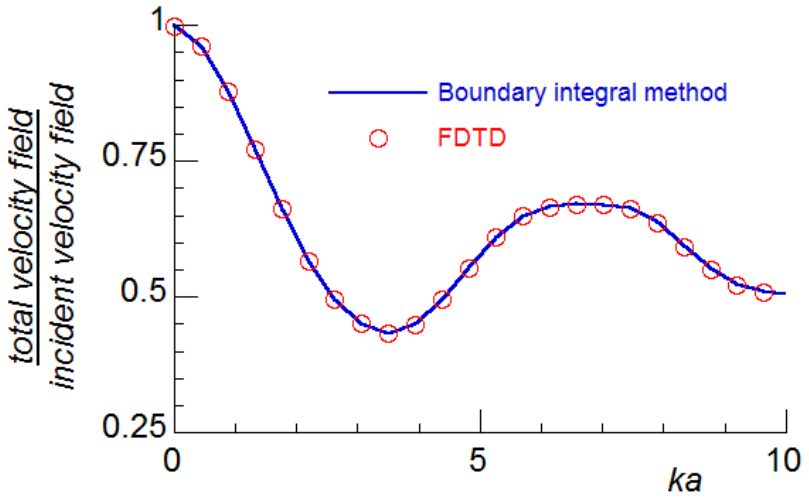

Fig. 6.2 *Velocity field (normalised by the incident field with normal incidence) in the forward scattering region versus nondimensional frequency for one cylindrical inclusion of 1 mm radius resolved by 80 cells through the diameter. The solid line presents the theoretical results; the empty circles present the numerical data extracted from the FDTD.*

6.3.2 The case of oblique incidence (the example of a single crack)

Another important issue is to examine accuracy of the numerical modelling of an oblique wave interacting with an object. We have seen that the simulations of normal incidence on either a crack or a cylindrical scatterer are relatively good so long as the scatterers are well resolved by the grid-mesh. In this section we will perform a simulation of a SH plane wave obliquely incident on a single 2D crack embedded into an isotropic homogeneous medium with the properties (6.7). We consider then a 2-D single crack.

The crack has a length $2a$ and lies along the X-axis of the mesh. The numerical procedure is as follows. We choose $\Delta x = \Delta y = 0.025\,mm$ as dimensions for the FDTD cell in the numerical code, and a computational domain of $\left(125\,mm, 0.25\,mm\right)$ which corresponds to a grid of $5\,000 \times 10$ cells along *X* and *Y*, respectively. The half-length of the crack is $a = 1\,mm$ which corresponds to 40 grid-cells. The origin of coordinates is placed at the point $\left(2500, 0\right)$. We excite the obliquely incident plane wave by using a line source with a phase delay as presented in Section 4.2.4.2. The horizontal line source is extended over the entire computational domain up to the PMLs and placed at the top of the computational domain just below the PML. We choose the time function for the source in the form (6.8) that is the same as it was for the normal incidence case.

The phase-delay source that will generate an oblique (conical) wave front is obtained by using a line source with a space-time dependence $s\left(\frac{\sin\theta}{c_t}x - t\right)$ where θ is the angle of incidence of the plane front onto the crack. For generating the front at 45°, the line-source distribution is chosen as:

$$s(x,t) = \cos\left(2\pi\left(\cos 45^\circ (x + 62.5) - t - 4\right)\right)\exp-\left(\cos 45^\circ (x + 62.5) - t - 4\ \right)^2 . \quad (6.11)$$

As explained in Chapter 4, modelling such a source requires spatial modulation of its amplitude in order to reduce the parasite effect coming from the edges. Therefore the function $s(x,t)$ is multiplied by the following function $M(x)$:

$$M(x) = H(37.5 - |x|) + H(|x| - 37.5)\exp-\left(\frac{|x| - 37.5|}{12.5}\right)^3 . \quad (6.12)$$

It yields transition zones of 1 000 cells at the ends of the constant amplitude zone such that the crack is located far enough from the zone of amplitude modulation, thus minimizing the perturbing effect (see Section 4.2.4.2). At the highest frequency in the simulation

($f_{\max} = 2\,MHz$), the wavelength in the domain ($\lambda_{\min} = 0.5\,mm$) is sampled by 20 points. The time step $\Delta t = 0.014\,\mu s$ satisfies the stability condition (4.2) and the simulation runs over 8 192 steps (approximately $115\,\mu s$). The PMLs are added at the both edges and faces of the computational domain for modelling an infinite medium. After the simulation is completed, we pick the time-signal for the component v_3 at the center of the lower face of the crack on the lower side. We perform another simulation, similar to the previous one, for which the crack is removed in order to extract the contribution of the incident field at the observation point. The normalized spectral amplitude of the component v_3 is shown in Fig. 6.3. A good agreement is observed between the simulated and the theoretical results. It confirms the consistency of the FDTD modelling for this problem.

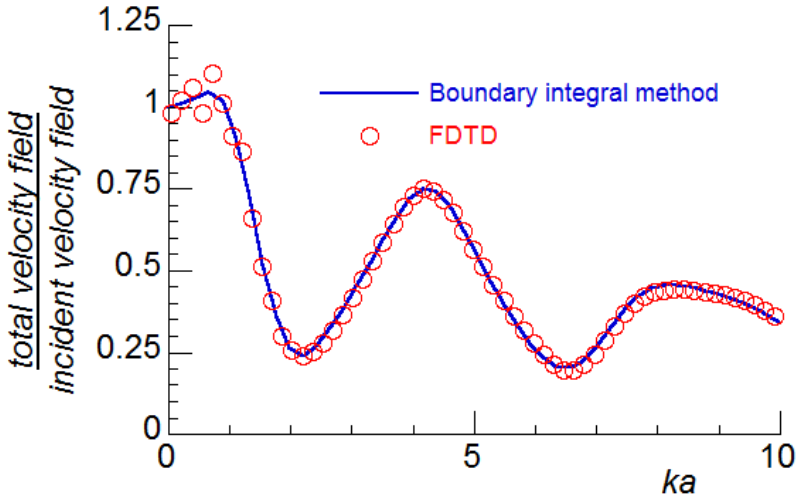

Fig. 6.3 *Velocity field (normalised by the incident field with normal incidence) versus nondimensional frequency for one cylindrical inclusion of 1 mm radius. The solid line presents the theoretical results; the empty circles present the numerical data extracted from the FDTD.*

6.4 SH-wave scattering by a slab of randomly distributed cracks

In this section we intend to compare some results concerning the reflectivity spectrum of a slab of flat cracks in the framework of coherent waves. Using the MST we can access the characteristics of coherent waves supported by the inhomogeneous slab such as the effective wavenumber $K_{eff}(\omega) = \frac{\omega}{c(\omega)} + \mathrm{i}\alpha(\omega)$ and the dynamical acoustic impedance $Z(\omega)$ or else , the effective mass density $\rho(\omega)$ and the dispersive effective shear modulus $\mu(\omega)$ of the equivalent homogeneous medium. Therefore the reflection $R(\omega)$ and transmission $T(\omega)$ coefficients of the inhomogeneous slab may be computed by solving a standard

reflection/transmission problem of an incident plane wave onto the equivalent homogenous layer emulating the actual layer containing the population of flat cracks.

A possible comparison between the theoretical and simulated wave characteristics could have been to run FDTD simulations over several realizations of the disorder of the random layer with a view to obtain the configurational mean field along the thickness of the slab and then to recover the complex value of the effective wavenumber K_{eff} within the slab by fitting the simulated field to a superposition of back and forth propagating effective plane waves. But we opt for comparing the results from the quantities which depend on the effective properties of the inhomogeneous slab and that can be evaluated from FDTD data picked up outside the slab itself. The reflection and transmission coefficients are then easily obtainable from the mean field (or coherent field) estimated on both side of the slab where the propagation medium is homogeneous. Therefore we propose to determine numerically $R(\omega)$ and $T(\omega)$ by means of a set of simulations by FDTD (configurational averaging), and to compare them with those stemming from the standard problem of reflection/transmission by an effective layer whose effective properties are determined by the MST technique.

In this section we will simulate the obliquely and normally incident SH plane waves onto a slab of flat cracks. We consider then a 2D isotropic homogeneous elastic medium with N cracks randomly distributed within a rectangular area of thickness $2h$ (see Fig. 6.1). The properties of the isotropic material are $\rho = 1\,g/cm^3$ and $c_t = 1\,mm/\mu s$. All the cracks are assumed to have the same length $2a$ and to be parallel to the X-axis in the defined coordinate system (X,Y). Cartesian coordinates for left starting point of each crack $(p_j, q_j)_{j=1,\ldots,N}$ are determined by generating $2N$ random numbers uniformly distributed in the range $[0,1]$ with the help of a standard computational routines. These two sets of coordinates are multiplied by the horizontal and vertical dimensions of the crack region for providing the values of p_j and q_j respectively. If during the random location process a new generated crack overlaps or touches a previously set up one, the process of determination of a new location is redone. All the crack surfaces are assumed to be stress free (sliding contact). The geometrical centre of the rectangular area defines the origin of the coordinate system.

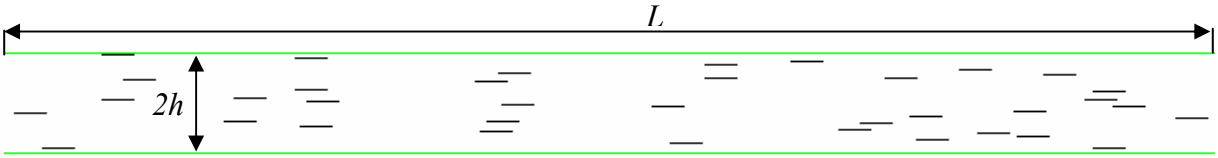

Fig. 6.4 *The scheme of a rectangular layer with randomly distributed flat cracks.*

The crack-number density ε per surface unit is defined as follows

$$\varepsilon = \frac{N}{S}, \tag{6.13}$$

where N is the number of cracks within the area $S = 2hL$ of rectangular slab considered in the simulation. Normalising this area by the length of the crack ($L \to \frac{L}{a}$ and $h \to \frac{h}{a}$) provides the surface density of cracks

$$n_0 = \frac{Na^2}{S}. \tag{6.14}$$

We can generate a plane wave using two different approaches. The first approach uses the technique of the initial condition area placed above the cracked zone and extended along the X-axis over the entire computational domain including the PMLs. The second approach consists in using the line source technique. The horizontal line source is extended over the entire computational domain up to the PMLs and it is placed at the top Y-coordinate of the computational domain just below the PML. The PMLs are added at all the edges of the computational domain for modelling an infinite medium.

The reflection and transmission spectra are extracted from the simulations and their moduli will be presented as functions of the reduced frequency $ka = 2\pi fa / c_t$. The numerical results are compared with two semi-analytical methods of multiple scattering by flat cracks: the finite-size crack technique and the line-like scatterer approach (see Section 6.2). Calculation of the reflection and transmission coefficients implies extracting SH coherent signal from the simulations (mean field recovery). In order to do so we can perform either of the following two procedures. The first one consists in finding the mean signals by spatially averaging the wave field probed along two lines parallel to the cracked layer, above and below it. This technique necessitates only one numerical simulation. The second procedure assumes averaging the numerical results at a single point (one below and the other above the layer) over a certain number of simulations with different samples of the crack distributions (with the same characteristics of the uniform random distribution). This latter technique is much more efficient than the 'spatial averaging' for a good estimation of the mean field, especially for low crack densities and for the case of oblique incidence. That is why it is going to be used below.

Afterwards we calculate the transmitted and reflected spectra of the final signals by means of FFT (using zero-padding technique if needed). Dividing the obtained spectra by the spectrum of the incident wave gives the transmission and reflection coefficients in the chosen band.

Nota Bene

In the rest of this chapter, we present a series of results describing various cases of reflection/transmission of a plane wave in a slab composed of identical inclusions randomly distributed in a homogeneous matrix.

The first part concerns SH waves scattered by populations of parallel flat cracks. Here we analyze implication of the thickness of the slab (simulations 1 and 2), of the concentration of scatterers (simulation 3), of the angle of incidence of the incoming plane wave (simulations 4 and 5), and finally of a non uniform distribution of cracks (Gaussian distribution — simulation 6).

The second part presents the results for P/SV waves scattered from the cylindrical solid inclusions (simulations 7 and 8). The last simulation deals with the concept of the 'effective' thickness of the slab with scatterers of non-zero volume (simulation 9).

6.4.1 Uniform crack distribution

In this section the statistical distribution of the cracks within the layer is supposed to be uniform over space. All the cracks are parallel to the faces of the delimiting layer and have the same length $2a$.

6.4.1.3 Normally incident plane wave

Simulation 1 ($h = 3a$ **,** $n_0 = 0.07$ ***)***

Let us consider the case of normally incident SH plane wave on the cracked layer. We choose a Ricker wavelet as a time function for the incident plane wave. In the process of configurational averaging (over several simulations), the width and the height of the cracked zone for each simulation are defined precisely by fixing the positions of four cracks. One of them is forced to be at the top edge of the layer, while its horizontal position is let to be arbitrary. The same procedure is performed for the three other cracks at the bottom, left and right edges. Proceeding this way ensures that the bounds of the layer are statistically well

defined. To obtain the reflection and transmission coefficients from the simulations we probe horizontally the wave field over two lines parallel to the layer: the first is above the initial condition zone (thereby excluding the incident wave contribution and probing the reflected field only), and the second is below the cracked layer (in the homogeneous part of the medium). By performing the averaging procedures (see Table 6.1) we extract the coherent signals from the whole set of simulations. The division of the obtained spectra by the incident wave spectrum gives the transmission and reflection coefficients (see Figs. 6.5 and 6.6) in the chosen band $0 \le ka \le k_{\max}a\left(= 2\pi f_{\max}a / c_t \approx 3.1\right)$.

<table>
<tr><th>Frequency range</th><th colspan="2">Discretization</th><th>Computational domain</th><th>Physical domain</th></tr>
<tr><td>$0 - 3.82\ MHz$
$\lambda_{\min} = \dfrac{c_{\min}}{f_{\max}} = 20\Delta x$</td><td colspan="2">$\Delta x = 0.013\,mm$
$\Delta y = 0.013\,mm$
$\Delta t = 0.009\,\mu s$</td><td>$L = 2000$ cells (X)
$l = 70$ cells (Y)
2048 time steps</td><td>$L = 26\,mm$
$l = 0.91\,mm$
running time $18\,\mu$s</td></tr>
<tr><th rowspan="2">Averaging type</th><th colspan="2">Source</th><th rowspan="2">Cracked rectangular zone characteristics</th><th rowspan="2">Cracked rectangular zone discretization</th></tr>
<tr><th>Type</th><th>Incident angle</th></tr>
<tr><td>- Through 80 simulations
- Along the receiver line of 200a</td><td>Initial condition</td><td>0°</td><td>$n_0 = 0.07, N = 84$
$a = 10$ cells (X)
$L_z = 200a,$
$h = 3a$</td><td>$a = 0.13mm$ (X)
$L_z = 26mm$
$h = 0.39mm$</td></tr>
<tr><td>Source function</td><td colspan="4">$s(t) = \dfrac{4}{\sqrt{\pi}}\left(\dfrac{1}{2} - \left(4t\right)^2\right)\exp\left(-\left(4t\right)^2\right)$</td></tr>
<tr><td>Scaling function</td><td colspan="4">NONE</td></tr>
<tr><td>Transition zone length</td><td colspan="4">NONE</td></tr>
<tr><td>Buffer zone length</td><td colspan="4">NONE</td></tr>
<tr><td>Control zone length</td><td colspan="4">NONE</td></tr>
<tr><td>Zero padding for FFT</td><td colspan="4">over 16 384 time steps</td></tr>
</table>

Table 6.1 *Parameters of the Simulation 1*

The curves extracted from the FDTD scheme show a good agreement with the curves calculated by the MST methods at low frequency, while the agreement deteriorates at a higher frequency within the chosen band. Getting more reliable numerical results for higher

frequencies requires much more simulations in the averaging process. Also we have noted a systematic deviation at high frequencies in between the numerical experiments and the analytics which is probably due to possible drawbacks of our numerical procedure, particularly concerning the configurational averaging at not so small values of ka .

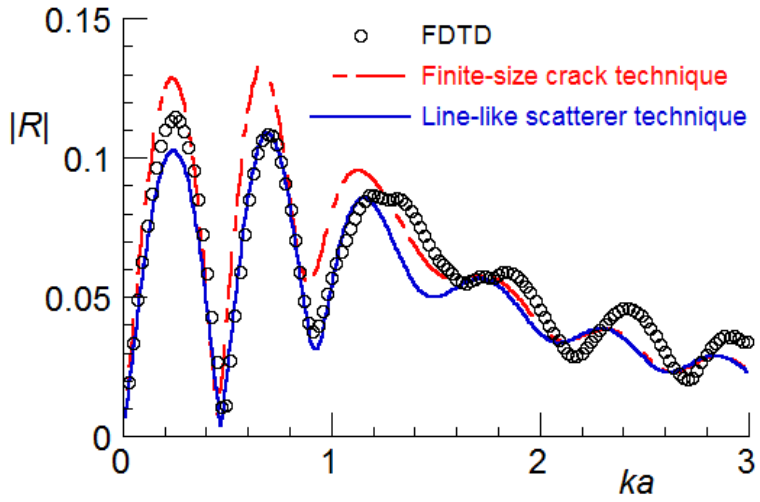

Fig. 6.5 *Reflection coefficient modulus versus nondimensional frequency for the concentration of cracks* $n_0 = 0.07$ *and the half-thickness* $h = 3a$ *. The dashed line and solid line present the theoretical results obtained by the finite-size crack method and the line-like scatterer technique, respectively; the circles present the numerical data obtained from FDTD.*

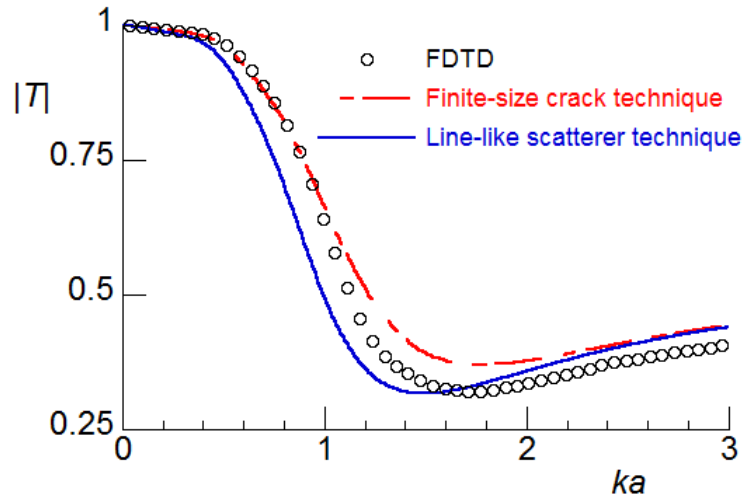

Fig. 6.6 *The same as in Fig. 6.5 but for the transmission coefficient T.*

Simulation 2 ($h = 12a, n_0 = 0.07$ ***)***

Let the layer thickness be four times greater than in the Simulation 1, so that $h = 12a$. Modifying the cracked zone requires the vertical extension of the computational domain up to

455 cells (=$5.915\,mm$) in order to fit the cracked zone to the numerical domain. To conserve the same crack density $n_0 = 0.07$ we increase by four times the number of cracks within the zone ($N = 336$). All the other parameters are left the same as in the Simulation 1.

<table>
<tr><th>Frequency range</th><th colspan="2">Discretization</th><th>Computational domain</th><th>Physical domain</th></tr>
<tr><td>$0 - 3.82\,MHz$
$\lambda_{\min} = \frac{c_{\min}}{f_{\max}} = 20\Delta x$</td><td colspan="2">$\Delta x = 0.013\,mm$
$\Delta y = 0.013\,mm$
$\Delta t = 0.009\,\mu s$</td><td>$L = 2000$ cells (X)
$l = 455$ cells (Y)
2048 time steps</td><td>$L = 26\,mm$
$l = 5.915\,mm$
running time $18\,\mu$s</td></tr>
<tr><td rowspan="2">Averaging type</td><td colspan="2">Source</td><td rowspan="2">Cracked rectangular zone characteristics</td><td rowspan="2">Cracked rectangular zone discretization</td></tr>
<tr><td>Type</td><td>Incident angle</td></tr>
<tr><td>- Through 80 simulations
- Along the receiver line of 200a</td><td>Initial condition</td><td>0°</td><td>$n_0 = 0.07, N = 336$
$a = 10$ cells (X)
$L_z = 200a,$
$h = 12a$</td><td>$a = 0.13mm$ (X)
$L_z = 26mm$
$h = 1.56mm$</td></tr>
<tr><td>Source function</td><td colspan="4">$s(t) = \frac{4}{\sqrt{\pi}}\left(\frac{1}{2} - \left(4t\right)^2\right)\exp\left(-\left(4t\right)^2\right)$</td></tr>
<tr><td>Scaling function</td><td colspan="4">NONE</td></tr>
<tr><td>Transition zone length</td><td colspan="4">NONE</td></tr>
<tr><td>Buffer zone length</td><td colspan="4">NONE</td></tr>
<tr><td>Control zone length</td><td colspan="4">NONE</td></tr>
<tr><td>Zero padding for FFT</td><td colspan="4">over 16384 time steps</td></tr>
</table>

Table 6.2 *Parameters of the Simulation 2*

Figs. 6.7 and 6.8 present the reflection and transmission coefficients for this case. A very good agreement between the analytical and numerical data is observed up to $ka = 1$, especially in the positions of thickness resonances of the layer. This confirms that the effective wavenumber provided by the MST coincides markedly well with the data extracted from the FDTD.

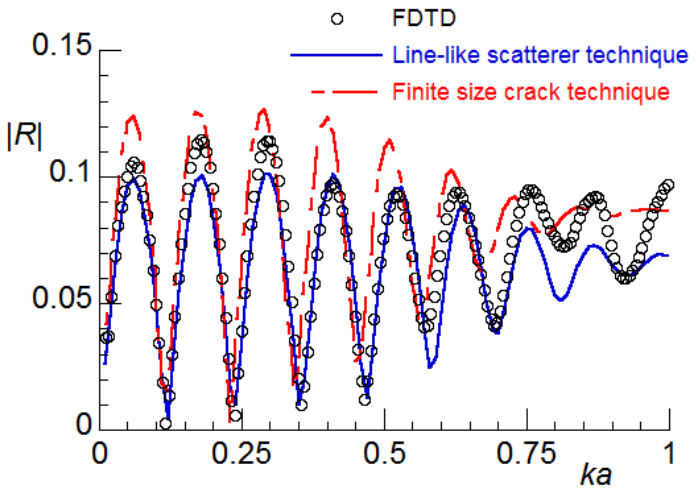

Fig. 6.7 *Reflection coefficient modulus versus nondimensional frequency for the concentration of cracks* $n_0 = 0.07$ *and a half-thickness* $h = 12a$ *. The dash line presents the finite-size crack method; the solid line presents the line-like scatterer technique; and the empty black circles present the numerical data obtained from FDTD.*

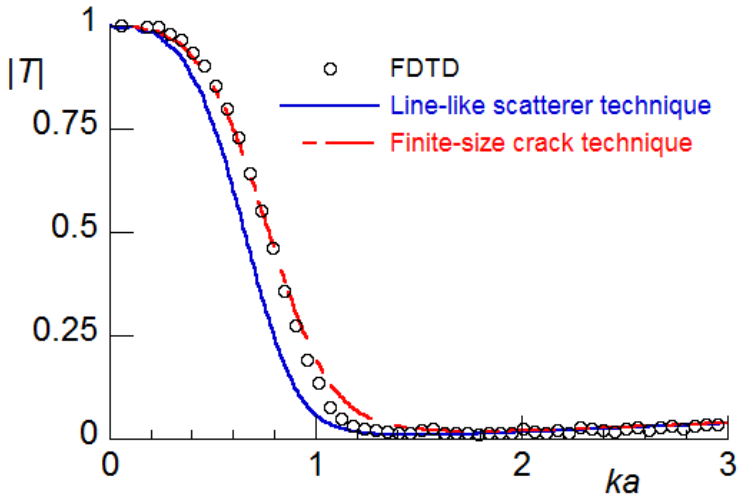

Fig. 6.8 *The same as in Fig. 6.7 but for the transmission coefficient T.*

Simulation 3 ($h = 3a$ **,** $n_0 = 0.01$ ***)***

Dependence on the concentration of inclusions is an important issue when retrieving the coherent-wave properties by means of configurational averaging from a set of deterministic numerical simulations. In the numerical context, the 'statistics' of a random medium can be 'felt' by the incident wave if the latter interacts with a sufficient number of scatterers. In this regard, we are going to observe the implication of a low concentration of inclusions in our numerical experiments.

Let us consider a crack concentration that is seven times less than in the Simulation 1 (with the same thickness of the layer). For a better uniformity of the crack distribution, we partition the entire layer in three equivalent zones (of area $200a \times 6a$ each) within which three random series of twelve cracks are generated. These three adjacent zones fill horizontally the entire computational domain, up to the PMLs, and can be viewed as a single cracked layer three times larger and having three times more cracks. This does certainly not affect the crack-number density ($n_0 = 0.01$). The central zone is used for probing the wave field. We arrange the 2000-point long top and bottom probing lines above and below the central zone respectively. Due to the large width of the simulation, it is necessary to reduce its vertical dimension (orthogonally to the plate). The technique of 'acoustical sources' is therefore employed for generating the incident plane wave. Extracting the reflected wave in this case demands an additional treatment. We perform the simulations under the same numerical conditions but without any crack. Then the top receiver probes the incident signal only. Afterwards, we subtract the previously captured incident signal from the average signal of the fifty-two simulations probed by the top receiver. Hence the reflected coherent wave is obtained, from which the reflection coefficient is calculated. The latter is presented in Fig. 6.9. The transmission coefficient (see Fig. 6.10) is obtained the same way as for the previous Simulation 1.

<table>
<tr><th>Frequency range</th><th>Discretization</th><th colspan="2">Computational domain</th><th>Physical domain</th></tr>
<tr><td>$0 - 3.82\,MHz$
$\lambda_{\min} = \frac{c_{\min}}{f_{\max}} = 20\Delta x$</td><td>$\Delta x = 0.013\,mm$
$\Delta y = 0.013\,mm$
$\Delta t = 0.009\,\mu s$</td><td colspan="2">$L = 6000$ cells (X)
$l = 70$ cells (Y)
2048 time steps</td><td>$L = 78\,mm$
$l = 0.91\,mm$
running time $18\,\mu$s</td></tr>
<tr><th rowspan="2">Averaging type</th><th colspan="2">Source</th><th rowspan="2">Cracked rectangular zone characteristics</th><th rowspan="2">Cracked rectangular zone discretization</th></tr>
<tr><th>Type</th><th>Incident angle</th></tr>
<tr><td>- Through 52 simulations
- Along the receiver line of 200a</td><td>Horizontal line source</td><td>0°</td><td>$n_0 = 0.01, N = 12$
$a = 10$ cells (X)
$L_z = 200a,$
$h = 3a$</td><td>$a = 0.13mm$ (X)
$L_z = 26mm$
$h = 0.39mm$</td></tr>
<tr><td>Source function</td><td colspan="4">$s(t) = \frac{4}{\sqrt{\pi}}\left(\frac{1}{2} - \left(4t\right)^2\right)\exp\left(-\left(4t\right)^2\right)$</td></tr>
</table>

Scaling function	$H(\|x\| - 26.000001)\exp(-(\frac{\|\|x\| - 26\|}{6.5})^3) + H(26.000001 - \|x\|)$
Transition zone length	1000 points
Buffer zone length	1000 points
Control zone length	2000 points
Zero padding for FFT	over 16384 time steps

Table 6.3 *Properties of the Simulation 3*

The agreement between the FDTD results with the MST is not as good as in the Simulation 1. This is mainly due to the insufficient number of scatterers which leads to a poor recovery of the mean field. In order to improve this recovery it would be necessary to take a very large amount of simulations for the configurational averaging and then to better resolve the wave statistics.

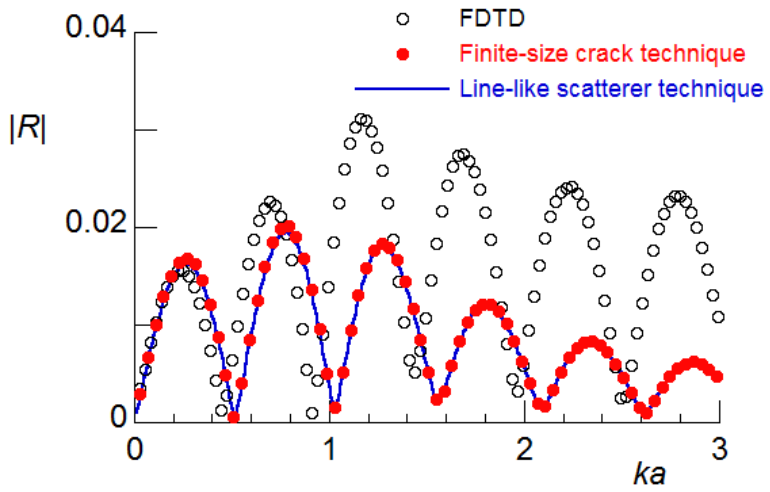

Fig. 6.9 *Reflection coefficient modulus versus nondimensional frequency for the concentration of cracks* $n_0 = 0.01$ *and the half-thickness* $h = 3a$ *. The red circles present the finite-size crack method; the solid line presents the line-like scatterer technique; and the empty circles present the numerical data obtained from FDTD.*

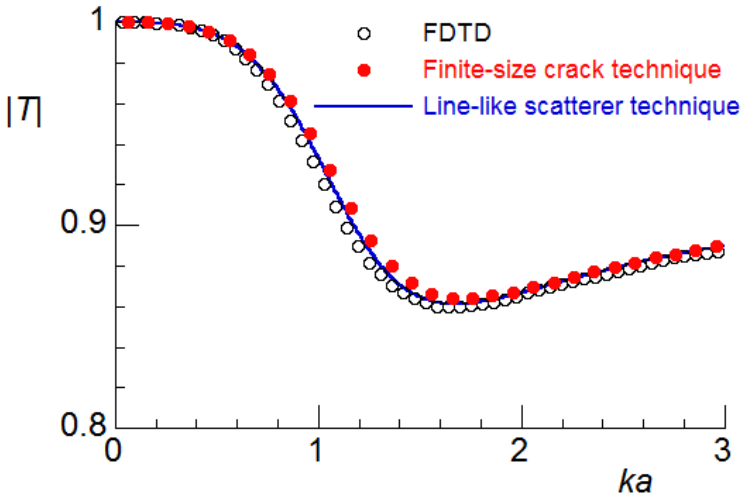

Fig. 6.10 *The same as in Fig. 6.9 but for the transmission coefficient T.*

6.4.1.4 Comparison of the two approaches for numerical generation of plane waves

This short section concerns the implication of generating the incident plane wave using either the line source (source terms in the wave equation) or the initial conditions setup (fixing spatially the wave field at the first value of time).

We compare two simulations based on the input parameters of the simulation 1 ($h = 3a$ and $n_0 = 0.07$) but with the two different ways of generating the incident plane wave. Figure 6.11 shows the reflection coefficient obtained from these two numerical simulations (along with the theoretical results from line-like scatterer technique). It can be seen that the difference between the two numerical approaches of the plane wave excitation is not really significant in the ka -range of interest.

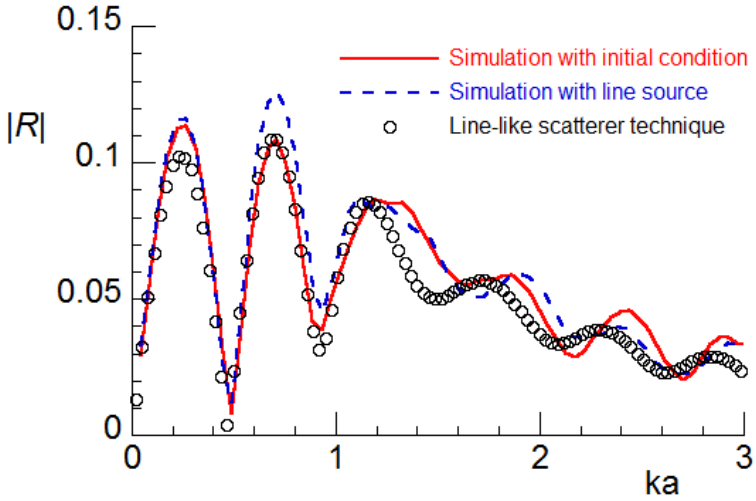

Fig. 6.11 *Reflection coefficient modulus versus nondimensional frequency for the concentration of cracks* $n_0 = 0.07$ *and the half-thickness* $h = 3a$ *. The solid line and the dashed line present the numerical results extracted from*

the simulation with initial conditions and with the line source, respectively; the empty circles show the theoretical dependence calculated by the line-like scatterer method.

6.4.1.5 Obliquely incident plane wave

In this section we consider oblique incidence of the SH plane wave on an inhomogeneous layer. The angle of incidence is denoted by θ.

Simulation 4 ($h = 3a$, $n_0 = 0.07$, $\theta = 15°$ ***)***

Consider oblique incidence under the angle 15º. The arrangement of crack distribution, crack size, spatial and temporal discretization as well as the computational domain parameters are similar to those of the Simulation 3 but with the crack density of the Simulation 1, that is, with $n_0 = 0.07$. For this concentration of cracks, each of the three parts of the layer accommodates eighty four cracks ($N = 84$). The horizontal line source is extended over the entire computational domain up to the PMLs and placed at the top *y*-coordinate of the computational domain, just below the PML. We choose two probing points, one above and one below the cracked region (both with $x = 0$, that is at the horizontal center of the layer) and perform signal averaging at these points over 84 simulations with different samples of the crack distribution. In this simulation the spectrum at the probing point includes the sum of the incident and the reflected waves. By analogy with the case of Simulation 3, the reflected wave is determined by performing one more simulation with the same parameters but without any cracks. The reflection and transmission coefficients are presented in Figs. 6.12 and 6.13.

Frequency range	**Discretization**		**Computational domain**	**Physical domain**
$0 - 3.82\ MHz$ $\lambda_{\min} = \frac{c_{\min}}{f_{\max}} = 20\Delta x$	$\Delta x = 0.013\,mm$ $\Delta y = 0.013\,mm$ $\Delta t = 0.009\,\mu s$		$L = 6000$ cells (X) $l = 70$ cells (Y) 4096 time steps	$L = 78\,mm$ $l = 0.91\,mm$ running time $\approx 37\,\mu$s
Averaging type	**Source**		**Cracked rectangular zone characteristics**	**Cracked rectangular zone discretization**
	Type	**Incident angle**		
- Through 84 simulations	Horizontal line source	15°	$n_0 = 0.07, N = 84$ $a = 10$ cells (X) $L_z = 200a$, $h = 3a$	$a = 0.13mm$ (X) $L_z = 26mm$ $h = 0.39mm$

Source function	$\frac{4}{\sqrt{\pi}}(0.5-(4(\sin(15°)(x+39)-t-2))^2)\exp(-(4(\sin(15°)(x+39)-t-2))^2)$
Scaling function	$H(\lvert x\rvert-26.000001)\exp(-(\frac{\lvert\lvert x\rvert-26\rvert}{6.5})^3)+H(26.000001-\lvert x\rvert)$
Transition zone length	1000 points
Buffer zone length	1000 points
Control zone length	2000 points
Zero padding for FFT	over 16384 time steps

Table 6.4 *Parameters of the Simulation 4*

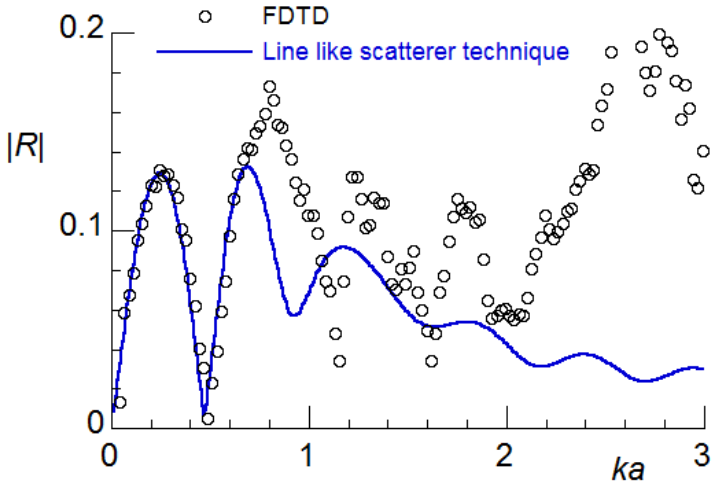

Fig. 6.12 *Reflection coefficient modulus versus nondimensional frequency for the concentration of cracks* $n_0 = 0.07$ *, the half-thickness* $h = 3a$ *and the incident angle q=15°. The solid line presents the theoretical result obtained by the line-like scatterer technique; the circles present the numerical data obtained from FDTD.*

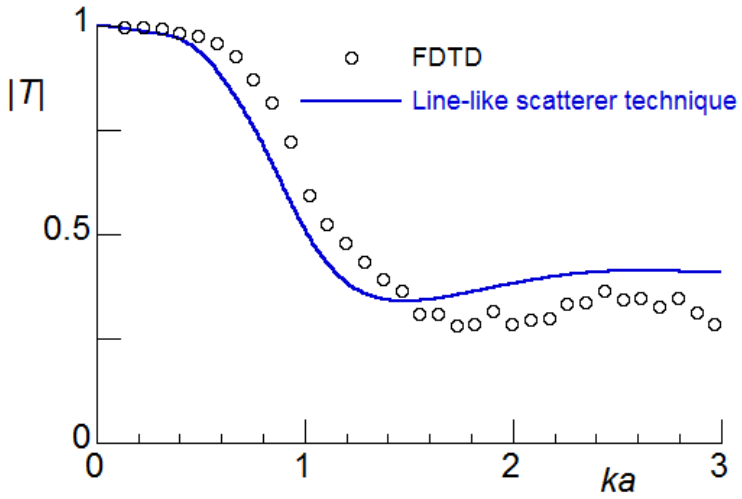

Fig. 6.13 *The same as in Fig. 6.12 but for the transmission coefficient T.*

Simulation 5 ($h = 10a$, $n_0 = 0.07$, $\theta = 45°$ ***)***

Let us show one more example of simulation where the oblique plane wave has a greater incident angle ($\theta = 45°$). We choose probing points above and below the crack region and place them horizontally at the middle of the domain. These points are located far enough from the edges of the computational domain in order to avoid perturbations due to a finite size of the source. We apply the procedure of the incident field subtraction as in the Simulation 4. The reflection and transmission spectra are presented in Figs. 6.14 and 6.15. A good agreement is seen between the numerical and the theoretical results up to $ka = 0.6$ for the reflection coefficient and up to $ka = 3$ for the transmission coefficient.

Frequency range	**Discretization**		**Computational domain**	**Physical domain**
$0 - 3.82\ MHz$ $\lambda_{\min} = \frac{c_{\min}}{f_{\max}} = 20\Delta x$	$\Delta x = 0.013\ mm$ $\Delta y = 0.013\ mm$ $\Delta t = 0.009\ \mu s$		$L = 3000$ cells (X) $l = 220$ cells (Y) 4096 time steps	$L = 39\ mm$ $l = 2.86\ mm$ running time $\approx 37\ \mu$s
Averaging type	**Source**		**Cracked rectangular zone characteristics**	**Cracked rectangular zone discretization**
	Type	**Incident angle**		
- Through 84 simulations	Horizontal line source	45°	$n_0 = 0.07, N = 420$ $a = 10$ cells (X) $L_z = 300a$ $h = 10a$	$a = 0.13mm$ (X) $L_z = 39mm$ $h = 1.3mm$

Source function	$\frac{4}{\pi}(0.5-(4(\sin(45°)(x+19.5)-t-2))^2)\exp(-(4(\sin(45°)(x+19.5)-t-2))^2)$
Scaling function	$H(\lvert x\rvert-6.500001)\exp(-(\frac{\lvert\lvert x\rvert-6.5\rvert}{6.5})^3)+H(6.500001-\lvert x\rvert)$
Transition zone length	1000 points
Buffer zone length	NONE
Control zone length	1000 points
Zero padding for FFT	over 16384 time steps

Table 6.5 *Parameters of the Simulation 5*

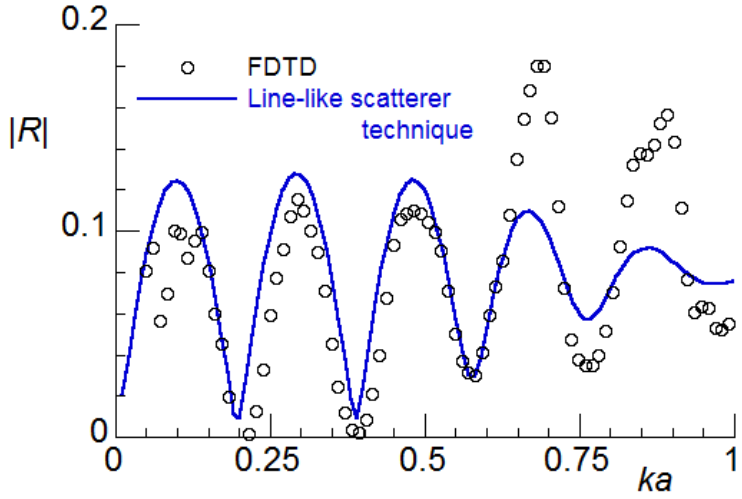

Fig. 6.14 *Reflection coefficient modulus versus nondimensional frequency for the concentration of cracks* $n_0 = 0.07$, *the half-thickness* $h = 10a$ *and an incident angle q= 45°. The solid line presents the theoretical result obtained by the line-like scatterer technique; the circles present the numerical data obtained from FDTD.*

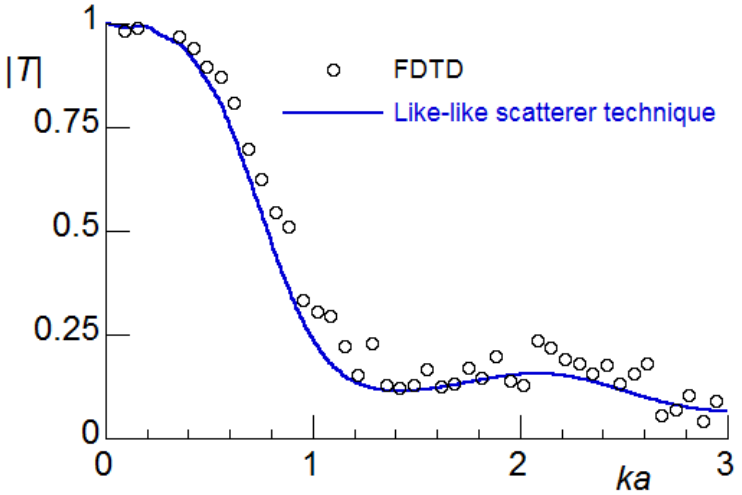

Fig. 6.15 *The same as in Fig. 6.14 but for the transmission coefficient T.*

6.4.2 Gaussian crack distribution – Simulation 6

We consider here the case of a layer of non-uniform crack density along its thickness. The statistical distribution of cracks within the layer is chosen to be of Gaussian type. Specifically, the non-uniform space-varying crack density $\eta(y)$ is given by the Gaussian law

$$\eta(y) = \eta_0 \frac{e^{-\left(\frac{y-h}{\sigma}\right)^2} - e^{-\left(\frac{h}{\sigma}\right)^2}}{1 - e^{-\left(\frac{h}{\sigma}\right)^2}}, \tag{6.15}$$

where $0 \le y \le 2h$ (so that $\eta(0) = \eta(h) = 0$), $\sigma = 6a$, $h = 12a$ (= 120 cells) and $a = 0.13\,mm$ (= 10 cells). Of course, the populations of cracks generated for numerical simulations do not follow rigorously this Gaussian-type distribution. In order to make comparisons with theoretical predictions, one has to fix a specific distribution for analytics. The first stage is then to generate the samples for each simulation following the law (6.15). At the second stage, one calculates the best fit for the theoretical Gaussian distribution of the type (6.15) over the thickness of the layer and also over the whole set of samples generated. The fitted parameter is the factor η_0, σ being unchanged. The latter value of η_0 is then used for the theoretical predictions. The results of this procedure are shown in Fig. 6.16.

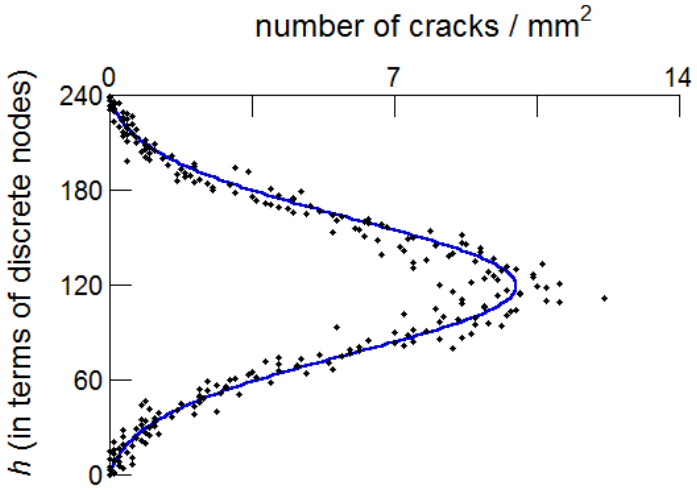

Fig. 6.16 *Profile of the non-uniform crack density $\eta(y)$. The black points represent the numerically generated crack distribution; the solid line represents the best fit by the law (6.15) of the numerical sample.*

The reflection and transmission coefficients of the mean wave are numerically determined in the same manner as for the uniform distributions presented before. Concerning the theoretical predictions, one can find a detailed calculation of the reflection and

transmission coefficients by the propagator-matrix approach in [12]. The comparison of our numerical data and the theoretical results of [12] is shown in Figs. 6.17 and 6.18.

<table>
<tr><th>Frequency range</th><th colspan="2">Discretization</th><th>Computational domain</th><th>Physical domain</th></tr>
<tr><td>$0-3.82\,MHz$
$\lambda_{\min}=\frac{c_{\min}}{f_{\max}}=20\Delta x$</td><td colspan="2">$\Delta x=0.013\,mm$
$\Delta y=0.013\,mm$
$\Delta t=0.009\,\mu s$</td><td>$L=500$ cells (X)
$l=455$ cells (Y)
16384 time steps</td><td>$L=6.5\,mm$
$l=5.915\,mm$
running time $\approx 147\,\mu$s</td></tr>
<tr><th rowspan="2">Averaging type</th><th colspan="2">Source</th><th rowspan="2">Cracked rectangular zone characteristics</th><th rowspan="2">Cracked rectangular zone discretization</th></tr>
<tr><th>Type</th><th>Incident angle</th></tr>
<tr><td>- Through 108 simulations
- Along the receiver line of 50a</td><td>Initial condition</td><td>0°</td><td>$a=10$ cells (X)
$L_z=50a$
$h=12a$</td><td>$a=0.13mm$ (X)
$L_z=6.5mm$
$h=1.56mm$</td></tr>
<tr><td>Source function</td><td colspan="4">$s(t)=\frac{4}{\sqrt{\pi}}\left(\frac{1}{2}-\left(4t\right)^2\right)\exp\left(-\left(4t\right)^2\right)$</td></tr>
<tr><td>Scaling function</td><td colspan="4">NONE</td></tr>
<tr><td>Transition zone length</td><td colspan="4">NONE</td></tr>
<tr><td>Buffer zone length</td><td colspan="4">NONE</td></tr>
<tr><td>Control zone length</td><td colspan="4">NONE</td></tr>
<tr><td>Zero padding for FFT</td><td colspan="4">NONE</td></tr>
</table>

Table 6.6 *Parameters of the Simulation 6.*

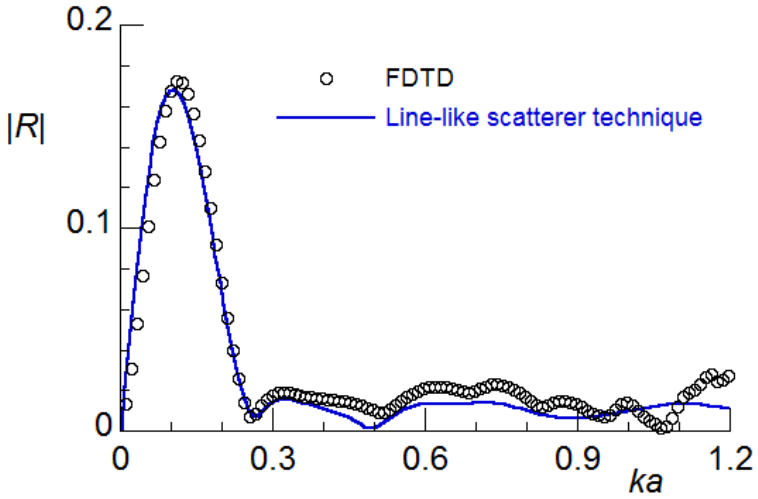

Fig. 6.17 *Reflection coefficient modulus versus nondimensional frequency for a non-uniform (Gaussian) crack distribution. The solid line presents the theoretical result obtained by the line-like scatterer technique; the circles present the numerical data obtained from FDTD.*

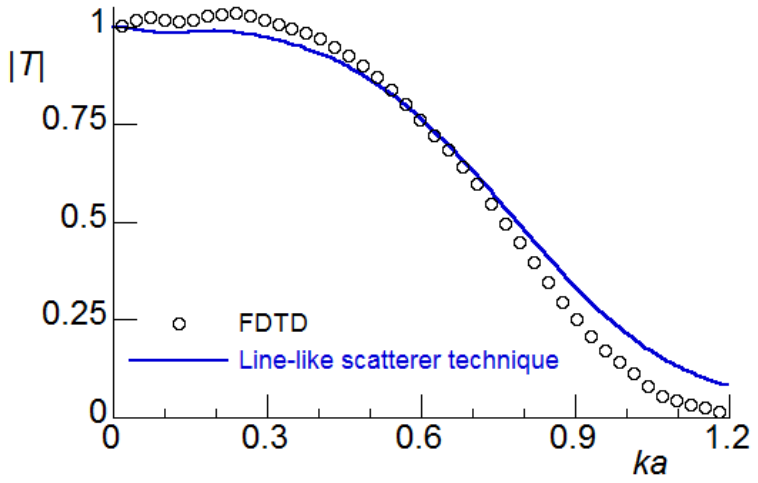

Fig. 6.18 *The same as in Fig. 6.17 but for the transmission coefficient T.*

6.5 P/SV wave scattering by a layer of uniformly distributed cylindrical inclusions

In this section we will simulate normally incident P- and SV plane waves onto a layer of cylindrical filled inclusions. We consider a 2D isotropic homogeneous elastic medium with N 2D circular inclusions (cylinders) randomly and uniformly distributed within a rectangular zone (see Fig. 6.19). Let the matrix be made of aluminium

$$\rho_1 = 2.7\, g / cm^3, c_{1t} = 3.13\, mm / \mu s, c_{1l} = 6.32\, mm / \mu s, \tag{6.16}$$

and the inclusions be made of steel

$$\rho_2 = 7.932\, g/cm^3, c_{2t} = 3.26\, mm/\mu s, c_{2l} = 5.96\, mm/\mu s. \tag{6.17}$$

All cylinders are assumed to have the same radius a. For the numerical simulations, the generation of distributions of cylinders is performed under the same conditions as for the crack problem.

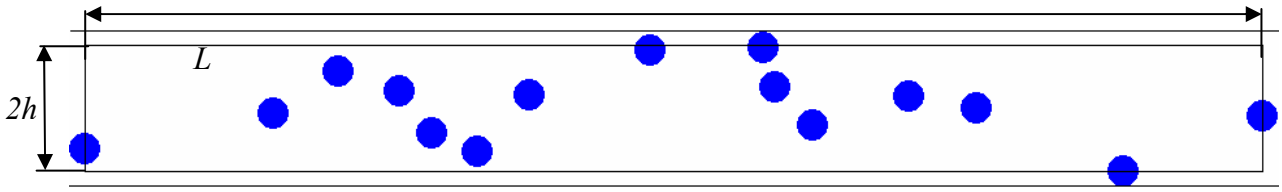

Fig. 6.19 *The scheme of rectangular layer with cylindrical inclusions.*

The volume fraction ϕ of inclusions is defined as follows

$$\phi = \frac{1}{S_{zone}} \sum_i S_i\,, \tag{6.18}$$

where S_i is the surface cross-section of the i-th inclusion and S_{zone} is the surface of the rectangular region enclosing the centres of all the cylinders. Since the cylinders have the same radius, expression (6.18) becomes

$$\phi = \frac{N\pi a^2}{2Lh}. \tag{6.19}$$

The height $2h$ of the rectangular region is defined from the centres of two extreme cylinders. Thus the calculation of ϕ includes all the cylinders, even if some of them partially exceed the rectangular region.

Two simulations are presented in this section, one for the SV wave and the other for the P wave. The numerical procedure is similar to that used in the case of SH waves.

For a better uniformity of the distribution of inclusions, we partition the initial layer into several zones within which the generation of random positions of the objects is carried out. Then we generate a plane wave using the line source technique. The horizontal line source is extended over the entire computational domain up to the PMLs and it is placed at the top y-coordinate of the computational domain just under the PML. For the SV wave we excite the wave along the line source by incorporating a source function f_1 in the formula (3.13) of Chapter 3. In the same manner, the P wave is excited by applying a time function to the term f_2 in the same formula. The simulations yield the dependence of reflection and transmission coefficients on the reduced frequencies $k_t a = \frac{\omega}{c_t} a$ or $k_l a = \frac{\omega}{c_l} a$. The numerical results are

compared with the theoretical ones obtained with the approach of [5, 6] in the context of the Waterman and Truell (W&T) theory.

Frequency range	**Discretization**		**Computational domain**	**Physical domain**
$0-3.82\,MHz$ $\lambda_{\min}=\frac{c_{\min}}{f_{\max}}=23.43\Delta x$	$\Delta x=0.035\,mm$ $\Delta y=0.035\,mm$ $\Delta t=0.039\,\mu s$		$L=4200$ cells (X) $l=126$ cells (Y) 4096 time steps	$L=147\,mm$ $l=4.41\,mm$ running time $\approx 160\,\mu$s
Averaging type	**Source**		**Cracked rectangular zone characteristics**	**Cracked rectangular zone discretization**
	Type	**Incident angle**		
- Through 39 simulations - Along the receiver line of 50a	Horizontal line source	0°	$\phi\approx 6.41\%$ $a=12$ cells (X) $L_z=98a$ $h=4a$	$a=0.42mm$ (X) $L_z=41.16mm$ $h=1.68mm$
Source function	$s(t)=\frac{4}{\sqrt{\pi}}\left(\frac{1}{2}-\left(4t\right)^2\right)\exp\left(-\left(4t\right)^2\right)$			
Scaling function	$H(\lvert x\rvert-38.500001)\exp(-(\frac{\lVert x\rvert-38.5\rvert}{17.5})^3)+H(38.500001-\lvert x\rvert)$			
Transition zone length	1000 points			
Buffer zone length	1000 points			
Control zone length	1200			
Zero padding for FFT	over 16384 time steps			

Table 6.7 *Parameters of the P-SV Simulation*

6.5.1 SV wave – Simulation 7 ($h=4a$, $\phi\approx 6.41\%$)

Using the simulation setup presented in the Table 6.7, we obtain the coefficients of reflection and transmission of the SV wave by a layer with 6.41%-volume fraction of randomly dispersed solid cylinders. The results are shown in Figs. 6.20 and 6.21 versus the reduced frequency $k_t a$. One can see that the reflection coefficient is in a relatively good accordance with the formulas of Aristégui and Angel approach based on the W&T theory.

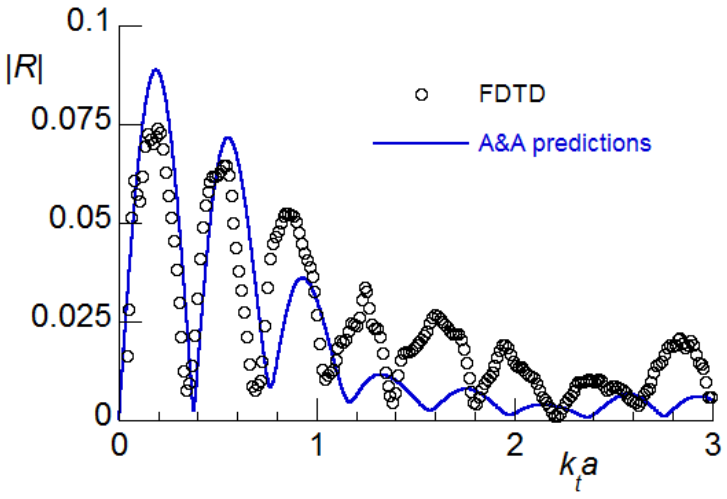

Fig. 6.20 *Reflection coefficient modulus of the SV-wave by a slab of uniform distribution of cylindrical solid inclusions. The solid line presents the theoretical results obtained from the Aristégui-Angel formulas; the circles present the numerical data obtained from FDTD.*

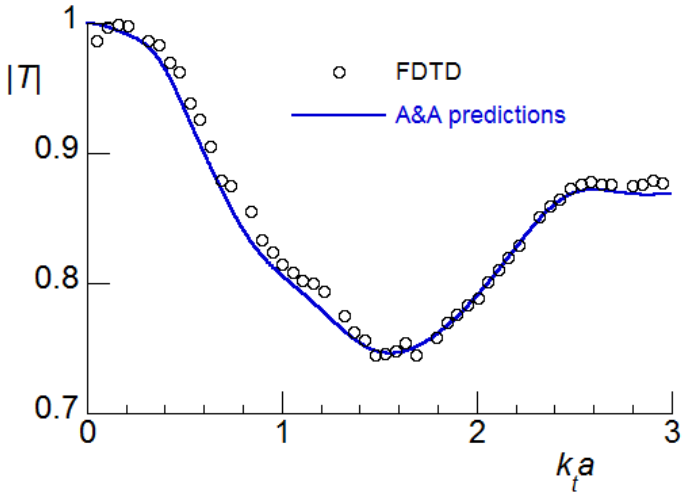

Fig. 6.21 *The same as in Fig. 6.20 but for the transmission coefficient T.*

6.5.2 P wave – Simulation 8 ($h = 4a$*,* $\phi \approx 6.41\%$*)*

The coefficients of reflection and transmission of the P wave are calculated in the same manner as for the SV wave. Figs. 6.22 and 6.23 show their absolute values as functions of the reduced-frequency $k_l a$. One can see that the transmission coefficient obtained by our FDTD procedure fits quite well with the theoretical predictions up to $k_l a = 1.5$ at least. On the other hand, the reflection coefficient starts to suffer a certain discrepancy with the theoretical predictions already at rather small $k_l a$. This is mainly due to the fact that the W&T theory

formally reduces the scatterers to points and thus their finite-size is not taken into account, which contradicts the numerical simulations where parts of some scatterers stick out beyond the theoretical thickness of the layer.

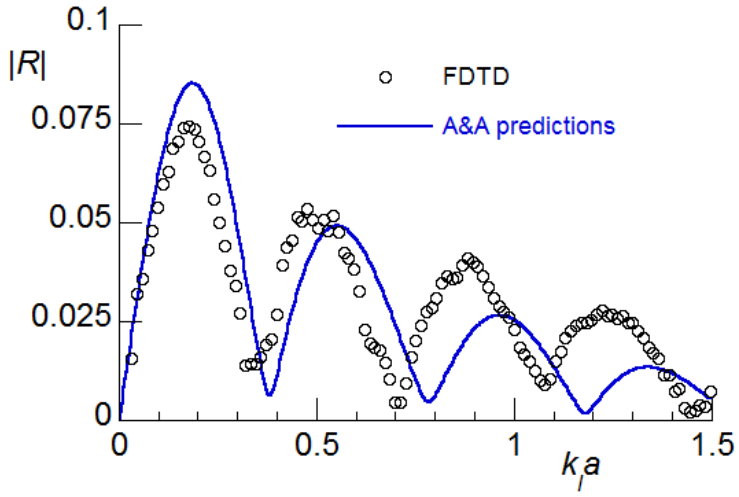

Fig. 6.22 *Reflection coefficient modulus of the P-wave by a slab of uniform distribution of cylindrical solid inclusions. The solid line presents the theoretical results by the Aristégui-Angel formulas; the empty points present the numerical data obtained from FDTD.*

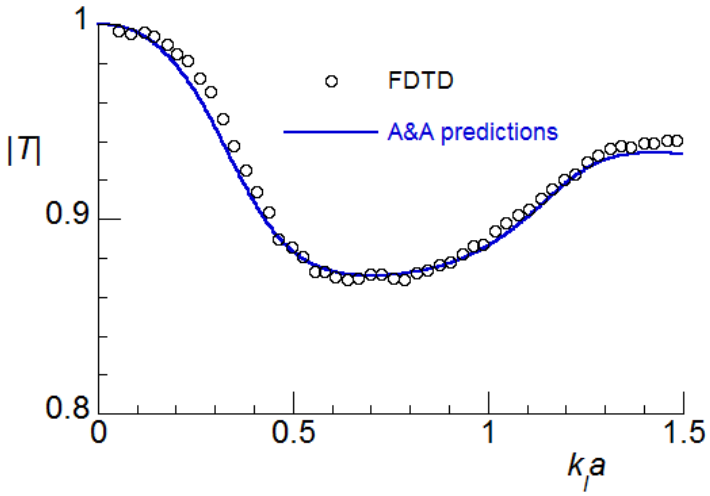

Fig. 6.23 *The same as in Fig. 6.22 but for the transmission coefficient T.*

6.5.3 The 'effective' thickness of a layer of randomly distributed finite-size scatterers

The results displayed in Figs. 6.20 and 6.22 show a systematic discrepancy between the numerical and theoretical quantification of the reflection peaks and dips which aggravates with growing ka. Indeed minimums and maximums of the reflection are particularly sensitive

to the chosen value of the layer thickness since they are governed by the thickness resonances of the layer occurring at $ka = \frac{2\pi f}{c} a \approx n \frac{\pi}{d} a$.

In the W&T formalism, the scatterers are reduced to points and hence the thickness is unambiguously defined from the centres of the extreme cylinders. But when the finite size of the scatterers is taken into account, as is the case in the numerical experiments, there is no obvious definition of the thickness. It can still be defined from the centres of the objects, but also from the area enclosing the objects entirely. The latter is greater than the former by exactly one diameter (for cylinders). Therefore comparing the techniques which either disregard or directly use the finite-size nature of the inclusions is tricky. This aspect is clearly observable from the obtained results for the reflection coefficient from cylindrical inclusions. Note that this does not happen for the case of flat cracks parallel to the layer faces (see e.g. Fig. 6.7), since here there is no ambiguity in the definition of the layer thickness (only one value comes into play).

The aim of this section is to explore the possibility of defining the 'effective' thickness for random layers constituted of finite-size objects. The idea is to tune the thickness used in the W&T model in order to match the theoretical values of the thickness resonance frequencies to the ones obtained from numerical simulation (and hence taking into account finite-size scatterers). At the same time, changing the thickness implies a change of the volume fraction if the number of objects is kept constant, or a change of the number of inclusions if the volume fraction remains the same. To this end, let us return to the cases presented in Sections 6.5.1 and 6.5.2. Generally speaking, the 'effective' value of h should lie between $4a$ and $5a$. Practically, if we allow the theoretical volume fraction ϕ to vary (meaning that the total number of inclusions within the layer is fixed), then by sweeping $\frac{h}{a}$ from 4 to 5 we may be able to find a value of $\frac{h}{a}$ at which the thickness resonances obtained from theoretical and numerical approaches will coincide. The best fit for the SV-wave problem (see Fig. 6.24) occurs at

$$\frac{h}{a} = 4.465\,,\ \phi \approx 5.7438\%\,. \tag{6.20}$$

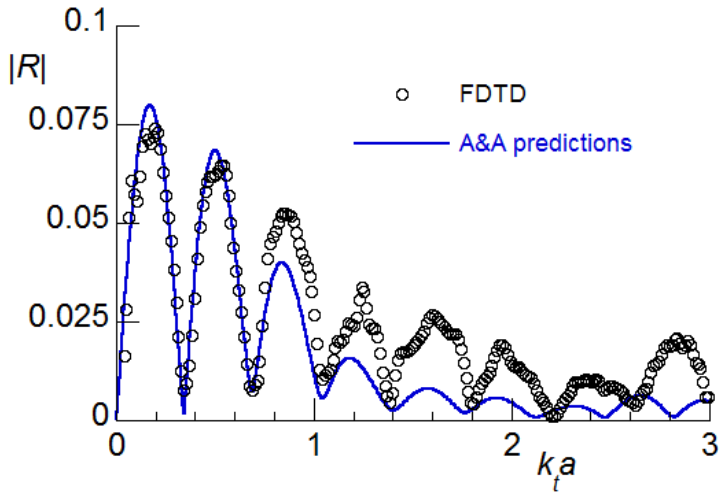

Fig. 6.24 *Comparison of the numerical and theoretical reflection coefficients for the SV-wave (simulation of 6.5.1), taking into account the 'effective' thickness correction* $h = 4.465a$ *for theory.*

The best fit for the P-wave problem (see Fig. 6.25) occurs at

$$h = 4.431a\,,\ \phi \approx 5.7878\%\,. \tag{6.21}$$

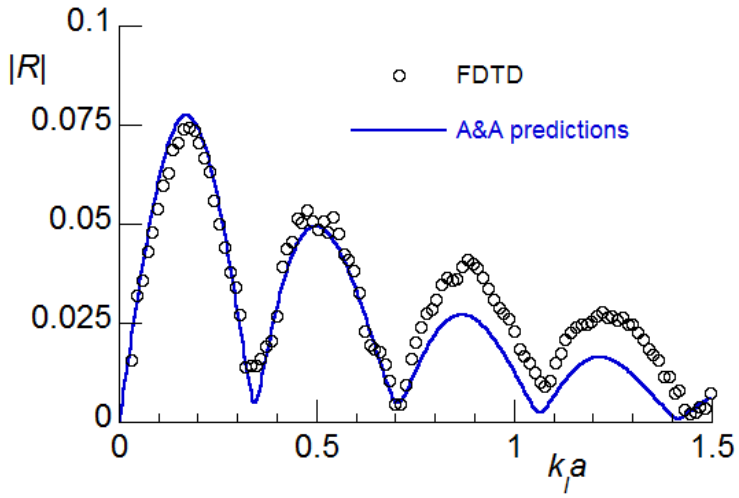

Fig. 6.25 *Comparison of the numerical and theoretical reflection coefficients for the P-wave (simulation of 6.5.2), taking into account the 'effective' thickness correction* $h = 4.431a$ *for theory.*

We expect that the effective thickness should increase with frequency and should finally reach the maximum value of $h = 5a$ due to the layer completely enclosing the finite-size cylinders. This conjecture is confirmed by certain frequency drift that persists in the results presented in Figs. 6.24 and 6.25.

References

1. L.L. Foldy, The multiple scattering of waves. I. General theory of isotropic scattering by randomly distributed scatterers, Phys. Rev. 67 (1945) 107.

2. A. Ishimaru, Wave Propagation and Scattering in Random Media, IEEE Press and Oxford University Press, Piscataway, NJ, 1997.

3. D. Sornette, Acoustic Waves in Random Media. I. Weak Disorder Regime, Acta acustica united with Acustica 67 (1989) 199-215.

4. Y.C. Angel, Y.K. Koba, Complex-valued wavenumber, reflection and transmission in an elastic solid containing a cracked slab region, Int. J. Solids Struct. 35 (1998) 573-592.

5. C. Aristégui, Y.C. Angel, Effective mass density and stiffness derived from P-wave multiple scattering, Wave Motion 44 (2007) 153-164.

6. C. Aristégui, Y.C. Angel, Effective material properties for shear-horizontal acoustic waves in fiber composites, Phys. Rev. E 75 (2007) 056607.

7. P.A. Martin, A. Maurel, W.J. Parnell, Estimating the dynamic effective mass density of random composites, J. Acoust. Soc. Am. 128 (2010) 571-577.

8. M. Caleap, B.W. Drinkwater, P.D. Wilcox, Effective dynamic constitutive parameters of acoustic metamaterials with random microstructure, New J. Phys. 14 (2012) 033014.

9. M. Chekroun, L.L. Marrec, B. Lombard, J. Piraux, Time-domain numerical simulations of multiple scattering to extract elastic effective wavenumbers, Waves Random Complex 22 (2012) 398-422.

10. M. Caleap, C. Aristégui, Effective antiplane properties in presence of frictional shear cracks, J. Geophys. Res. 115 (2010) B02302.

11. Y.C. Angel, C. Aristégui, Analysis of sound propagation in a fluid through a screen of scatterers, J. Acoust. Soc. Am. 118 (2005) 72-82.

12. C. Aristégui, M. Caleap, O. Poncelet, S.V. Golkin, A.L. Shuvalov, Coherent elastic wave propagation through non-uniform spatial distributions of cracks, in: Proceedings of Acoustics'08, 29 June–4 July, Paris, France, 2008. CD ROM, ISBN 978−2−9521105−4−9, pp. 5963−5967.

13. C. Aristégui, M. Caleap, O. Poncelet, A.L. Shuvalov, Y.C. Angel, Coherent wave propagation in solids containing spatially varying distributions of finite-size cracks, 5e Journée du GDR CNRS 2501, in: Étude de la propagation ultrasonore en milieux inhomogènes en vue du contrôle non-destructif, Ultrasonic Wave Propagation in Non Homogeneous Media, Anglet, France, 2009, pp. 423-435.

14. M. Caleap, C. Aristégui, Y.C. Angel, Effect of crack opening and orientation on dispersion and attenuation of antiplane coherent wave, Geophys. J. Int. 177 (2009) 1151-1165.

15. P.C. Waterman, R. Truell, Multiple scattering of waves, J. Math. Phys. 2 (1961) 512-537.

16. J.-M. Conoir, A. Norris, Effective wavenumbers and reflection coefficients for an elastic medium containing random configurations of cylindrical scatterers, Wave Motion, 47 (2010) 183-197.

17. J.-M. Conoir, A. Norris, F. Luppé, Generalization of the Waterman and Truell formula for an elastic medium containing random configurations of cylindrical scatterers, in: Congrès Français d'Acoustique CFA10, Lyon , France, 13-16 avril, 2010. CD-ROM, ISBN 978-2-9521105-7-0.

18. M. Caleap, C. Aristégui, Coherent wave propagation in solids containing various systems of frictional shear cracks, Waves Random Complex 20 (2010) 551-568.

General Conclusion and Perspectives

The problems of acoustic-wave propagation in inhomogeneous and damaged media with complex structure have always been of steady interest in view of miscellaneous applications. Recent emergence of phononic crystals and metamaterials have particularly intensified the research into acoustic properties of periodically inhomogeneous media. Another topical subject of acoustics is wave propagation in randomly damaged media with defined statistical distribution of defects leading to a multiple scattering problem.

The thesis presents results of modelling of acoustic wave propagation in periodical, inhomogeneous and random media. The numerical tool is developed which is compared with analytical predictions. In particular this work considers two problems: the problem of the elastic wave propagation in continuously or discretely periodic structures and the problem of multiple scattering. Predicted analytical results for the both problems are examined numerically using the developed FDTD numerical code. The consistency and accuracy of the numerical scheme has been confirmed via its application to the SH wave propagation in periodically inhomogeneous media and to the SH and P/SV wave multiple scattering in random media. Note that validation for scattering is especially convincing since this latter problem is fraught with many possible numerical errors.

Analytical modelling of the considered acoustic phenomena often (particularly in the case of multiple scattering theory) relies on certain a priori assumption, which renders numerical verification especially important. The developed numerical tool is general and flexible enough to provide a versatile basis for the consequent development. The numerical code is adapted to the scope of problems considered at the Physical Acoustics Department (APY) of the Institute of Mechanics and Engineering of Bordeaux (I2M), and it is a first step to create a numerical basis for tackling various problems of acoustics at APY Dpt (metamaterials, acoustic cloaking, phononic crystals, etc.). Moreover, due to its general handling of physical objects (i.e. of boundary conditions, sources, initial conditions and materials) the developed code can be extended to the problems of wave propagation in viscoelastic and in piezoelectric materials.

Appendix

FDTD formulas detailed for the P/SV case

This appendix aims at presenting different specific schemes used in our FDTD code for taking into account several types of boundary condition (BC) for the case of P and SV waves propagation.

The three commonly encountered types of BC are:

i) The traction-free boundary condition which implies a zero traction vector at the free surface;

ii) The sliding contact which is expressed by a zero shear stress and continuity of a normal component of particle-velocity fields at the interface between the two media;

iii) The rigid contact so that both the traction and the full velocity vector are continuous across the interface of two media.

For each case, we present an appropriate scheme taking into account which faces of the unit cell are subjected to the BC.

A.1 Free Boundary Condition

If one or two faces of the FDTD cell are free of traction (the case of three faces being free is excluded), we need to modify the scheme (3.20) which concerns the cells within the bulk of a medium. The arrangement of the nodes within the cell for the different mechanical fields is reminded in Fig. A.1, along with the FDTD scheme (3.20) which is repeated in (A.1).

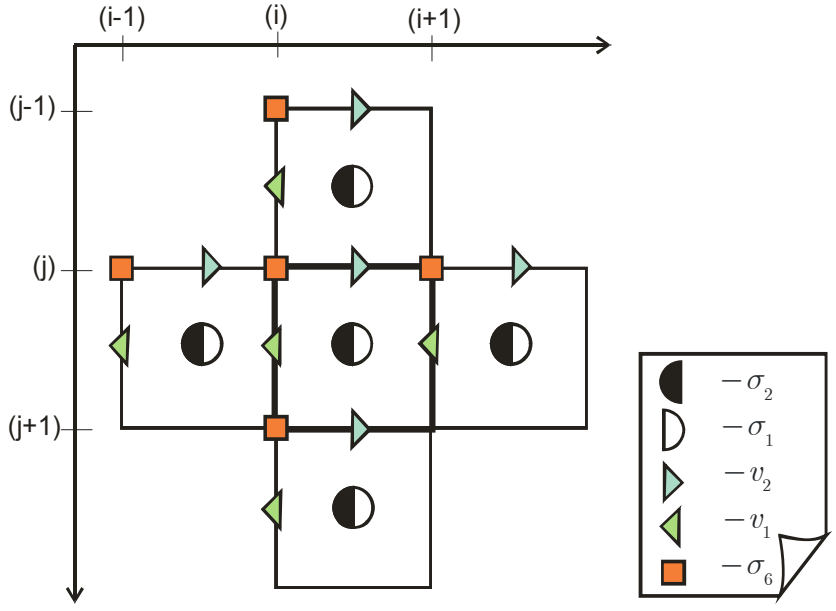

Fig. A1 *Discretization of the mechanical fields of the Bulk FDTD cell for the P/SV waves.*

$$
\begin{cases}
\left(v_1\right)_{i,j+\frac{1}{2}}^{n+\frac{1}{2}} = \left(v_1\right)_{i,j+\frac{1}{2}}^{n-\frac{1}{2}} + \dfrac{\Delta t}{\rho_{i,j+\frac{1}{2}}}\left(\dfrac{\left(\sigma_1\right)_{i+\frac{1}{2},j+\frac{1}{2}}^{n} - \left(\sigma_1\right)_{i-\frac{1}{2},j+\frac{1}{2}}^{n}}{\Delta x} + \dfrac{\left(\sigma_6\right)_{i,j+1}^{n} - \left(\sigma_6\right)_{i,j}^{n}}{\Delta y} + \left(f_1\right)_{i,j+\frac{1}{2}}^{n}\right), \\
\left(v_2\right)_{i+\frac{1}{2},j}^{n+\frac{1}{2}} = \left(v_2\right)_{i+\frac{1}{2},j}^{n-\frac{1}{2}} + \dfrac{\Delta t}{\rho_{i+\frac{1}{2},j}}\left(\dfrac{\left(\sigma_6\right)_{i+1,j}^{n} - \left(\sigma_6\right)_{i,j}^{n}}{\Delta x} + \dfrac{\left(\sigma_2\right)_{i+\frac{1}{2},j+\frac{1}{2}}^{n} - \left(\sigma_2\right)_{i+\frac{1}{2},j-\frac{1}{2}}^{n}}{\Delta y} + \left(f_2\right)_{i+\frac{1}{2},j}^{n}\right), \\
\left(\sigma_1\right)_{i+\frac{1}{2},j+\frac{1}{2}}^{n+1} = \left(\sigma_1\right)_{i+\frac{1}{2},j+\frac{1}{2}}^{n} + \Delta t\left(c_{11}\right)_{i+\frac{1}{2},j+\frac{1}{2}}\left(\dfrac{\left(v_1\right)_{i+1,j+\frac{1}{2}}^{n+\frac{1}{2}} - \left(v_1\right)_{i,j+\frac{1}{2}}^{n+\frac{1}{2}}}{\Delta x} - \left(h_1\right)_{i+\frac{1}{2},j+\frac{1}{2}}^{n+\frac{1}{2}}\right) + \\
\qquad\qquad + \Delta t\left(c_{12}\right)_{i+\frac{1}{2},j+\frac{1}{2}}\left(\dfrac{\left(v_2\right)_{i+\frac{1}{2},j+1}^{n+\frac{1}{2}} - \left(v_2\right)_{i+\frac{1}{2},j}^{n+\frac{1}{2}}}{\Delta y} - \left(h_2\right)_{i+\frac{1}{2},j+\frac{1}{2}}^{n+\frac{1}{2}}\right), \\
\left(\sigma_2\right)_{i+\frac{1}{2},j+\frac{1}{2}}^{n+1} = \left(\sigma_2\right)_{i+\frac{1}{2},j+\frac{1}{2}}^{n} + \Delta t\left(c_{12}\right)_{i+\frac{1}{2},j+\frac{1}{2}}\left(\dfrac{\left(v_1\right)_{i+1,j+\frac{1}{2}}^{n+\frac{1}{2}} - \left(v_1\right)_{i,j+\frac{1}{2}}^{n+\frac{1}{2}}}{\Delta x} - \left(h_1\right)_{i+\frac{1}{2},j+\frac{1}{2}}^{n+\frac{1}{2}}\right) + \\
\qquad\qquad + \Delta t\left(c_{22}\right)_{i+\frac{1}{2},j+\frac{1}{2}}\left(\dfrac{\left(v_2\right)_{i+\frac{1}{2},j+1}^{n+\frac{1}{2}} - \left(v_2\right)_{i+\frac{1}{2},j}^{n+\frac{1}{2}}}{\Delta y} - \left(h_2\right)_{i+\frac{1}{2},j+\frac{1}{2}}^{n+\frac{1}{2}}\right), \\
\left(\sigma_6\right)_{i,j}^{n+1} = \left(\sigma_6\right)_{i,j}^{n} + \Delta t\left(c_{66}\right)_{i,j}\left(\dfrac{\left(v_2\right)_{i+\frac{1}{2},j}^{n+\frac{1}{2}} - \left(v_2\right)_{i-\frac{1}{2},j}^{n+\frac{1}{2}}}{\Delta x} + \dfrac{\left(v_1\right)_{i,j+\frac{1}{2}}^{n+\frac{1}{2}} - \left(v_1\right)_{i,j-\frac{1}{2}}^{n+\frac{1}{2}}}{\Delta y} - \left(h_6\right)_{i,j}^{n+\frac{1}{2}}\right).
\end{cases}
\tag{A.1}
$$

A.1.1 BC at the top face

First, we consider the case of the *Top Free cell* (Fig. A2). In fact we are able in our code to generalize the traction-free BC with a zero traction to the loaded BC with any imposed value of traction, possibly depending on time. In either case, we remove from the initial scheme (A.1) the formula for $\left(\sigma_6\right)_{i,j}^{n}$ and instead set its value directly as

$$
\left(\sigma_6\right)_{i,j}^{n} = \begin{cases} 0 & (\text{free BC}), \\ \left(\sigma_6\right)_{BC}^{n}(n\Delta t) & (\text{loaded BC}). \end{cases}
\tag{A.2}
$$

Also, because the nodes for the component v_2 are located at the surface, equation (A.1)$_2$ must be modified by using a forward finite difference formula involving the component $\left(\sigma_2\right)_{i+\frac{1}{2},j+\frac{1}{2}}^{n}$ of the usual cell and the fixed value $\left(\sigma_2\right)_{BC}^{n}$ given by the BC:

$$
\left(v_2\right)_{i+\frac{1}{2},j}^{n+\frac{1}{2}} = \left(v_2\right)_{i+\frac{1}{2},j}^{n-\frac{1}{2}} + \frac{\Delta t}{\rho_{i+\frac{1}{2},j}}\left(\frac{\left(\sigma_6\right)_{i+1,j}^{n} - \left(\sigma_6\right)_{i,j}^{n}}{\Delta x} + \frac{\left(\sigma_2\right)_{i+\frac{1}{2},j+\frac{1}{2}}^{n} - \left(\sigma_2\right)_{BC}^{n}}{\Delta y/2} + \left(f_2\right)_{i+\frac{1}{2},j}^{n}\right),
\tag{A.3}
$$

where

$$\left(\sigma_2\right)_{BC}^{n} = \begin{cases} 0 & (\text{free BC}), \\ \left(\sigma_2\right)_{BC}^{n}(n\Delta t) & (\text{loaded BC}). \end{cases} \tag{A.4}$$

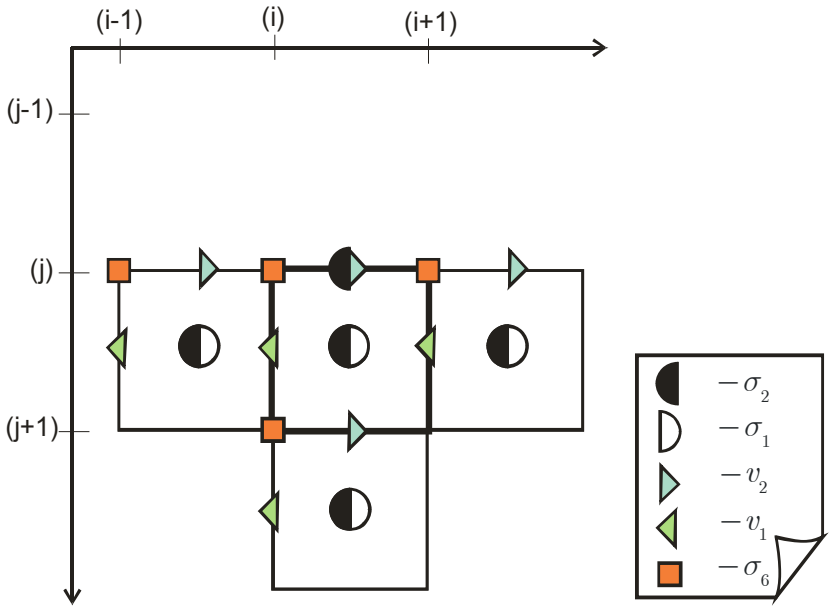

Fig. A2 *P/SV Top Free cell*

A.1.2 BC at the bottom face

In the case of the *Bottom Free cell* (Fig. A3) the formula $(A.1)_5$ is not used and the value of the component σ_6 at the left bottom corner of the cell is set to

$$\left(\sigma_6\right)_{i+1,j}^{n} = \begin{cases} 0 & (\text{free BC}), \\ \left(\sigma_6\right)_{BC}^{n}(n\Delta t) & (\text{loaded BC}). \end{cases} \tag{A.5}$$

For the same reason as above, the formula $(A.1)_2$ is replaced by

$$\left(v_2\right)_{i+\frac{1}{2},j}^{n+\frac{1}{2}} = \left(v_2\right)_{i+\frac{1}{2},j}^{n-\frac{1}{2}} + \frac{\Delta t}{\rho_{i+\frac{1}{2},j}}\left(\frac{\left(\sigma_6\right)_{i+1,j}^{n} - \left(\sigma_6\right)_{i,j}^{n}}{\Delta x} + \frac{\left(\sigma_2\right)_{BC}^{n} - \left(\sigma_2\right)_{i+\frac{1}{2},j-\frac{1}{2}}^{n}}{\Delta y/2} + \left(f_2\right)_{i+\frac{1}{2},j}^{n}\right), \tag{A.6}$$

where $\left(\sigma_2\right)_{BC}^{n}$ is the value determined by the BC on the normal stress on the bottom face:

$$\left(\sigma_2\right)_{BC}^{n} = \begin{cases} 0 & (\text{free BC}), \\ \left(\sigma_2\right)_{BC}^{n}(n\Delta t) & (\text{loaded BC}). \end{cases} \tag{A.7}$$

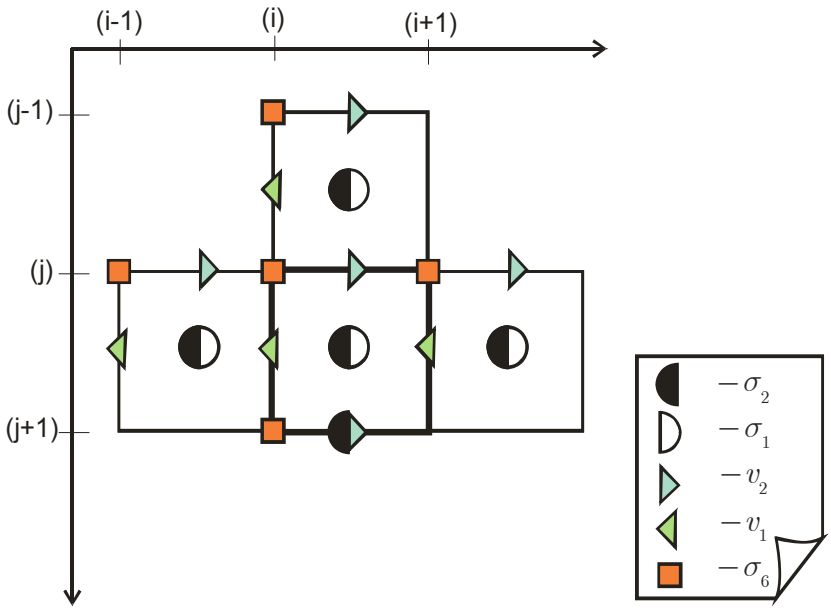

Fig. A3 *P/SV Bottom Free cell*

A.1.3 BC at the left face

For the *Left Free cell* (Fig. A4), the treatment for the value of σ_6 is exactly the same as in the two previous cases. But it is now the formula $(A.1)_1$ for v_1 that must be changed, namely:

$$\left(v_1\right)_{i,j+\frac{1}{2}}^{n+\frac{1}{2}} = \left(v_1\right)_{i,j+\frac{1}{2}}^{n-\frac{1}{2}} + \frac{\Delta t}{\rho_{i,j+\frac{1}{2}}}\left\{\frac{\left(\sigma_1\right)_{i+\frac{1}{2},j+\frac{1}{2}}^{n} - \left(\sigma_1\right)_{BC}^{n}}{\Delta x/2} + \frac{\left(\sigma_6\right)_{i,j+1}^{n} - \left(\sigma_6\right)_{i,j}^{n}}{\Delta y} + \left(f_1\right)_{i,j+\frac{1}{2}}^{n}\right\}, \quad \text{(A.8)}$$

where

$$\left(\sigma_1\right)_{BC}^{n} = \begin{cases} 0 & (\text{free BC}), \\ \left(\sigma_1\right)_{BC}^{n}(n\Delta t) & (\text{loaded BC}). \end{cases} \quad \text{(A.9)}$$

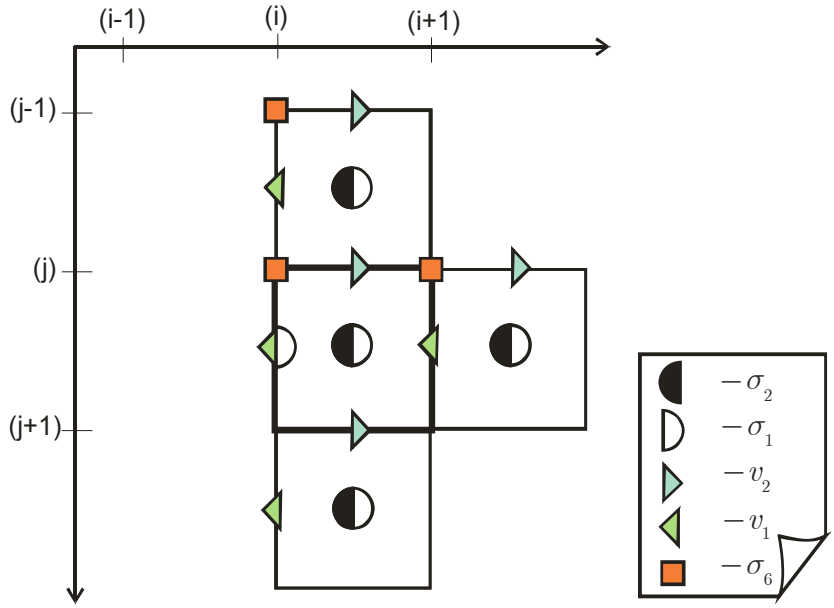

Fig. A4 *P/SV Left Free cell*

A.1.4 BC at the right face

In this case (see Fig. A5), equation $(A.1)_1$ becomes:

$$\left(v_1\right)_{i,j+\frac{1}{2}}^{n+\frac{1}{2}} = \left(v_1\right)_{i,j+\frac{1}{2}}^{n-\frac{1}{2}} + \frac{\Delta t}{\rho_{i,j+\frac{1}{2}}}\left(\frac{\left(\sigma_1\right)_{BC}^{n} - \left(\sigma_1\right)_{i+\frac{1}{2},j+\frac{1}{2}}^{n}}{\Delta x/2} + \frac{\left(\sigma_6\right)_{i,j+1}^{n} - \left(\sigma_6\right)_{i,j}^{n}}{\Delta y} + \left(f_1\right)_{i,j+\frac{1}{2}}^{n}\right), \quad \text{(A.10)}$$

where

$$\left(\sigma_1\right)_{BC}^{n} = \begin{cases} 0 & \text{(free BC)}, \\ \left(\sigma_1\right)_{BC}^{n}(n\Delta t) & \text{(loaded BC)}. \end{cases} \quad \text{(A.11)}$$

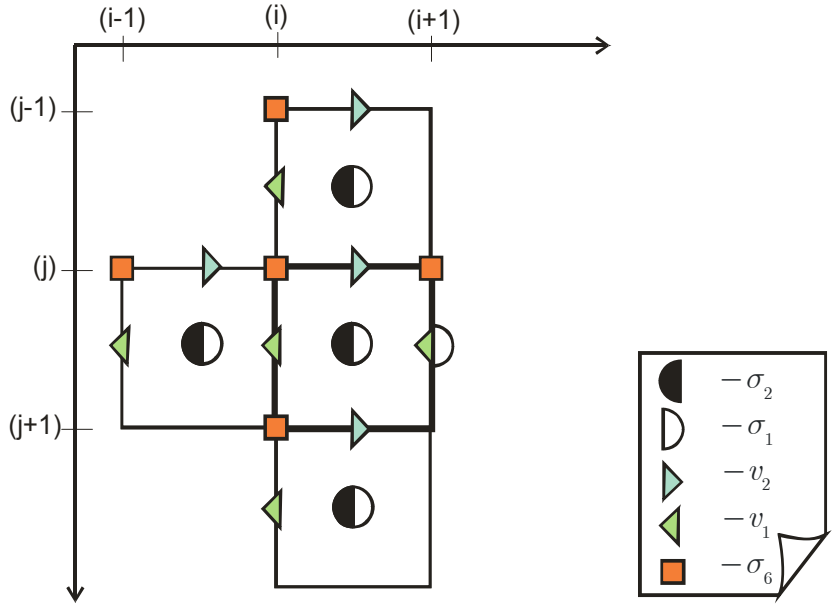

Fig. A5 *P/SV Right Free cell*

A.1.5 BC at the corner cells

Let us consider the cases of corners of the numerical domain subjected to boundary conditions. The particular types of cells whose treatment needs to be specialized are the *Left-Top Free, Right-Top Free, Left-Bottom Free* and *Right-Bottom Free* ones.

For the *Left-Top Free cell* (Fig. A6) we combine the conditions (A.2)-(A.4) and (A.8)-(A.9) for the Top BC and the Left BC at the same time.

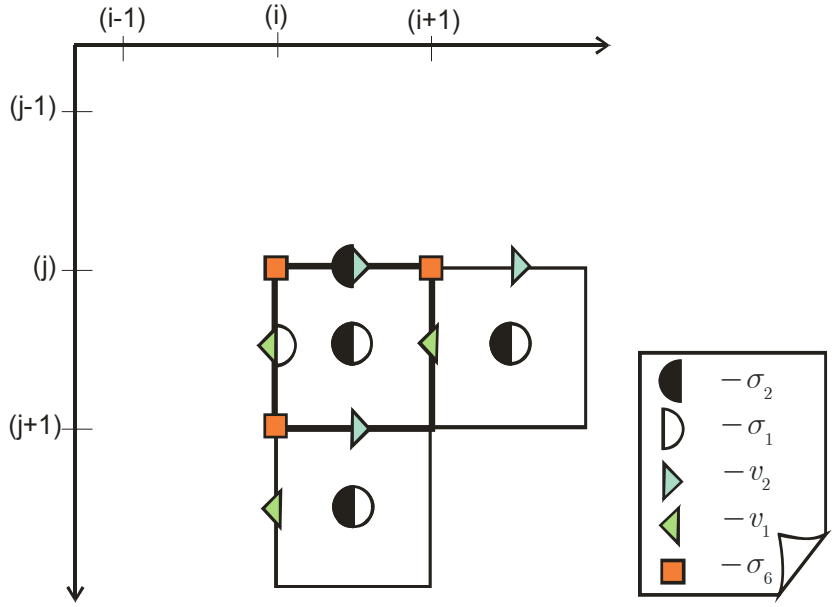

Fig. A6 *P/SV Left-Top Free cell*

In the case of *Left-Bottom Free cell* (Fig. A7) we combine the conditions (A.8)-(A.9) and (A.5)-(A.7).

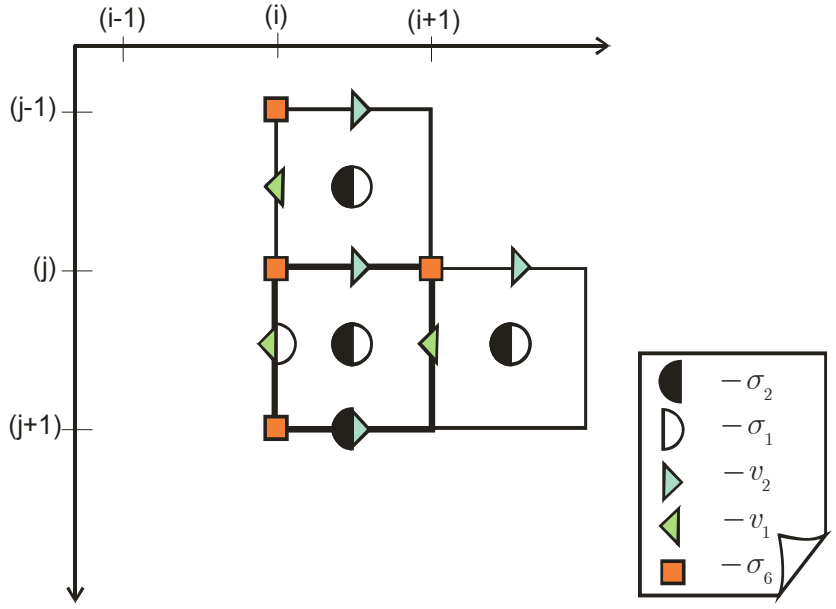

Fig. A7 *P/SV Left-Bottom Free cell*

In the case of *Right-Top Free cell* (Fig. A8) we combine the conditions (A.2)-(A.4) and (A.10)-(A.11).

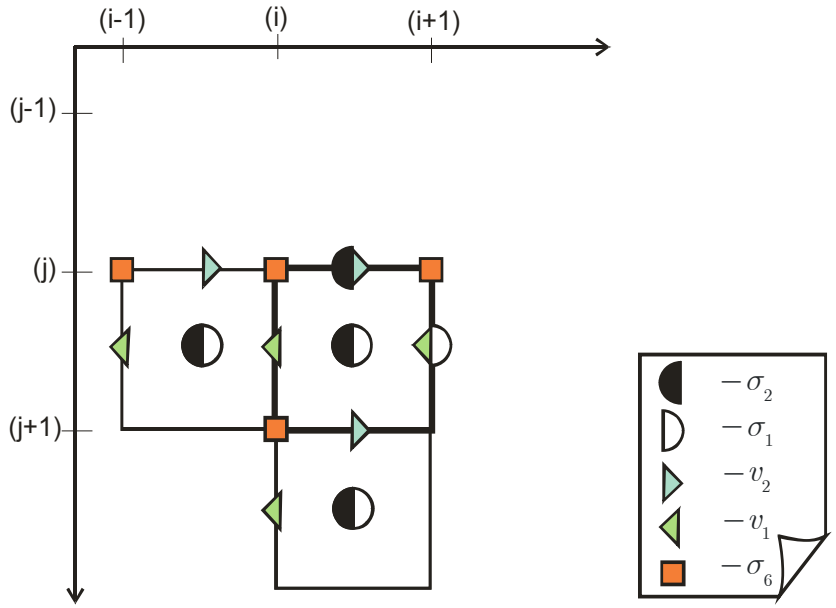

Fig. A8 *P/SV Right-Top Free cell*

For the special case of the *Right-Bottom Free cell* (Fig. A9), on top of combining conditions (A.10)-(A.11) and (A.5)-(A.7) for the right BC and bottom BC, we need to introduce an additional value σ_6 at the right-bottom corner of the unit-cell as follows

$$\left(\sigma_6\right)_{i+1,j+1}^{n} = \begin{cases} 0 & (\text{free BC}), \\ \left(\sigma_6\right)_{BC}^{n}(n\Delta t) & (\text{loaded BC}). \end{cases} \tag{A.12}$$

in order to calculate v_1 and v_2 in Eqs. (A.6) and (A.10).

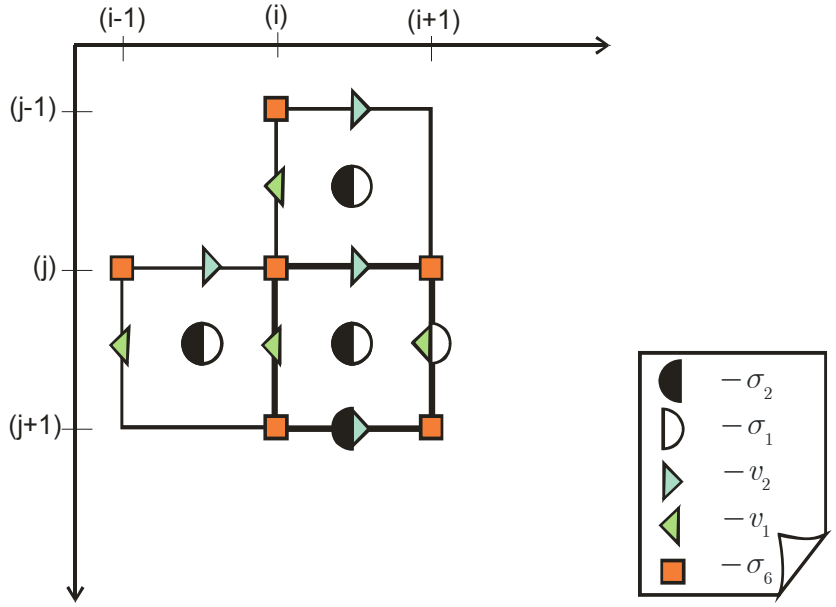

Fig. A9 *P/SV Right-Bottom Free cell*

A.2 Sliding Contact Boundary Conditions

Now we show how to treat a sliding contact in our FDTD scheme. By the definition (see Preamble to the Appendix A), this type of BC leads to zero stress σ_6 on the surfaces in contact. We provide two examples describing the *Top Sliding cell* and *Right-Bottom Sliding cell.*

The formulas for the *Top Sliding cell* (Fig. A10) are as follows:

$$\begin{cases} \left(v_1\right)_{i,j+\frac{1}{2}}^{n+\frac{1}{2}} = \left(v_1\right)_{i,j+\frac{1}{2}}^{n-\frac{1}{2}} + \dfrac{\Delta t}{\rho_{i,j+\frac{1}{2}}}\left(\dfrac{\left(\sigma_1\right)_{i+\frac{1}{2},j+\frac{1}{2}}^{n} - \left(\sigma_1\right)_{i-\frac{1}{2},j+\frac{1}{2}}^{n}}{\Delta x} + \dfrac{\left(\sigma_6\right)_{i,j+1}^{n} - 0}{\Delta y} + \left(f_1\right)_{i,j+\frac{1}{2}}^{n}\right), \\ \left(v_2\right)_{i+\frac{1}{2},j}^{n+\frac{1}{2}} = \left(v_2\right)_{i+\frac{1}{2},j}^{n-\frac{1}{2}} + \dfrac{\Delta t}{\rho_{i+\frac{1}{2},j}}\left(\dfrac{\left(\sigma_2\right)_{i+\frac{1}{2},j+\frac{1}{2}}^{n} - \left(\sigma_2\right)_{i+\frac{1}{2},j-\frac{1}{2}}^{n}}{\Delta y} + \left(f_2\right)_{i+\frac{1}{2},j}^{n}\right), \\ \left(\sigma_1\right)_{i+\frac{1}{2},j+\frac{1}{2}}^{n+1} = \left(\sigma_1\right)_{i+\frac{1}{2},j+\frac{1}{2}}^{n} + \Delta t\left(c_{11}\right)_{i+\frac{1}{2},j+\frac{1}{2}}\left(\dfrac{\left(v_1\right)_{i+1,j+\frac{1}{2}}^{n+\frac{1}{2}} - \left(v_1\right)_{i,j+\frac{1}{2}}^{n+\frac{1}{2}}}{\Delta x} - \left(h_1\right)_{i+\frac{1}{2},j+\frac{1}{2}}^{n+\frac{1}{2}}\right) + \\ \qquad + \Delta t\left(c_{12}\right)_{i+\frac{1}{2},j+\frac{1}{2}}\left(\dfrac{\left(v_2\right)_{i+\frac{1}{2},j+1}^{n+\frac{1}{2}} - \left(v_2\right)_{i+\frac{1}{2},j}^{n+\frac{1}{2}}}{\Delta y} - \left(h_2\right)_{i+\frac{1}{2},j+\frac{1}{2}}^{n+\frac{1}{2}}\right), \\ \left(\sigma_2\right)_{i+\frac{1}{2},j+\frac{1}{2}}^{n+1} = \left(\sigma_2\right)_{i+\frac{1}{2},j+\frac{1}{2}}^{n} + \Delta t\left(c_{12}\right)_{i+\frac{1}{2},j+\frac{1}{2}}\left(\dfrac{\left(v_1\right)_{i+1,j+\frac{1}{2}}^{n+\frac{1}{2}} - \left(v_1\right)_{i,j+\frac{1}{2}}^{n+\frac{1}{2}}}{\Delta x} - \left(h_1\right)_{i+\frac{1}{2},j+\frac{1}{2}}^{n+\frac{1}{2}}\right) + \\ \qquad + \Delta t\left(c_{22}\right)_{i+\frac{1}{2},j+\frac{1}{2}}\left(\dfrac{\left(v_2\right)_{i+\frac{1}{2},j+1}^{n+\frac{1}{2}} - \left(v_2\right)_{i+\frac{1}{2},j}^{n+\frac{1}{2}}}{\Delta y} - \left(h_2\right)_{i+\frac{1}{2},j+\frac{1}{2}}^{n+\frac{1}{2}}\right), \\ \left(\sigma_6\right)_{i,j}^{n} = 0. \end{cases} \tag{A.13}$$

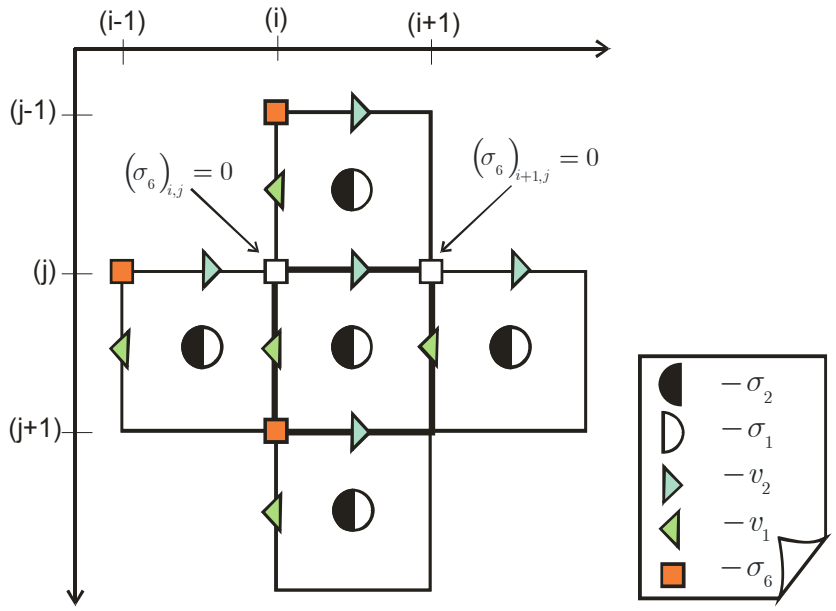

Fig. A10 *P/SV Top Sliding cell*

The formulas for the *Right-Bottom Sliding cell* (Fig. A11) are as follows:

$$
\begin{cases}
(v_1)^{n+\frac{1}{2}}_{i,j+\frac{1}{2}} = (v_1)^{n-\frac{1}{2}}_{i,j+\frac{1}{2}} + \dfrac{\Delta t}{\rho_{i,j+\frac{1}{2}}}\left(\dfrac{(\sigma_1)^{n}_{i+\frac{1}{2},j+\frac{1}{2}} - (\sigma_1)^{n}_{i-\frac{1}{2},j+\frac{1}{2}}}{\Delta x} + \dfrac{0-(\sigma_6)^{n}_{i,j}}{\Delta y} + (f_1)^{n}_{i,j+\frac{1}{2}}\right), \\
(v_2)^{n+\frac{1}{2}}_{i+\frac{1}{2},j} = (v_2)^{n-\frac{1}{2}}_{i+\frac{1}{2},j} + \dfrac{\Delta t}{\rho_{i+\frac{1}{2},j}}\left(\dfrac{(\sigma_6)^{n}_{i+1,j} - (\sigma_6)^{n}_{i,j}}{\Delta x} + \dfrac{0-(\sigma_2)^{n}_{i+\frac{1}{2},j-\frac{1}{2}}}{\Delta y} + (f_2)^{n}_{i+\frac{1}{2},j}\right), \\
(\sigma_1)^{n+1}_{i+\frac{1}{2},j+\frac{1}{2}} = (\sigma_1)^{n}_{i+\frac{1}{2},j+\frac{1}{2}} + \Delta t(c_{11})_{i+\frac{1}{2},j+\frac{1}{2}}\left(\dfrac{(v_1)^{n+\frac{1}{2}}_{i+1,j+\frac{1}{2}} - (v_1)^{n+\frac{1}{2}}_{i,j+\frac{1}{2}}}{\Delta x} - (h_1)^{n+\frac{1}{2}}_{i+\frac{1}{2},j+\frac{1}{2}}\right) + \\
\qquad + \Delta t(c_{12})_{i+\frac{1}{2},j+\frac{1}{2}}\left(\dfrac{(v_2)^{n+\frac{1}{2}}_{i+\frac{1}{2},j+1} - (v_2)^{n+\frac{1}{2}}_{i+\frac{1}{2},j}}{\Delta y} - (h_2)^{n+\frac{1}{2}}_{i+\frac{1}{2},j+\frac{1}{2}}\right), \\
(\sigma_2)^{n+1}_{i+\frac{1}{2},j+\frac{1}{2}} = (\sigma_2)^{n}_{i+\frac{1}{2},j+\frac{1}{2}} + \Delta t(c_{12})_{i+\frac{1}{2},j+\frac{1}{2}}\left(\dfrac{(v_1)^{n+\frac{1}{2}}_{i+1,j+\frac{1}{2}} - (v_1)^{n+\frac{1}{2}}_{i,j+\frac{1}{2}}}{\Delta x} - (h_1)^{n+\frac{1}{2}}_{i+\frac{1}{2},j+\frac{1}{2}}\right) + \\
\qquad + \Delta t(c_{22})_{i+\frac{1}{2},j+\frac{1}{2}}\left(\dfrac{(v_2)^{n+\frac{1}{2}}_{i+\frac{1}{2},j+1} - (v_2)^{n+\frac{1}{2}}_{i+\frac{1}{2},j}}{\Delta y} - (h_2)^{n+\frac{1}{2}}_{i+\frac{1}{2},j+\frac{1}{2}}\right), \\
(\sigma_6)^{n+1}_{i,j} = (\sigma_6)^{n}_{i,j} + \Delta t(c_{66})_{i,j}\left(\dfrac{(v_2)^{n+\frac{1}{2}}_{i+\frac{1}{2},j} - (v_2)^{n+\frac{1}{2}}_{i-\frac{1}{2},j}}{\Delta x} + \dfrac{(v_1)^{n+\frac{1}{2}}_{i,j+\frac{1}{2}} - (v_1)^{n+\frac{1}{2}}_{i,j-\frac{1}{2}}}{\Delta y} - (h_6)^{n+\frac{1}{2}}_{i,j}\right).
\end{cases}
\tag{A.14}
$$

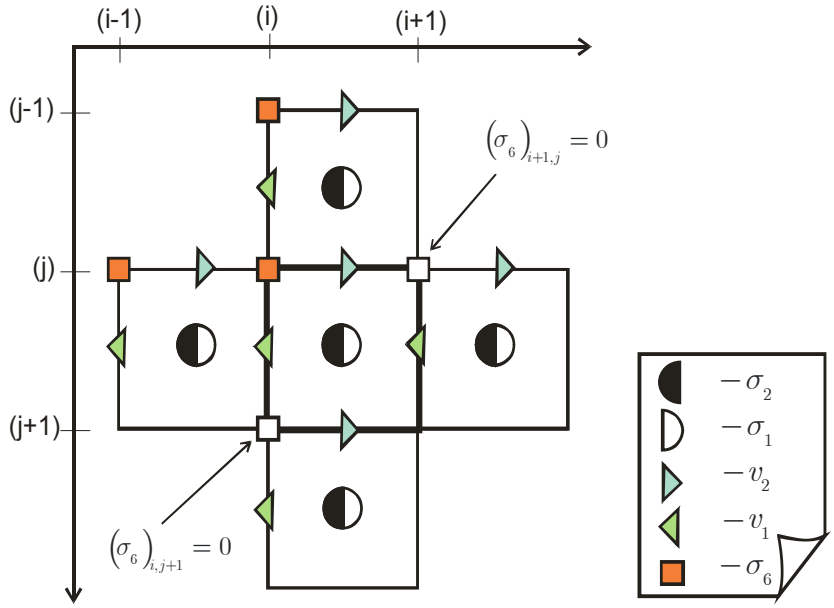

Fig. A11 *P/SV Right Bottom Sliding cell*

A.3 Rigid contact between two different materials

We proceed the same way as in Section 3.4.3. First, we assume that the interface between the two media is horizontal. To compute the update of the component v_2 at the interface, we consider the interfacial value σ_2^* of the continuous normal stress (see Fig. A12) which is normally not involved in the common FDTD scheme. We find

$$\rho_1 \frac{\Delta(v_2)_{i+\frac{1}{2},j}}{\Delta t} = \frac{\sigma_2^* - (\sigma_2)_{i+\frac{1}{2},j-\frac{1}{2}}}{\Delta y/2} + \frac{(\sigma_6)_{i+1,j} - (\sigma_6)_{i,j}}{\Delta x} \tag{A.15}$$

for the cell above the contact (the first medium), and

$$\rho_2 \frac{\Delta(v_2)_{i+\frac{1}{2},j}}{\Delta t} = \frac{(\sigma_2)_{i+\frac{1}{2},j+\frac{1}{2}} - \sigma_2^*}{\Delta y/2} + \frac{(\sigma_6)_{i+1,j} - (\sigma_6)_{i,j}}{\Delta x} \tag{A.16}$$

for the cell below (the second medium). Taking half of the sum of those two expressions leads to

$$\frac{\rho_1 + \rho_2}{2} \frac{\Delta(v_2)_{i+\frac{1}{2},j}}{\Delta t} = \frac{(\sigma_2)_{i+\frac{1}{2},j+\frac{1}{2}} - (\sigma_2)_{i+\frac{1}{2},j-\frac{1}{2}}}{\Delta y} + \frac{(\sigma_6)_{i+1,j} - (\sigma_6)_{i,j}}{\Delta x}. \tag{A.17}$$

For the updating of $(\sigma_6)_{i,j}$ we use a similar approach by introducing an additional value v_1^* at the interface (see Fig. A12), at the point with coordinate (i, j):

$$\frac{1}{c_{66}^{(1)}} \frac{\Delta(\sigma_6)_{i,j}}{\Delta t} = \frac{(v_1)_{i,j+\frac{1}{2}} - v_1^*}{\Delta y/2} + \frac{(v_2)_{i+\frac{1}{2},j} - (v_2)_{i-\frac{1}{2},j}}{\Delta x}, \tag{A.18}$$

$$\frac{1}{c_{66}^{(2)}}\frac{\Delta(\sigma_6)_{i,j}}{\Delta t}=\frac{v_1^*-(v_1)_{i,j-\frac{1}{2}}}{\Delta y/2}+\frac{(v_2)_{i+\frac{1}{2},j}-(v_2)_{i-\frac{1}{2},j}}{\Delta x}. \tag{A.19}$$

Again taking half of the sum of (A.18) and (A.19), we find

$$\left(\frac{1}{2c_{66}^{(1)}}+\frac{1}{2c_{66}^{(2)}}\right)\frac{\Delta(\sigma_6)_{i,j}}{\Delta t}=\frac{(v_1)_{i,j+\frac{1}{2}}-(v_1)_{i,j-\frac{1}{2}}}{\Delta y}+\frac{(v_2)_{i+\frac{1}{2},j}-(v_2)_{i-\frac{1}{2},j}}{\Delta x} \tag{A.20}$$

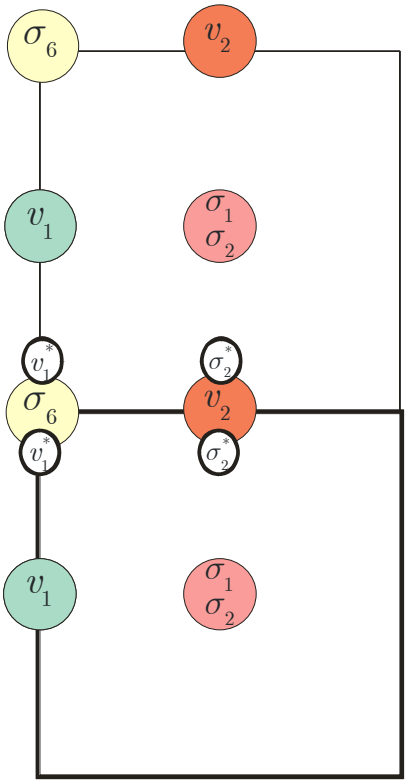

Fig. A12 *Horizontal rigid contact between two materials*

Altogether, we obtain the following formulas for the bottom cell (the updating of the components of the upper cell being not affected by the interface)

$$\begin{cases}\rho\dfrac{\Delta(v_1)_{i,j+\frac{1}{2}}}{\Delta t}=\dfrac{(\sigma_1)_{i+\frac{1}{2},j+\frac{1}{2}}-(\sigma_1)_{i-\frac{1}{2},j+\frac{1}{2}}}{\Delta x}+\dfrac{(\sigma_6)_{i,j+1}-(\sigma_6)_{i,j}}{\Delta y},\\ \dfrac{\rho_1+\rho_2}{2}\dfrac{\Delta(v_2)_{i+\frac{1}{2},j}}{\Delta t}=\dfrac{(\sigma_2)_{i+\frac{1}{2},j+\frac{1}{2}}-(\sigma_2)_{i+\frac{1}{2},j-\frac{1}{2}}}{\Delta y}+\dfrac{(\sigma_6)_{i+1,j}-(\sigma_6)_{i,j}}{\Delta x},\\ \dfrac{\Delta(\sigma_1)_{i+\frac{1}{2},j+\frac{1}{2}}}{\Delta t}=c_{11}\dfrac{(v_1)_{i+1,j+\frac{1}{2}}-(v_1)_{i,j+\frac{1}{2}}}{\Delta x}+c_{12}\dfrac{(v_2)_{i+\frac{1}{2},j+1}-(v_2)_{i+\frac{1}{2},j}}{\Delta y},\\ \dfrac{\Delta(\sigma_2)_{i+\frac{1}{2},j+\frac{1}{2}}}{\Delta t}=c_{12}\dfrac{(v_1)_{i+1,j+\frac{1}{2}}-(v_1)_{i,j+\frac{1}{2}}}{\Delta y}+c_{22}\dfrac{(v_2)_{i+\frac{1}{2},j+1}-(v_2)_{i+\frac{1}{2},j}}{\Delta x},\\ \left(\dfrac{1}{2c_{66}^{(1)}}+\dfrac{1}{2c_{66}^{(2)}}\right)\dfrac{\Delta(\sigma_6)_{i,j}}{\Delta t}=\dfrac{(v_1)_{i,j+\frac{1}{2}}-(v_1)_{i,j-\frac{1}{2}}}{\Delta y}+\dfrac{(v_2)_{i+\frac{1}{2},j}-(v_2)_{i-\frac{1}{2},j}}{\Delta x}.\end{cases} \tag{A.21}$$

If the contact occurs vertically (see Fig. A13), we similarly obtain the following formulas for the right cell

$$\begin{cases} \dfrac{\rho_1+\rho_2}{2}\dfrac{\Delta\left(v_1\right)_{i,j+\frac{1}{2}}}{\Delta t}=\dfrac{\left(\sigma_1\right)_{i+\frac{1}{2},j+\frac{1}{2}}-\left(\sigma_1\right)_{i-\frac{1}{2},j+\frac{1}{2}}}{\Delta x}+\dfrac{\left(\sigma_6\right)_{i,j+1}-\left(\sigma_6\right)_{i,j}}{\Delta y}, \\ \rho\dfrac{\Delta\left(v_2\right)_{i+\frac{1}{2},j}}{\Delta t}=\dfrac{\left(\sigma_2\right)_{i+\frac{1}{2},j+\frac{1}{2}}-\left(\sigma_2\right)_{i+\frac{1}{2},j-\frac{1}{2}}}{\Delta y}+\dfrac{\left(\sigma_6\right)_{i+1,j}-\left(\sigma_6\right)_{i,j}}{\Delta x}, \\ \dfrac{\Delta\left(\sigma_1\right)_{i+\frac{1}{2},j+\frac{1}{2}}}{\Delta t}=c_{11}\dfrac{\left(v_1\right)_{i+1,j+\frac{1}{2}}-\left(v_1\right)_{i,j+\frac{1}{2}}}{\Delta x}+c_{12}\dfrac{\left(v_2\right)_{i+\frac{1}{2},j+1}-\left(v_2\right)_{i+\frac{1}{2},j}}{\Delta y}, \\ \dfrac{\Delta\left(\sigma_2\right)_{i+\frac{1}{2},j+\frac{1}{2}}}{\Delta t}=c_{12}\dfrac{\left(v_1\right)_{i+1,j+\frac{1}{2}}-\left(v_1\right)_{i,j+\frac{1}{2}}}{\Delta y}+c_{22}\dfrac{\left(v_2\right)_{i+\frac{1}{2},j+1}-\left(v_2\right)_{i+\frac{1}{2},j}}{\Delta x}, \\ \left(\dfrac{1}{2c_{66}^{(1)}}+\dfrac{1}{2c_{66}^{(2)}}\right)\dfrac{\Delta\left(\sigma_6\right)_{i,j}}{\Delta t}=\dfrac{\left(v_1\right)_{i,j+\frac{1}{2}}-\left(v_1\right)_{i,j-\frac{1}{2}}}{\Delta y}+\dfrac{\left(v_2\right)_{i+\frac{1}{2},j}-\left(v_2\right)_{i-\frac{1}{2},j}}{\Delta x}. \end{cases} \tag{A.22}$$

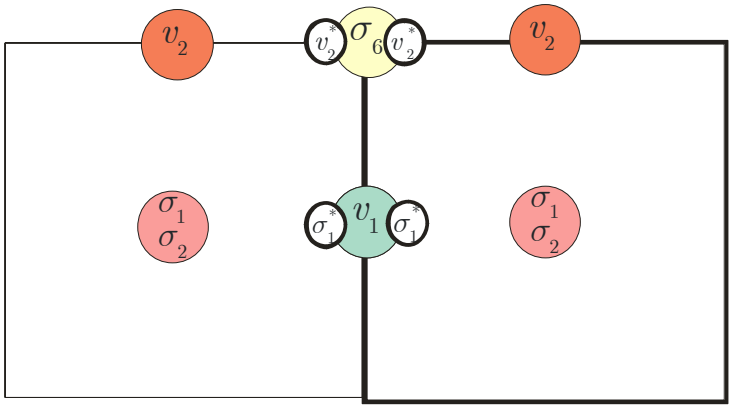

Fig. A13 *Vertical rigid contact between two materials*